

Chuyan Zhang

**Structural Dependence  
of Diamond Composites on  
Electrocatalytic Performance  
of Small Molecules**

**Schriftenreihe der Arbeitsgruppe  
des Lehrstuhls für Oberflächen- und Werkstofftechnologie  
im Institut für Werkstofftechnik**

**Herausgeber: Prof. Dr. rer. nat. habil. Xin Jiang**

**Band 20**

---

**Chuyan Zhang**

Structural Dependence of Diamond Composites on Electrocatalytic Performance of  
Small Molecules

Schriftenreihe der Arbeitsgruppe des Lehrstuhls für Oberflächen- und  
Werkstofftechnologie im Institut für Werkstofftechnik



---

### **Impressum**

Prof. Dr. rer. nat. habil. Xin Jiang

Lehrstuhl für Oberflächen- und Werkstofftechnologie

Institut für Werkstofftechnik

Universität Siegen

57076 Siegen

ISSN: 2194-0096

Zugl.: Siegen, Univ., Diss., 2023



---

# **Structural Dependence of Diamond Composites on Electrocatalytic Performance of Small Molecules**

Von der Naturwissenschaftlich-Technischen Fakultät  
der Universität Siegen

zur Erlangung des Grades eines Doktors  
der Ingenieurwissenschaften  
genehmigte

## **Dissertation**

von:	M. Sc. Chuyan Zhang
aus:	Liaoning, China
eingereicht am:	17. Mai 2023
Mündliche Prüfung am:	15. August 2023
Referent:	Prof. Dr. rer. nat. habil. Xin Jiang
Korreferent:	Prof. Dr. Holger Schönherr



---



## Kurzfassung

Die Elektrokatalyse kleiner Moleküle kann einen nachhaltigen Beitrag zur Lösung von globalen Energiekrisen und Umweltproblemen leisten. Ein Schlüssel, um den Energieverlust in elektrokatalytischen Prozessen zu verringern, ist die sinnvolle Entwicklung effizienter und stabiler Katalysatoren unter günstigen Bedingungen. Jedoch stehen die hohen Kosten, begrenzte Verfügbarkeit, Vergiftungsanfälligkeit und vereinzelte aktive Zentren kommerzieller Edelmetall-Katalysatoren (z.B. Pt/C und RuO<sub>2</sub>) der großmaßstäblichen Anwendbarkeit entgegen. Außerdem finden die häufigsten katalytischen Reaktionen kleiner Moleküle, z.B. der Sauerstoffreduktions-/Entwicklungsreaktion (ORR/OER), der Kohlendioxidreduktionsreaktion (CO<sub>2</sub>RR) und der Nitratreduktionsreaktion (NITRR) über Mehrelektronenreaktionen statt, bei denen eine verzögerte Kinetik und komplexe Reaktionswege vorliegen. Deshalb reichen nur vereinzelte metallische aktive Zentren auf den Katalysatoroberflächen nicht aus, um diese Herausforderungen zu stemmen. Es ist darüber hinaus nötig, die Reaktionsmechanismen aufzuklären, heterogene Katalysatoren zu entwickeln und die Struktur und Zusammensetzung der verschiedenen Komponenten aufeinander abzustimmen.

Diamantelektroden werden aufgrund ihres breiten Potenzialfensters, geringen Hintergrundstromes, ihrer hohen chemischen Stabilität und Resistenz gegen Katalysatorvergiftung als elektrochemische Sensoren und zur fortgeschrittenen elektrokatalytischen Oxidation von Schadstoffen verwendet. Bei der Elektrokatalyse von kleinen Molekülen bedeutet das breite Potenzialfenster die thermodynamische Hemmung der Wasserstoffentwicklung (HER), wodurch die Selektivität für ORR, CO<sub>2</sub>RR und NITRR garantiert wird. Weiterhin besitzt die robuste Struktur ausreichende Stabilität und Recyclingmöglichkeiten in extremen Umgebungen. Allerdings ist die elektrokatalytische Leistung von Diamantelektroden aufgrund des Mangels an aktiven Zentren reduziert. Die Herausforderung liegt darin, mehrere aktive Zentren sowie das Gleichgewicht zwischen Aktivität und Stabilität zu schaffen.

In dieser Arbeit werden Berechnungen der Dichtefunktionaltheorie (DFT) mit Experimenten kombiniert, um effiziente und robuste Diamantkomposite als Katalysatoren für die Elektrokatalyse kleiner Moleküle (z.B. Sauerstoff und Nitrat) zu untersuchen. Ein tieferes Verständnis der Beziehung zwischen Struktur und Leistung wird erforscht, um die praktische Anwendung in Energiegeräten zu entwickeln.

Bei der Elektrokatalyse von Sauerstoff (ORR/OER) werden die Stickstoff-dotierten Kohlenstoff-Nanowände/Diamant (N-CNWs/D) Komposite mittels mikrowellenplasmaunterstützter chemischer Gasphasenabscheidung (MPCVD) synthetisiert. Die Komposite bestehen aus einer dünnen Nanodiamantschicht als Substrat und einem vertikal ausgerichteten Multigraphen an der Oberfläche. Nach einer Nachbehandlung durch Glühen weisen die Komposite eine hervorragende ORR-Leistung (hohes Onset-Potential von 835 mV vs. RHE) und eine ausgezeichnete Stabilität (90 % Stromerhalt nach 20 Stunden) auf. Die verbesserte ORR-Leistung wird auf die aktivierten und exponierten Kantenstellen von CNWs/D und eine gebundene Nanodiamantschicht zurückgeführt. Weiterhin werden die  $\text{Co}_4\text{N}@d\text{-NCNWs/D}$  Komposite produziert und als bifunktionale ORR/OER-Katalysatoren eingesetzt. DFT-Berechnungen sagen voraus, dass die verstärkte Wechselwirkung zwischen  $\text{Co}_4\text{N}$  und  $d\text{-NCNWs/D}$  eine optimale Dispersion der  $\text{Co}_4\text{N}$ -Nanopartikel fördert. Außerdem werden die elektronischen Strukturen der Co- und C-Atome an der Grenzfläche angepasst, wodurch das Überpotential von ORR/OER von 0,67 auf 0,23 eV reduziert wird. Experimentelle Ergebnisse bestätigen, dass die Komposite über eine hervorragende bifunktionale ORR/OER-Leistung (z. B. eine kleine Potenzialdifferenz von 0,75 V) verfügen. Somit werden diese Komposite als Luft-Kathode verwendet. Die aufgebauten flexiblen Zink-Luft-Batterien weisen eine hohe Leerlaufspannung von 1,41 V und eine aufgezeichnete Biegestabilität auf.

Im Hinblick auf die Elektrokatalyse von Nitraten werden die mit Kupfer-Nanopartikeln beschichteten Bor-dotierten Diamantgewebe ( $\text{Cu-np}@BDD\text{-m}$ ) mittels chemischer Heißfilament-Gasphasenabscheidung (HFCVD) und Magnetron-

Sputtering synthetisiert. Nach dem Niederdruckätzverfahren werden Cu-Nanopartikel in die BDD-m-Oberfläche eingebettet, was zu verstärkten Metall-Support-Wechselwirkungen führt. Die DFT-Berechnungen zeigen, dass diese starke Wechselwirkung die Adsorption von stickstoffhaltigen Zwischenprodukten (z. B.  $^*\text{NO}_3$ ,  $^*\text{NO}_2$ ,  $^*\text{N}$ ) verstärkt, die Reaktionsenergie durch NITRR von 1,06 auf 0,91 eV minimiert und die Energiebarriere für konkurrierende HER von 0,50 auf 0,97 eV unter neutralen Bedingungen steigert. Somit weisen die Komposite eine hervorragende NITRR-Leistung auf (z. B. Nitratentfernung von 90,2 % und Ammoniakselektivität von 76,8 %). Der erzeugte nanoskalige Bereich stabilisiert die aktiven Stellen und verbessert die lokale Adsorption von Nitraten, die zu einer Verschiebung des diffusionsgesteuerten Onset-Potenzials der ersten Stufe führt (von -0,25 auf 0,1 V vs. RHE). Auf diese Weise wird der NITRR-Mechanismus in thermodynamischen und kinetischen Prozessen deutlich in den Vordergrund gerückt. Eine solche Elektrode wird zum Aufbau von Flüssigkeitsflussreaktoren für nachhaltige Anwendungen angesehen.

Zusammenfassend wurden in dieser Arbeit effiziente und robuste Diamantkomposite als Katalysatoren für die Elektrokatalyse kleiner Moleküle sowie Sauerstoff und Nitrat hergestellt. Durch die Konstruktion einer sinnvollen Trägerstruktur, Modifizierung der aktiven Zentren auf der Oberfläche sowie Begünstigung verstärkter Metall-Support-Wechselwirkungen wird ein Gleichgewicht zwischen der Aktivität und Stabilität erreicht. Der vorgeschlagene Ansatz für das Katalysatordesign wird zur Elektrokatalyse anderer kleiner Moleküle und für die Konstruktion künftiger Energiegeräte verwendet.

## Acknowledgements

First of all, I would like to express my sincere gratitude to my supervisor, Prof. Xin Jiang, for his professional guidance and kind support during my Ph.D. studies and life. Thanks to him forgiving me the opportunity to start my Ph.D. work. His extensive knowledge led me into the field of diamonds, and his research attitude has benefited me both in my studies and future life.

Besides my supervisor, I would like to thank the other members of my thesis committee: Prof. Dr. Holger Schönherr, Prof. Dr. rer. Nat. Benjamin Butz and Prof. Dr. Nianjun Yang.

I would like to thank Prof. Nianjun Yang for his valuable help during my PhD studies. He always encouraged me to continue my research with an open mind. In addition, he gave me much guidance in my English thesis writing skills.

As most of my experimental works was done at the institute of metal research (IMR) in China, I would like to thank Prof. Nan Huang for her support. She was very patient, discussing with me and improving the quality of my work.

I would also like to thank all my colleagues. Thanks to Ms. Andrea Brombach for helping me with student affairs. Ximan Dong and Xinyue Chen are the people I met and welcomed on my first day in Siegen. Tianxiao Guo and Suta Kevin for discussing ideas and revising my thesis. Thanks to Yao Li, Changli Li, Chen Wang, Dr. Ullah Hameed, Dr. Aleksandr Zubtsovskii and Dr. Thorsten Staedler for their support of my Ph.D. thesis.

Special thanks to Dr. Zhai Zhaofeng for introducing me to the experimental techniques and methods when I was still a beginner. He was very caring and encouraging to me. Many thanks to Bin Chen for his scientific way of thinking. Thanks to Dr. Dan Shi, Dr. Haining Li and Meiqi Zhou for taking care of me in my life. Thanks to Dr. Zhigang Lu for calming me down and Dr. Cai Zhang for helping me in the tube furnace experiments.

I am grateful to all the cooperators and technician: Stefan Wagner, Dr. Bing Yang,

Lusheng Liu, Dr. Ziyao Yuan, Haozhe Song, TianwenHu, Yuhua Yang, Jiaqi Lu, Jiayi Xiong, Ziwen Zheng, Mengrui Wang, Zhaolun Cui, Jiaxin Wang, Junyao Li, Xiao Zhao and Jiayi Lan.

For experimental measurements, special thanks to Dr. Zhaofeng Zhai, Bin Chen and Dr. Bing Yang for their help in TEM measurements. Raman and SEM were performed at the laboratory of IMR. XPS and XRD were done at the *Analytical Center* of IMR. XAS was done at the *Shanghai Science Compass Test Center*. It was also grateful to the *Shenzhen Cloud Computing Center* for allowing the use of their computing facilities for DFT simulations.

Finally, I would like to thank my friends and parents forgiving me strength during my Ph.D. studies. Without them, I would not have been able to complete this thesis.

Siegen, in September 2023

Chuyan Zhang

## Contents

<b>Kurzfassung.....</b>	<b>II</b>
<b>Acknowledgements.....</b>	<b>V</b>
<b>Symbol List.....</b>	<b>X</b>
<b>Abstract .....</b>	<b>XVI</b>
<b>1 Introduction .....</b>	<b>1</b>
1.1 Electrocatalysis of small molecules .....	1
1.1.1 Challenges in electrocatalysis of oxygen .....	2
1.1.2 Challenges in electrocatalysis of nitrate.....	2
1.2 Development of diamond composite catalysts .....	3
1.3 Motivation of the thesis .....	11
1.4 Overview of the thesis .....	11
<b>2 Theoretical fundamentals.....</b>	<b>14</b>
2.1 Concepts of electrocatalyst design .....	14
2.1.1 Sabatier principle and volcano curve .....	14
2.1.2 Linear scaling relationship .....	15
2.1.3 Brønsted-Evans-Polanyi relationship.....	17
2.1.4 <i>d</i> -band center theory .....	18
2.2 Reaction pathways .....	19
2.2.1 Oxygen reduction reaction and oxygen evolution reaction .....	19
2.2.2 Nitrate reduction reaction .....	21
2.3 Density functional theory calculations .....	23
2.3.1 The time-independent Schrödinger equation .....	24
2.3.2 Hartree-Fock method .....	25
2.3.3 Density functional theory .....	26
2.3.4 Pseudopotential .....	28
<b>3 Experimental .....</b>	<b>30</b>
3.1 Film deposition techniques .....	30

3.1.1 Microwave plasma enhanced chemical vapor deposition .....	30
3.1.2 Hot filament chemical vapor deposition .....	30
3.1.3 Magnetron sputtering .....	31
3.1.4 Electrodeposition .....	32
3.2 Preparation of diamond composites.....	33
3.2.1 N-CNWs/D composites .....	33
3.2.2 Co <sub>4</sub> N@d-NCNWs/D composites .....	35
3.2.3 Cu-np@BDD-m composites .....	37
3.3 Characterization .....	38
3.3.1 Morphology and physical structure characterization .....	38
3.3.2 Surface states analysis .....	39
3.3.3 X-ray absorption spectroscopy (XAS) .....	41
3.4 Electrochemical investigations .....	43
3.4.1 Electrochemical methods .....	44
3.4.2 Electrocatalytic oxygen reactions .....	46
3.4.3 Electrocatalytic nitrate reduction reaction .....	49
3.5 Ion detection.....	51
3.6 Computer simulations .....	53
3.6.1 Computer software .....	53
3.6.2 Modelling details and parameters .....	53
<b>4 N-CNWs/D composites for electrocatalytic ORR .....</b>	<b>55</b>
4.1 Modulation of N-CNWs/D composite nanostructures.....	56
4.2 ORR performance of N-CNWs/D composites .....	63
4.3 Annealing treatment and enhancing ORR performance .....	64
4.4 Effect of an annealing treatment in terms of ORR activity.....	70
4.5 Conclusions .....	77
<b>5 Co<sub>4</sub>N@d-NCNWs/D composites for electrocatalytic ORR/OER and zinc-air batteries .....</b>	<b>79</b>

5.1 DFT calculations of heterointerface and ORR/OER mechanisms .....	81
5.2 Characterization of Co <sub>4</sub> N@d-NCNWs/D composites .....	84
5.3 Electrocatalytic ORR/OER performance .....	93
5.4 Performance of assembled zinc-air batteries .....	101
5.5 Conclusions .....	106
<b>6 Cu-np@BDD-m composites for electrocatalytic NITRR .....</b>	<b>108</b>
6.1 Characterization of Cu-np@BDD-m composites .....	109
6.2 Electrocatalytic NITRR performance .....	114
6.3 DFT calculations of composite interface and NITRR mechanisms .....	118
6.4 Ion accumulation in the nanoconfined area .....	122
6.5 Conclusions .....	123
<b>7 Summary and outlook .....</b>	<b>125</b>
7.1 Summary .....	125
7.2 Outlook .....	126
<b>8 References .....</b>	<b>128</b>
<b>Lebenslauf .....</b>	<b>141</b>
<b>Publikationen.....</b>	<b>142</b>



## Symbol List

### Abbreviations

AC	amplitude current
BDD	boron doped diamond
BEP	Bronsted-Evans-Polanyi
BND	boron nitrogen co-doped diamond
CC	carbon cloth
CHE	computational hydrogen electrode
CNWs/D	carbon nanowalls/diamond composites
CO <sub>2</sub> RR	carbon dioxide reduction reaction
CV	cyclic voltammetry
DFT	density functional theory
DGNSs	diamond/graphite hybrid nanosheets
DOS	density of states
ECSA	electrochemical surface area
EDX	energy dispersive X-ray analysis
EIS	electrochemical impedance spectroscopy
EXAFS	extended X-ray absorption fine structure
FE	degree Celsius per minute
FFT	fast Fourier transform
GC	glassy carbon
GCD	galvanostatic charge-discharge curves
GCE	glassy carbon electrode
GGA	generalized gradient approximation
HER	hydrogen evolution reaction
HFCVD	hot filament chemical vapor deposition
LAPW	linearized augmented plane wave
LDA	local density approximation
LSV	linear sweep voltammetry
MPCVD	microwave plasma chemical vapor deposition
NC	nano carbon
NCD	nanocrystalline diamond films

NCP	norm-conserving pseudopotential
ND	nanodiamond
NITRR	nitrate reduction reaction
NRR	nitrogen reduction reaction
OCP	open-circuit potential
OER	oxygen evolution reaction
ORR	oxygen reduction reaction
PAW	plane wave pseudopotential
PTFE	polytetrafluorethylene
PVD	physical vapor deposition
RDE	rotating disk electrode
RHE	reversible hydrogen electrode
SCA	static water contacts angles
SCE	saturated calomel electrode
SEM	scanning electron microscopy
SMSI	strong metal-supporting interaction
SSA	specific surface area
TEM	transmission electron microscope
TS	transition state
UPS	ultraviolet photoelectron spectroscopy
USPP	ultrasoft pseudopotential
VASP	Vienna <i>ab initio</i> simulation package
VGs	vertical graphene sheets
WF	work function
XANES	X-ray absorption near-edge structure
XAS	X-ray absorption spectroscopy
XPS	X-ray photoelectron spectroscopy
XRD	X-ray diffraction
ZABs	zinc-air batteries

**Chemicals**

Al	aluminum
----	----------

---

$\text{Al}_2\text{O}_3$	aluminum oxide
Ar	argon
$\text{CH}_4$	methane
$\text{CO}_2$	carbon dioxide
Cu	copper
$\text{Co}_4\text{N}$	cobalt nitride
$\text{Co}(\text{NO}_3)_2 \cdot 6\text{H}_2\text{O}$	cobalt nitrate hexahydrate
$\text{Co}(\text{OH})_2$	cobalt hydroxide
CoPc	cobalt phthalocyanine
He	helium
$\text{H}_2$	hydrogen
$\text{H}_2\text{O}_2$	hydrogen peroxide
$\text{H}_2\text{O}$	water
$\text{H}_3\text{PO}_4$	phosphoric acid
HCl	hydrochloric acid
Hg	hydrargyrum
$\text{HgCl}$	mercury chloride
$\text{HgO}$	mercury oxide
$\text{KNO}_3$	potassium nitrate
KOH	potassium hydroxide
$\text{N}_2$	nitrogen
$\text{NaClO}$	sodium hypochlorite
$\text{Na}_2\text{SO}_4$	sodium sulfate
$\text{NaNO}_3$	sodium nitrate
NaOH	sodium hydroxide
$\text{NH}_3$	ammonia
Ni	nickel
$\text{O}_2$	oxygen
Pt/C	platinum on carbon
$\text{RuO}_2$	ruthenium oxide
Si	silicon
Ti	titanium

**Symbols**

$a$	lattice constant of supercell
$b$	lattice constant of supercell
$\Delta E$	potential difference
$\Delta H$	enthalpy change
$a$	position of the transition state
$C_{\text{dl}}$	double-layer capacitance
$C_0$	bulk concentration
$D_0$	diffusion coefficient
$E$	energy of the system
$E_{1/2}$	half-wave potential
$E_{10}$	overpotential
$E_a$	activation energy
$E_0$	initial energy
$E_{\text{onset}}$	onset potential
$E_p$	barrier of reactions
$E_R$	barrier of reactions
$E'_{\text{xc}} [n(\vec{r})]$	exchange-correlation generalization
$F$	faraday constant
FWHMs	full width at half maximum
$j_L$	diffusion limiting current density
$j_k$	kinetic current
$m_e$	mass of electrons
$M$	molar mass
$M_I$	mass of nuclei
$n$	number of transferred electrons
$n(\vec{r})$	electron number density
$\eta$	overpotential
$Q$	total charge
$\vec{T}_i$	position coordinates of electrons
$\vec{R}_I$	position coordinates of nuclei
$S$	geometric area

$t$	time
$T_e$	kinetic energy of the electrons
$T_n$	kinetic energy of the nuclei
$T[n(\vec{r})]$	kinetic energy generalization
$\nu$	kinetic viscosity
$V$	volume of the electrolyte
$V_e$	potential energy of the electrons
$V_n$	potential energy of the nuclei
$V_{e-n}$	potential energy for the interaction between electrons and nuclei
$H$	Hamiltonian operator
$\Psi(T, \vec{R})$	wavefunction
$\chi(\sigma)$	spin wavefunction

### Units

$^\circ$	degree
$^\circ\text{C}$	degree Celsius
$^\circ\text{C}/\text{min}$	degree Celsius per minute
$\Omega$	ohm
$\mu\text{m}$	micrometer
$\mu\text{F}$	microfarad
$\mu\text{L}$	microliter
A	ampere
$\text{\AA}$	Ångström
cm	centimeter
$\text{cm}^{-1}$	per centimeter
$\text{cm}^2$	square centimeter
$\text{cm}^2 \text{ s}^{-1}$	square centimeter per second
$\text{C mol}^{-1}$	coulomb per mole
eV	electron Volt
$\text{eV } \text{\AA}^{-1}$	electron Volt per Ångström
g	gram

---

h	hour
kV	kilovolt
kW	kilowatt
mbar	millibar
mF cm <sup>-2</sup>	millifarad per square centimeter
mg cm <sup>-2</sup>	milligram per square centimeter
mg h <sup>-1</sup> cm <sup>-2</sup>	milligram per hour per square centimeter
mL	milliliter
min	minute
mm	millimeter
mM	millimole per liter
mol cm <sup>-3</sup>	mole per cubic centimeter
mAcm <sup>-2</sup>	milliampere per square centimeter
mV	millivolt
mV/s	millivolt per second
mV dec <sup>-1</sup>	millivolt per decade
mW cm <sup>-2</sup>	milliwatt per square centimeter
M	mole per liter
MHz	megahertz
nm	nanometer
Pa	pascal
rpm	revolutions per minute
s	second
sccm	standard cubic centimeter per minute
V	volts
V/s	volts per second
wt%	mass percentage concentration
W	watt

## Abstract

Electrocatalysis of small molecules is a sustainable solution to help the global energy crisis and meanwhile to reduce environmental pollution. The key to reduce energy losses during the electrocatalytic processes is the rational design of efficient and robust electrocatalysts under practical operation conditions. However, commercial metal based catalysts such as Pt/C and RuO<sub>2</sub> are suffer from their high costs, scarcity, susceptibility to poisoning, and single reaction sites, limiting their large-scale applications. Moreover, the most common catalytic reactions of small molecules such as oxygen reduction/evolution reaction (ORR/OER), CO<sub>2</sub> reduction reaction (CO<sub>2</sub>RR) and nitrate reduction reaction (NITRR) are multi-electron reactions, where sluggish kinetics exist together with complex reaction pathways. Such traditional single metal active sites are not sufficient to overcome such challenges. Therefore, it is urgent to deeply understand the reaction mechanisms, to design the heterogeneous catalysts, to tune the structure and composition of the multiple components.

Diamond-based electrodes have been widely employed in electrochemical sensing and advanced electrocatalytic oxidation of pollutants, due to their broad potential windows, low background currents, high chemical stability, and resistance to toxication. As for the electrocatalysis of small molecules, the broad potential window means the thermodynamic inhibition of hydrogen evolution, which ensures the selectivity of ORR, CO<sub>2</sub>RR and NITRR. Meantime, the robust structure provides sufficient stability and recycling possibilities in extreme environments. However, the diamond-based electrodes feature poor electrocatalytic performance, due to the lack of active sites. Creation of or the increase of active sites together with the balance of their activity and stability still remains challenging.

This thesis combines the density functional theory (DFT) calculations with experiments to construct efficient and robust diamond composites, which are employed as the catalysts for the electrocatalysis of small molecules such as oxygen and nitrate. Deep understanding of the relationship between catalyst structures and electrocatalytic

performance is further desired to develop their practical application in energy devices.

Concerning the oxygen electrocatalysis, namely, the ORR and OER, the nitrogen doped carbon nanowalls/diamond (N-CNWs/D) composites are synthesized by means of microwave plasma enhanced chemical vapor deposition (MPCVD) technique, consisting of a thin nanodiamond layer at the bottom and a vertically aligned multigraphene on the surface. After annealing post-treatment, the composites feature superior ORR performance (high onset potential of 835 mV vs. Standard hydrogen electrode, RHE) and excellent stability (90% current retention after 20 h). It is attribute to the activated and exposed edge sites and a bonded nanodiamond layer. The Co<sub>4</sub>N@d-NCNWs/D composites are further synthesized and employed as the ORR/OER bifunctional catalysts. In more detail, the DFT calculations predict that the enhanced metal-supporting interaction between the Co<sub>4</sub>N and d-NCNWs/D promotes the anchoring and dispersion of the Co<sub>4</sub>N nanoparticles. It also adjusts the electronic structures of Co and C atoms at the interface, reducing the overpotential of ORR/OER from 0.67 to 0.23 eV. Experimentally, the composites feature superior ORR/OER bifunctional performance (e.g., a small potential gap of 0.75 V). Since these composites are directly grow on carbon cloth collectors, they are utilized as air electrodes. The assembled flexible zinc-air batteries exhibit a high open circuit voltage of 1.41 V and excellent bending stability.

With respect to the nitrate electrocatalysis, the copper nanoparticles coated boron-doped diamond mesh (Cu-np@BDD-m) composites are synthesized by means of hot-filament chemical vapor deposition (HFCVD) and magnetron sputtering. After the application of an etching process at a low pressure, Cu nanoparticles are embedded in the BDD-m surface, leading to a strong metal-supporting interaction or a nanoconfined trapping area. The DFT calculations reveal that this strong interaction enhances the adsorption of nitrogen-contained intermediates (e.g., \*NO<sub>3</sub>, \*NO<sub>2</sub>, \*N), minimizes the reaction energy through NITRR from 1.06 to 0.91 eV, and raises the energy barrier of competing HER from 0.50 to 0.97 eV at a neutral medium. Consequently, the composite



features superior NITRR performance (e.g., nitrate removal of 90.2% and ammonia selectivity of 76.8%). The resultant nano-confined area stabilizes the active sites and enhanced the local adsorption of nitrate, eventually upshifting the diffusion-controlled first-step onset potential (from -0.25 to 0.1 V vs. RHE). In this way, the NITRR mechanism is elaborated in thermodynamic and kinetic processes. Such an electrode promises to assemble liquid flow reactors for sustainable applications.

In summary, efficient and robust diamond composites based catalysts are fabricated for the electrocatalysis of small molecules such as oxygen and nitrate. The balance of their activity and stability is achieved *via* the construction of the rational support structure, the modification of the active sites on the surface, and the enhancement of the metal-supporting interactions. The catalyst design approach proposed in this thesis is promising to be applied for the electrocatalysis of other small molecules and further for the assembly of energy devices of practical applications in future.

# 1 Introduction

## 1.1 Electrocatalysis of small molecules

Searching of renewable energy sources has become a huge challenge on account of rapid energy consumption and increasing global demands. The electrocatalysis of energy-related small-molecules (e.g.,  $\text{H}_2\text{O}$ ,  $\text{N}_2$ ,  $\text{CO}_2$ ,  $\text{NO}_x$ ) has attracted a wide range of interest (**Figure 1.1**). For instance, water electrolysis ( $2\text{H}_2\text{O} \rightarrow 2\text{H}_2 + \text{O}_2$ ) is a reaction that enables the utilization of renewable electrical energy to produce green fuel energy (namely  $\text{H}_2$  and  $\text{O}_2$ ) without the emission of harmful gases [1-3]. Furthermore, the generated  $\text{H}_2$  can also serve as an important feedstock for ammonia synthesis (namely  $\text{N}_2 + 3\text{H}_2 \rightarrow 2\text{NH}_3$ ) in agriculture and the chemical industry [4-6]. while the produced oxygen can be reused as a fuel resource for batteries (e.g., fuel cells and metal-air batteries) to convert chemical energy into electrical energy, allowing for a sustainable energy cycle [7-9]. Although the efficiencies of these energy conversion systems are affected by many factors, the development of efficient and stable catalysts is the core during the electrocatalysis of small molecules. In the past few years, tremendous efforts have been thus made to design the geometrical and electronic structures of catalysts [10-12]. However, there is still a lack of explanation about the relationship between the reaction mechanisms on the real active sites and effective structures of the catalysts.

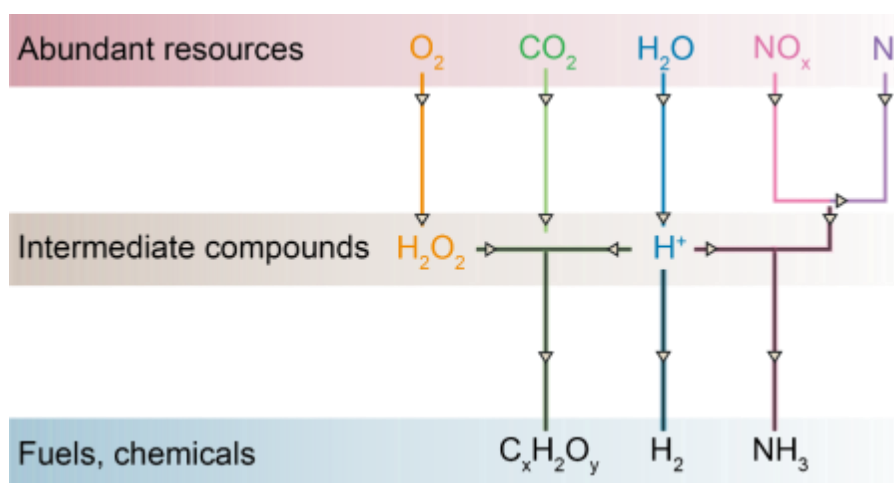


**Figure 1.1.** Schematic illustration of possible electrocatalytic pathways for energy-related small-molecules.

### 1.1.1 Challenges in electrocatalysis of oxygen

There are at least two types of oxygen reactions, namely oxygen reduction reaction (ORR) and oxygen evolution reaction (OER). They are essential reactions for fuel cells and metal-air batteries, regarded as ideal energy conversion and storage devices in the future (**Figure 1.2**). However, both of them are sluggish kinetics, due to the involvement of 4 electrons in multi-steps. The high overpotential of the ORR and OER eventually inhibits the energy conversion efficiencies of the devices. It is known that commercial Pt/C and RuO<sub>2</sub> feature superior ORR and OER activity, respectively. Their high costs, scarcity, susceptibility to poisoning, and single active site unfortunately limit their large-scale applications. Therefore, developing a sustainable, robust, and efficient non-noble heterogeneous catalyst is vital for the electrocatalysis of oxygen molecules.

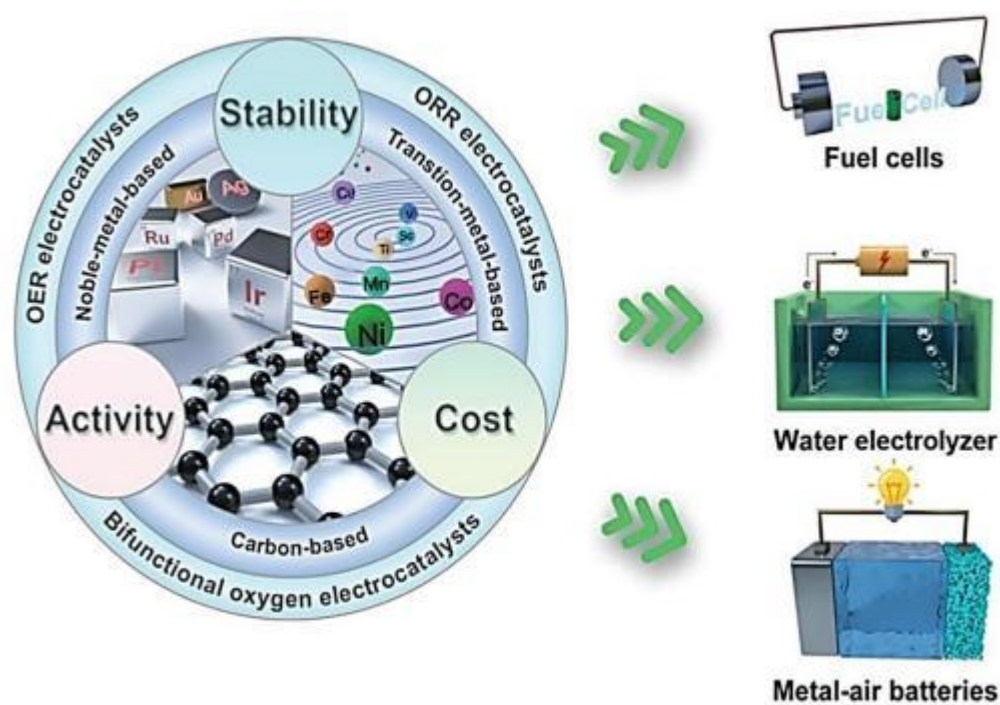


**Figure 1.2.** Applications of electrocatalytic oxygen reactions for energy conversion and storage devices [13]. Copyright 2020, Wiley-VCH.

### 1.1.2 Challenges in electrocatalysis of nitrate

Ammonia is both a significant chemical for fertilizer production and a promising energy carrier for energy conversion. The traditional approach of ammonia synthesis is

so-called Haber-Bosch process, which involves the intensive consumption of fossil energy and carbon dioxide emission. Different from this approach, electrocatalytic synthesis of ammonia has attracted tremendous attention very recently as a green technology. Compared with the nitrogen reduction reaction (NRR), which is significantly suppressed by the energy barriers to nitrogen dissociation [14], the reduction reaction of nitrate to ammonia is thermodynamically favorable for the practical applications. In addition, the electrocatalytic nitrate reduction reaction (NITRR) is an essential step towards a sustainable nitrogen cycle resolving the nitrate enrichment (**Figure 1.3**), which is caused by the over-utilization of fertilizers and industrial sewage discharge, to achieve the goal of “turning waste into treasure” [15, 16]. However, the NITRR is complex since it is an eight-electron process and competes thermodynamically with the hydrogen evolution reaction (HER). Improving the activity, selectivity and stability of sustainable ammonia production remains a challenge. Deep understanding of the mechanism of the NITRR is required for rational design of different catalysts.

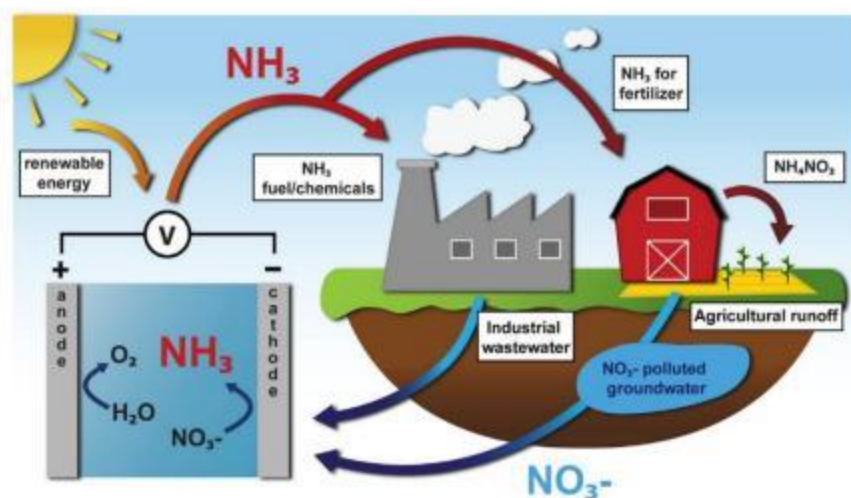


**Figure 1.3.** Sustainable nitrogen cycle resolving the nitrate enrichment [5]. Copyright 2020, Elsevier Inc.

## 1.2 Development of diamond composite catalysts

Diamond has been increasingly investigated for electrocatalytic applications

because of its chemical inertness, high corrosion resistance, wide electrochemical potential window and low background current [17, 18]. Early researches have demonstrated that a diamond electrode possesses much higher chemical inertness and corrosion resistance than a graphite and glassy carbon (GC) electrode during potential cycling in an extreme environment [19]. Moreover, the high oxygen evolution overpotential allows the enriched hydroxyl radicals on the surface for electrocatalytic oxidation reactions. In contrast, the negative hydrogen evolution potential ensures good selectivity in some electrocatalytic reduction reactions, such as ORR, nitrogen reduction reaction (NRR), CO<sub>2</sub> reduction reaction (CO<sub>2</sub>RR) and the NITRR. Unfortunately, diamond electrodes suffer always from their inert surface properties and poor electrochemical activity. To overcome these shortcomings, commonly reported methods are doping [20], surface modification [21-23], and multi-stage nanostructure formation.

For example, the boron-doped diamond (BDD) has been widely used for anodic electrocatalytic oxidation of pollutants, due to its good conductivity, chemical stability and rich boron active sites [24, 25]. It has been suggested that the electrochemical catalytic performance can be enhanced by modulating the boron dopants, the ratio of sp<sup>3</sup>/sp<sup>2</sup> and its surface terminations [26]. Three-dimensional BDD nanostructures (e.g., BDD foam) have been produced and applied in cathodic catalytic reactions [27]. For instance, Zhang et al. prepared porous BDD catalysts on the nickel foam substrate for the electrocatalytic ORR (**Figure 1.4a, b**). They explored the relationship between specific surface areas (SSAs) and the catalytic performance in alkaline solutions [28]. The SSA of the catalyst was found to be directly proportional to the ORR activity and inversely to the durability and methanol resistance (**Figure 1.4c, d**). Furthermore, Liu et al. stated that the nanostructured BDD has an enlarged surface area and induces a charge accumulation effect on the needle tip [29] (**Figure 1.4e, f**). The synthesized electrode exhibited superior NRR activity and excellent stability (**Figure 1.4g, h**).

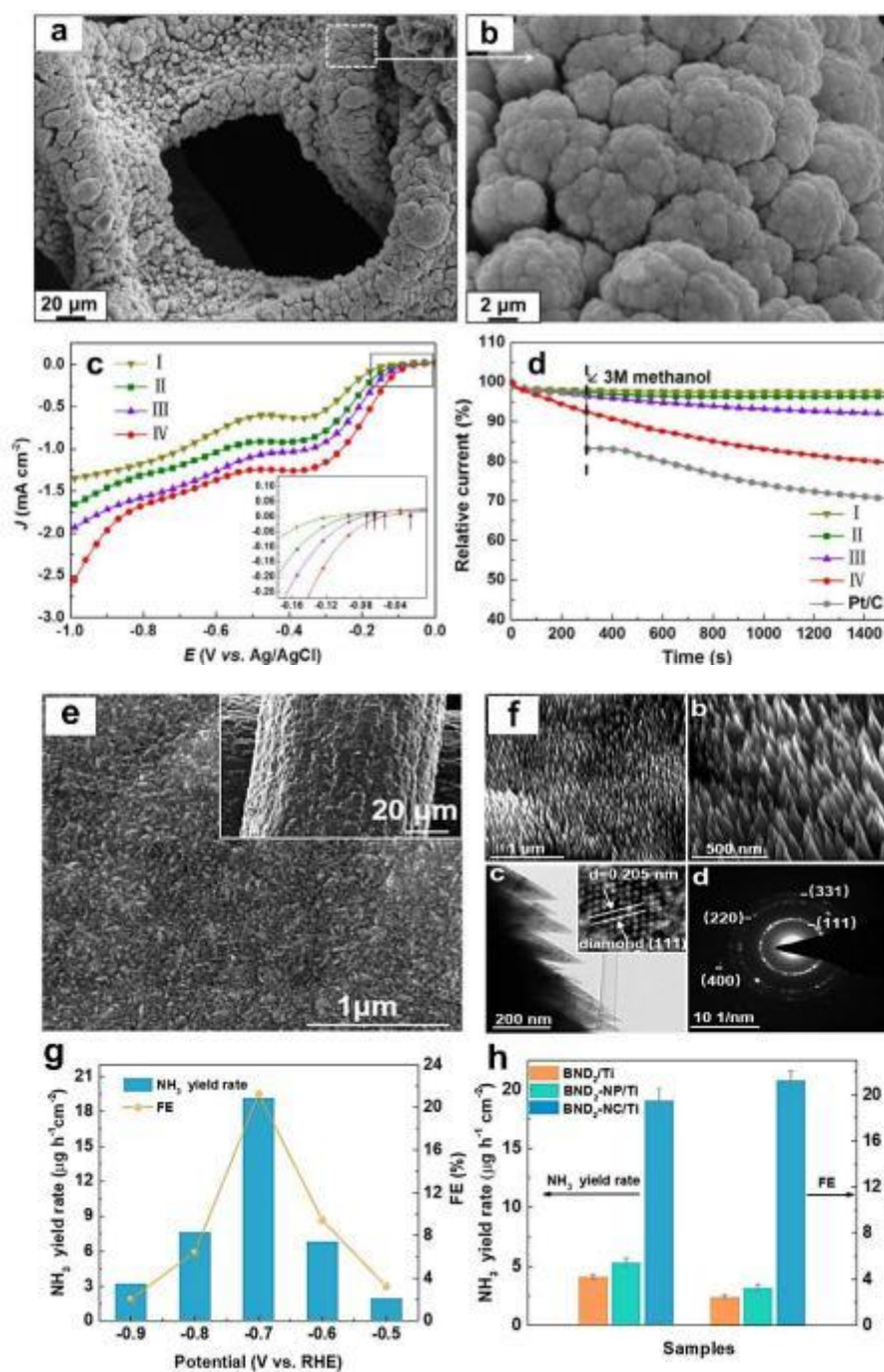


**Figure 1.4.** (a, b) SEM images of BDD catalysts deposited on foam nickel substrates. (c) LSV curves of the BDD catalysts. (d) Methanol tolerance of the BDD catalysts [28]. Copyright 2017, Elsevier. (e) SEM image of a BND<sub>2</sub>/Ti electrode. (f) Morphology and physical structure of BND<sub>2</sub>-NC/Ti electrode. (g) NH<sub>3</sub> yield rates and FEs of BND<sub>2</sub>-NC/Ti electrode. (h) Comparison of NH<sub>3</sub> yield rates and FEs of BND<sub>2</sub>/Ti, BND<sub>2</sub>-NC/Ti and BND<sub>2</sub>-NP/Ti electrodes [29]. Copyright 2020, American Chemical Society.

Another approach to enhance the electrocatalytic performance of diamond electrodes is to introduce graphite into diamond. For example, N-doped Diamond/graphite hybrid nanosheets (DGNSs) epitaxially grown on boron-doped diamond (BDD) films [30] (**Figure 1.5a, b**) exhibited electrocatalytic performance toward the ORR, which was further enhanced after their doping with nitrogen. The NDGNSs doped at 650 °C with  $\text{NH}_3$  in a tube furnace showed higher electrocatalytic activity and stability toward the ORR than the commercial Pt/C catalyst (**Figure 1.5c, d**). The vertical graphene sheets (VGs) with edge defects have been formed as catalyst centers on separated papillary granules of nanocrystalline diamond films (NCD) [31] (**Figure 1.5e, f**). Such a composite showed enhanced ORR performance, due to the exposed edge sites and the efficient air/solid/solution tri-interface with a medium static contact angle (**Figure 1.5g, h**).

These diamond-core graphite-shell structures combine excellent stability with superior chemical activity, meeting the requirements for practical applications of diamond catalysts. For example, the ND@G composites were synthesized by a simple method, followed by the Ar annealing of nanodiamonds [32, 33]. As essential candidates of electrocatalysts, this composite featured a large surface area and abundant defects on the graphene, thus improving the adsorption of oxygen (**Figure 1.6a-d**). In addition, doped ND@G composite and other graphene-like structures were obtained by varying the annealing treatment atmosphere and annealing temperature. For example, after annealing of ND at a temperature as high as 1550 °C for 6 h, a hND composite catalyst was achieved (**Figure 1.6e**). After exfoliation and nitridation, the N-exhND possessed N-doped edges at the shell and  $\text{sp}^3$ -hybridized diamond structure at the core, conceived a synergic effect with a considerably enhanced ORR activity and outstanding stability (**Figure 1.6f, g**) [33].



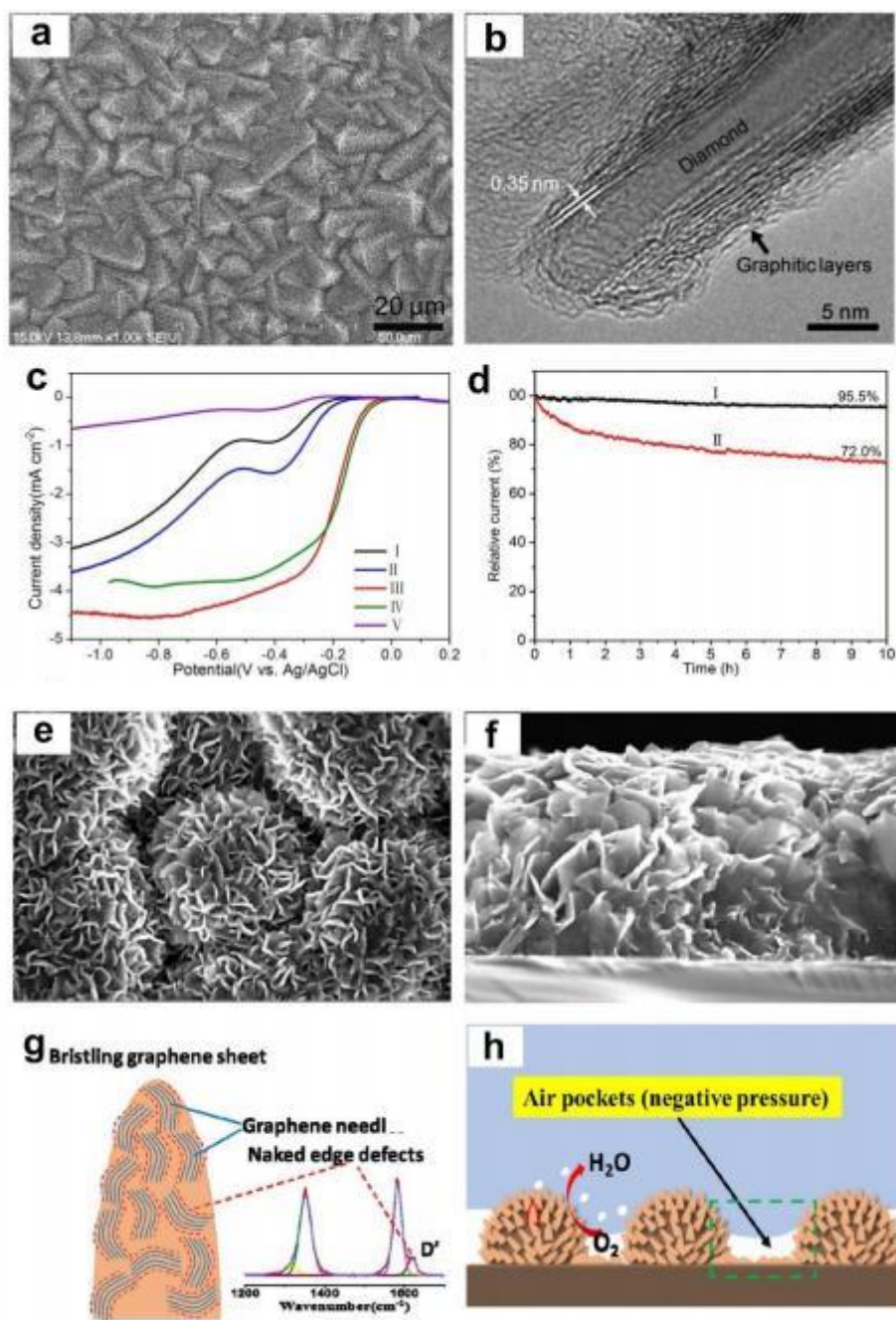


**Figure 1.5.** (a) SEM image and (b) HRTEM image of the DGNSs grown on BDD films. (c) LSV curves of the NDGNSs films and Pt/C. (d) Long term stability of NDGNSs films and Pt/C [30]. Copyright 2018, American Chemical Society. (e) Front image and (f) Sectional image of the VG-on-SPF-NCD electrode. (g) The typical vertical graphene sheets with large numbers of naked edge defects for high efficiency ORR catalysis. (h) The possible Cassie-Wenzel contacting state and ORR reaction happen on liquid/solid interface [31]. Copyright 2020, Elsevier.



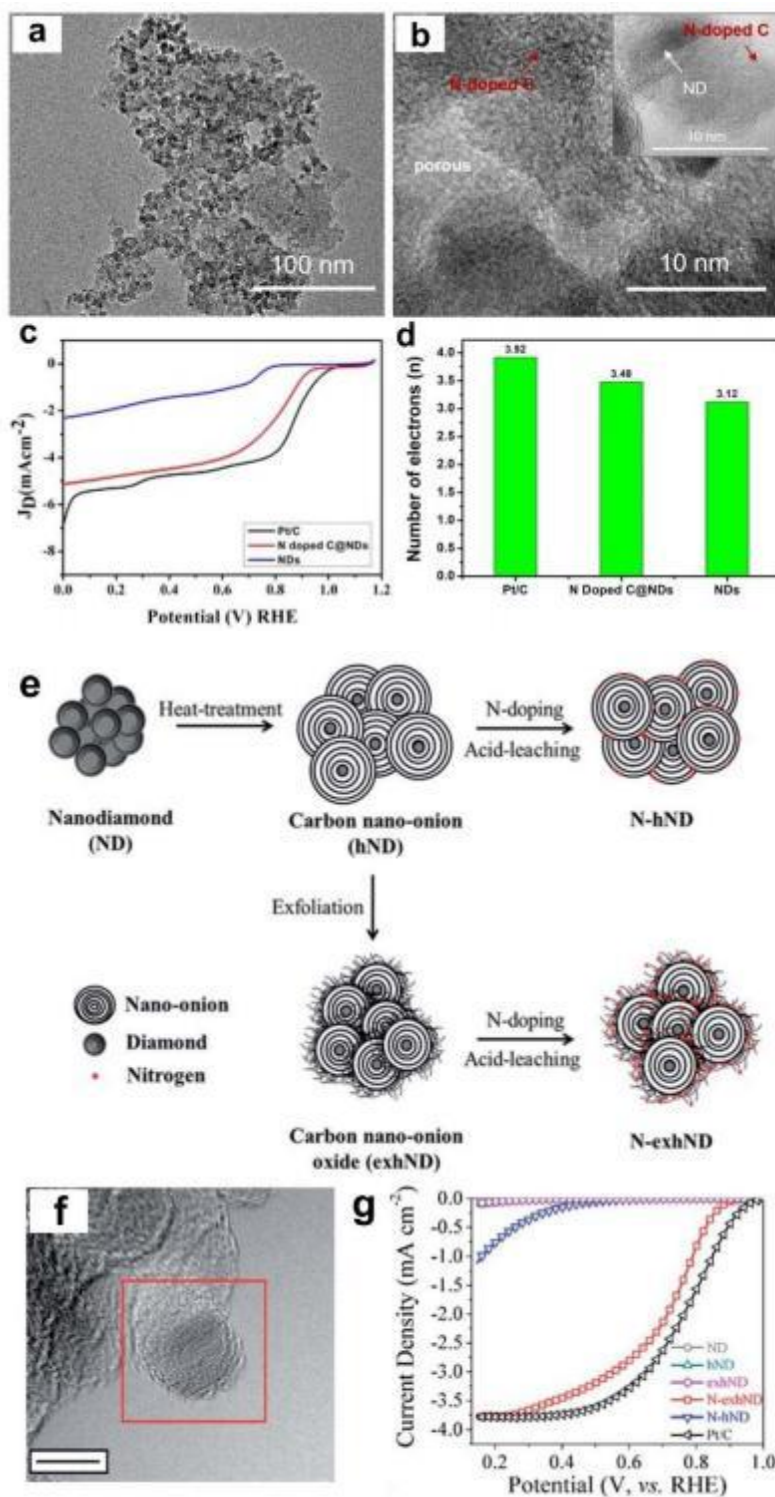


**Figure 1.6.** (a, b) TEM images of N-doped C@NDs. (c) LSV curves of NDs, N-doped C@NDs and Pt/C. (d) Electrons transferred number of NDs, N-doped C@NDs and Pt/C [32]. Copyright 2020, IOP Publishing. (e) Schematic diagram of the catalyst preparations. (f) TEM image of N-exhND. (g) LSV curves of N-exhND and Pt/C [33]. Copyright 2016, The Royal Society of Chemistry.

Furthermore, the NG@D composite mentioned above was employed to modify metal nanoparticles [34-37]. Huang et al. stated that an atomically dispersed copper catalyst supported on a defective nanodiamond-graphene (ND@G) substrate exhibited excellent catalytic performance toward selective conversion of acetylene to ethylene [38] (**Figure 1.7**). The unique structural feature of Cu atoms anchored over graphene through the Cu-Cbond ensured the effective activation of acetylene and easy desorption of ethylene. In this case, the ND@G substrate served as not only a robust support for stability, but also interacted with the anchored metal nanoparticles, which cannot be observed on the inert diamond substrate [39]. This so-called strong metal-supporting interaction (SMSI) is thus expected to promote a homogeneous dispersion of the metal nanoparticles and induce interfacial effects that modulate the intrinsic activity of active sites. Although such interactions have been further studied on metal oxide supporters in the last decades [40-43], they have not been proposed in diamond composite catalysts.

In summary, diamond composite, a unique  $sp^3$  carbon involved material, is a promising electrocatalyst that still needs further research. The rational design of its three-dimensional nanostructure, the control of the ratio between diamond and graphite phases, and the investigation of the effect of metal-supporting interactions on its catalytic activity shall be studied. Deep understanding of the relevant mechanisms is significant to design novel diamond composite catalysts that feature high activity and stability.

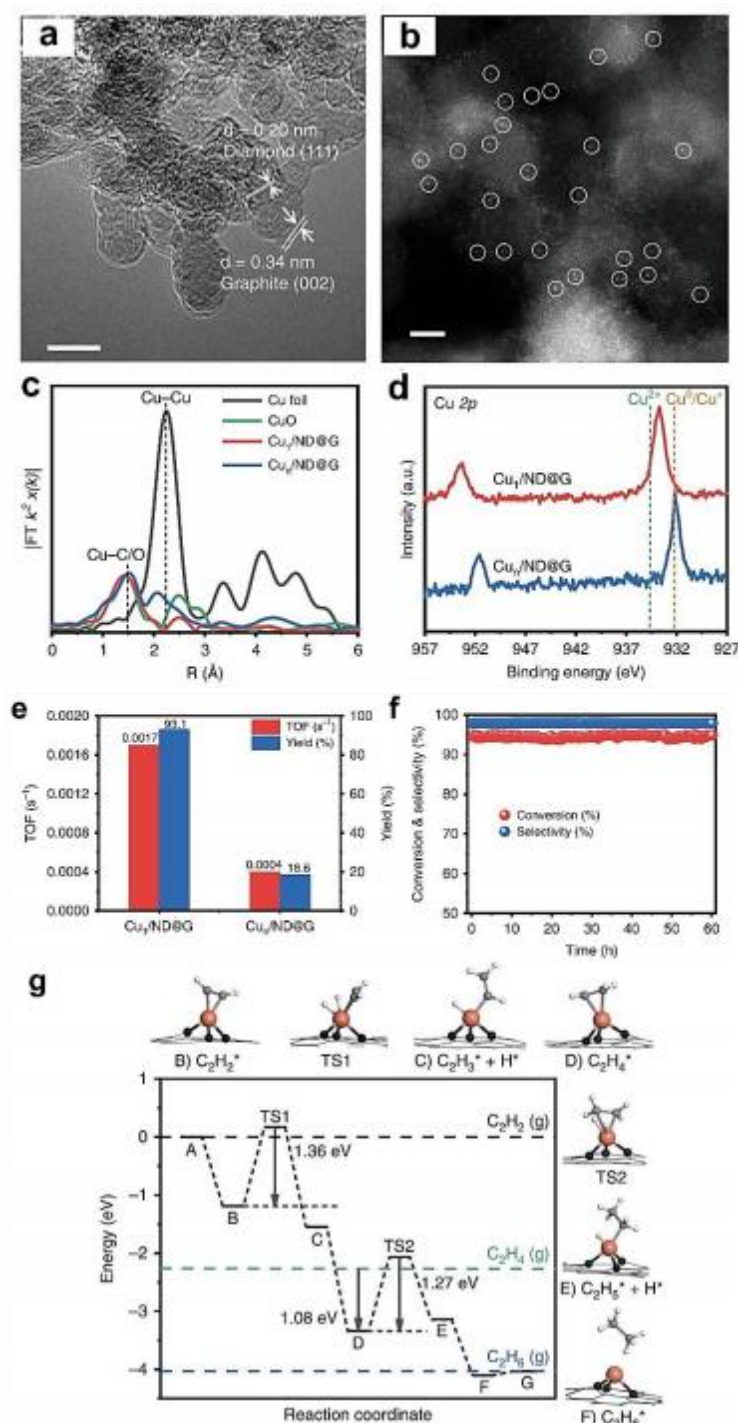


**Figure 1.7.** TEM images of (a) ND@G support and (b) Cu<sub>1</sub>/ND@G catalyst. (c) Cu K-edge EXAFS spectra in R space for Cu<sub>1</sub>/ND@G. (d) Cu 2p XPS of Cu<sub>1</sub>/ND@G and Cu<sub>0</sub>/ND@G. (e) TOF values and ethylene yields of the catalysts. (f) Durability test on Cu<sub>1</sub>/ND@G. (g) Energy profile of acetylene hydrogenation on the Cu<sub>1</sub>/ND@G catalyst and the structures of intermediates and transition states [38]. Copyright 2019, Nature Publishing Group.

### 1.3 Motivation of the thesis

From the above discussion, it is clear that the design of efficient and robust catalysts for oxygen electrocatalysis and ammonia synthesis is highly desired. In this respect, suitable catalysts are expected to significantly reduce energy loss during energy conversion, eventually meeting the demands of the commercial development of new energy devices and valuable products.

As for the design of efficient catalysts, the critical approach is to improve the intrinsic activity and the density of available active sites on the catalyst surface. Therefore, many efforts have made to adjust the morphology, surface properties and electronic structures of different catalysts. Note that the heterogeneous interfacial environment of the composites is especially vital. An ideal reaction interface must provide efficient electron transport pathways, large specific surface areas for ion and mass transport, and intensively exposed intrinsic active sites.

The focus of this thesis is thus to construct efficient and robust diamond composite catalysts and explore their practical applications. Centering on this focus, three different approaches have been proposed in this thesis:

- (1) Design of novel diamond composite catalysts for efficient and stable oxygen electrocatalysis and ammonia synthesis;
- (2) Combination of the density function theory (DFT) calculations with experimental results to deeply understand electronic structures of active sites and reaction mechanisms, eventually to reveal the structure-performance relationships of as-designed catalysts;
- (3) Exploration of practical applications of as-synthesized catalysts in next-generation electronic devices.

### 1.4 Overview of the thesis

This thesis consists of 7 chapters.

Chapter 1 introduces the challenges of electrocatalysis of small molecules, such as

oxygen and nitrate. The development of diamond composite catalysts is described. The motivations to design efficient and robust diamond composite electrocatalysts and employ theoretical DFT calculations for the exploration of the reaction mechanisms in this thesis are clarified.

Chapter 2 elaborates on the basic concepts of electrocatalyst design, such as the Sabatier principle and the D-band theory. The electrocatalytic pathways of oxygen and nitrate reactions are precisely described. The theoretical base of the DFT calculations is outlined.

Chapter 3 presents experimental methods that have been employed for this thesis. The used techniques for the preparation and characterization of synthesized diamond composites are described. The electrochemical measurements and the ion detection methods are covered in detail. The software and model parameters used for DFT calculations are listed.

Chapter 4 displays physical structures and chemical compositions of the nitrogen doped carbon nanowalls/diamond (N-CNWs/D) composites that are grown using a microwave plasma enhanced chemical vapor deposition (MPCVD) method under various deposition parameters. The ORR performance on the N-CNWs/D composites is systematically collected. The main reasons for their boosted ORR performance after annealing post-treatment are elaborated.

Chapter 5 shows the preparation of the  $\text{Co}_4\text{N}@d\text{-NCNWs/D}$  composites and their applications as bi-functional catalysts toward both the ORR and OER. The details of employing DFT calculations to design heterointerface and discuss structure-performance relationship are summarized. Finally, the assemble of aqueous and flexible zinc-air batteries with the  $\text{Co}_4\text{N}@d\text{-NCNWs/D}$  composites is described. The applications of such batteries to operate elastic wristbands are demonstrated.

Chapter 6 concentrates on the design of  $\text{Cu-np@BDD-m}$  composites toward electrocatalytic NITRR with high efficiency and selectivity. The DFT calculations elaborate the reaction mechanism of the NITRR on the heterointerface. Furthermore,

an implicit solution model is employed to study local ion accumulation in the nanoconfined area.

Chapter 7 summarizes the major findings of this thesis in terms of efficient and robust electrocatalyst design and a deep understanding of reaction mechanisms of small molecules (here oxygen and nitrate). The perspectives and future research directions of the electrocatalysis of small-molecule on composite catalysts are discussed and outlined.

## 2 Theoretical fundamentals

### 2.1 Concepts of electrocatalyst design

#### 2.1.1 Sabatier principle and volcano curve

In 1913 Paul Sabatier proposed for the first time that [44] an ideal catalyst should bind to the reactant at an intermediate strength which is neither too weak nor too strong. If the bond is too weak, the catalyst and the reactant will hardly interact with each other. While if the bond is too strong, the product will not desorb from the catalyst surface, thus inhibiting further reactions. However, this principle was based only on qualitative analysis at that time. There were no methods to calculate the binding energies between the catalysts and intermediates. Therefore, the Sabatier principle was also named as Balance principle (**Figure 2.1**). It provides the foundation for the subsequent theory of ideal catalyst design.

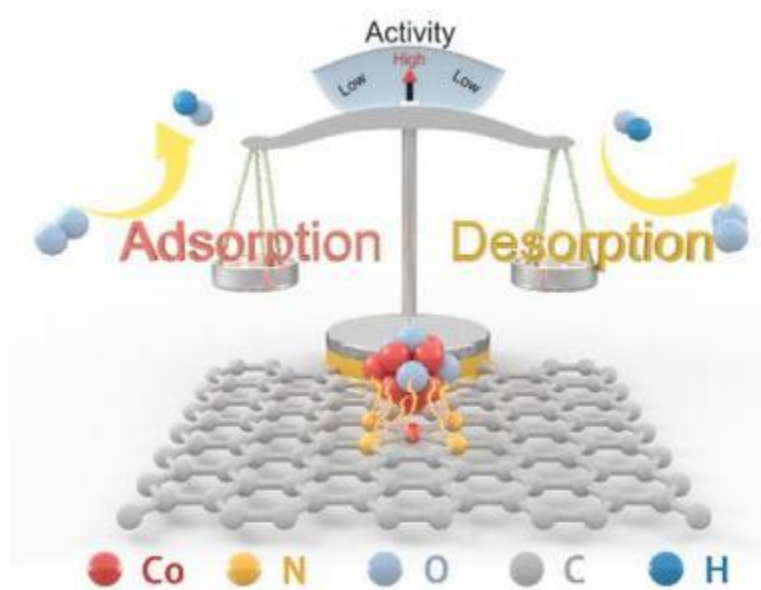


**Figure 2.1.** Schematic illustration of the binding energy between catalyst and reactants [45]. Copyright 2021, Elsevier Ltd.

Until 2004, Nørskov and co-workers introduced the computational hydrogen electrode (CHE) model. It opened up the quantitative calculation of the free-energy landscape of an electrocatalyst by computational techniques [46]. This model

substitutes the free energy of an electron-proton pair with that of half a hydrogen molecule at  $U = 0$  V (vs. RHE, reversible hydrogen electrode). Using this method, it is possible to determine the free energies of reaction intermediates as a function of the applied electrode potential and a fixed pH by use of posteriori analysis. When the free energies of reaction intermediates are obtained by DFT at the zero electrode potential and  $\text{pH} = 0$ , they can be further shifted to any electrochemical conditions, based on this CHE model. Using this simple model, the free energies of ORR on different catalysts were calculated. The relationship between the binding energies of intermediates and their electrocatalytic performance was depicted, so-named as the volcano curve (**Figure 2.2**). To date, the volcano curve has been derived and optimized to become one of the critical indicators for screening novel catalysts.

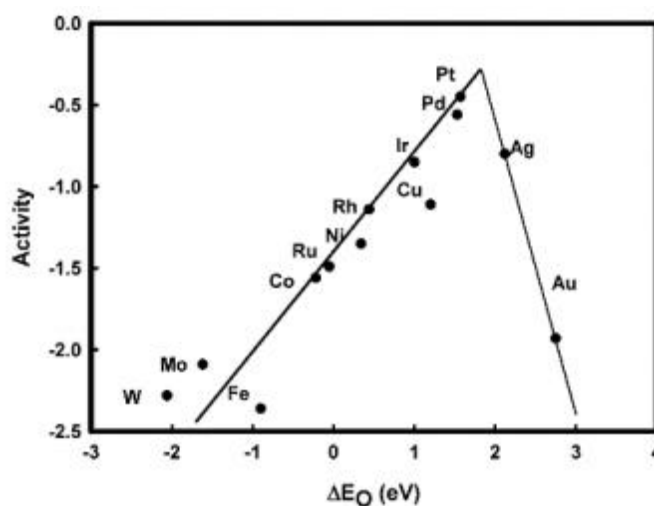


**Figure 2.2.** Relationship between the binding energy of  $\text{O}^*$  and the electrocatalytic performance of ORR [46]. Copyright 2004, American Chemical Society.

### 2.1.2 Linear scaling relationship

It appears relatively easier to investigate the two-electron transfer reactions like HER than reactions that transfer more electrons, such as ORR, OER and NITRR. It is thus essential to deeply understand multi-electron reaction models and further build the relationship between the multi-electron system and the simple one-electron system.

In 2007, Nørskov and co-workers developed the scaling model into a DFT method



in order to estimate a series of dehydrogenation reaction energies for organic molecules on transition-metal surfaces [47]. This method was further applied to the OER, a multi-electron reaction system. They showed that a universal scaling relation between the adsorption energies of  $\text{HOO}^*$  vs  $\text{HO}^*$  makes it possible to analyze the free energy diagrams of all the oxides in a general way (**Figure 2.3**) [48]. This result gave rise to an activity volcano that was the same for various oxide catalysts and a universal descriptor for the OER activity. Furthermore, the thermodynamic theory of these multi-electron transfer reactions based on scaling relationships was discussed, providing optimized volcano curves [49]. This theory can be applied to multi electron transfer reactions, such as  $\text{CO}_2\text{RR}$  and  $\text{NITRR}$ .

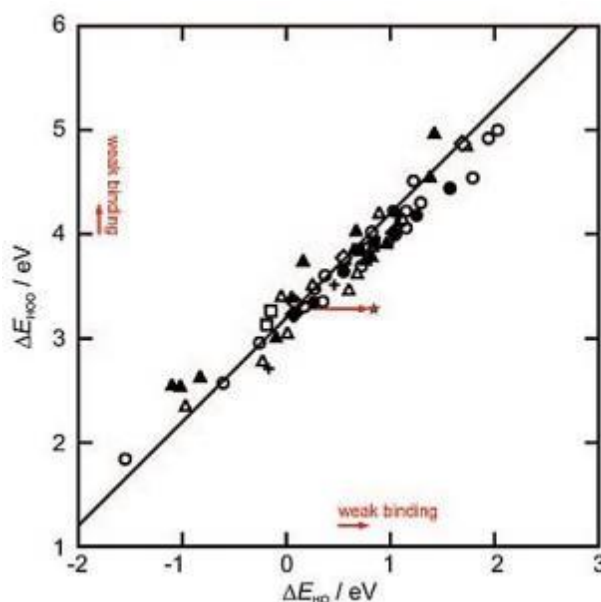


**Figure 2.3.** Adsorption energy of  $\text{HOO}^*$  plotted against the adsorption energy of  $\text{HO}^*$  on different electrodes [48]. Copyright 2011, Wiley-VCH.

Although the scaling relationship and volcano curve enable us to understand the reaction mechanisms of different reactions and screen ideal catalysts, their drawback is that they are usually based on typical materials and thus not suitable for complex systems. Therefore, many efforts have been devoted in recent years to overcome the limiting of linear scaling relationship in order to design higher-performance catalysts

for practical applications [50].

### 2.1.3 Brønsted-Evans-Polanyi relationship

The Brønsted-Evans-Polanyi (BEP) relationship suggests that the activation energy between two reactions is proportional to their enthalpy. This relationship can be expressed as

$$E_a = E_0 + a\Delta H \quad (2.1)$$

where  $E_a$  is the activation energy,  $\Delta H$  is the enthalpy,  $a$  is the position of the transition state along the reaction coordinate. As shown in **Figure 2.4**, TS1 and TS2 are the transition state of the adsorption and the last elementary step of surface association reactions, respectively. The term of  $\Delta H$  is the enthalpy change of the overall reaction. The terms of  $E_R$  and  $E_P$  are the barriers of reactions. It has been suggested that the reaction rate under given reaction conditions shows a maximum as a function of the dissociative adsorption energy of the key reactant. For most situations this maximum is in the same range of reaction energies [51, 52].

The BEP is a linear energy relationship that efficiently calculates the activation energy of many reactions within a distinct family. The activation energy may be used to characterize the kinetic rate parameters of a given reaction by applying the Arrhenius equation.

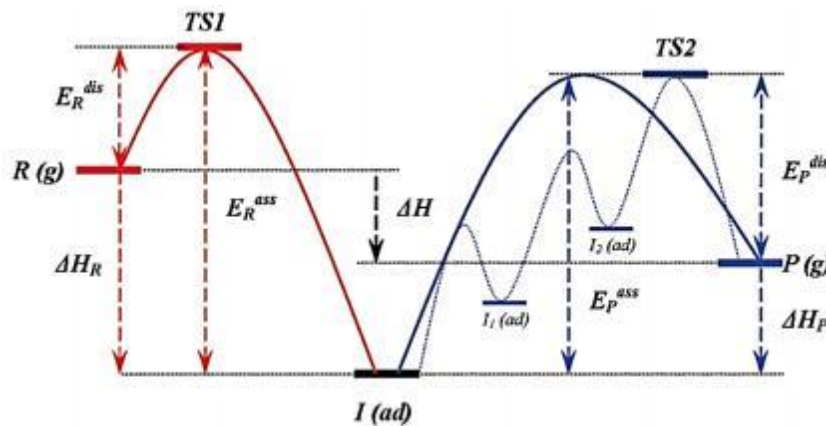


**Figure 2.4.** Illustrative energy profile of the catalytic reaction model [53]. Copyright 2008, American Chemical Society.

### 2.1.4 *d*-band center theory

The *D*-band center theory was first presented by B. Hammer and J. K. Nørskov in 1995 [54]. It is applied to reveal the relationship between the chemisorption energies and the degree of orbital overlap with the adsorbate, which is related to the filling degree of *d*-bands of transition metal catalysts. Precisely, as the adsorbed molecule approaches a metal surface, there is an interaction between the orbitals of an adsorbed molecule and the *s*-, *d*- orbitals of the transition metals. This interaction will lead to energy level spitting, creating bonding and anti-bonding orbitals (**Figure 2.5**). Hence, when the position of antibonding orbitals is above the Fermi level, the probability of electrons fills the antibonding orbitals and becomes smaller, thus enhancing the bonding energy. For example, the self-consistently calculated density of states (DOS) of chemisorbed hydrogen on the Ni, Cu, Pt and Au surfaces were depicted (**Figure 2.6**). The anti-bonding states are above the Fermi level and empty on Ni and Pt. On the contrary, they are essentially filled on Cu and Au. That is why Cu and Au are nobler than Ni and Pt.

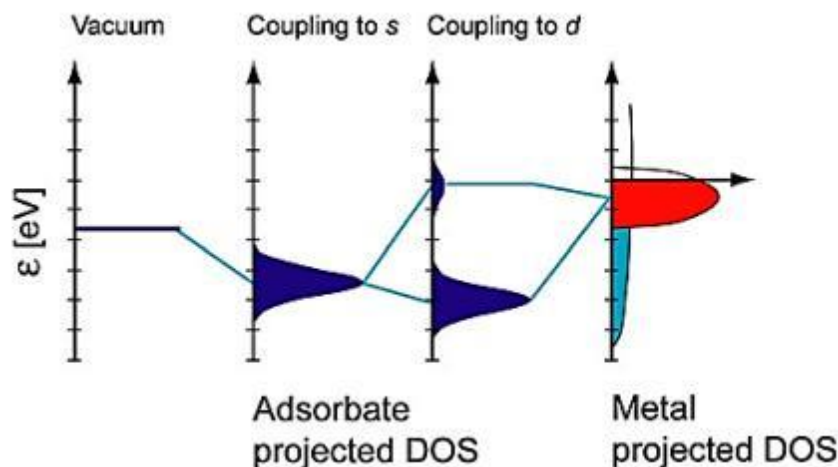


**Figure 2.5.** Schematic illustration of the formation of a chemical bond between an adsorbate valence level and the *s*, *d* states of a transition metal surface [55]. Copyright 2011, National Academy of Science.

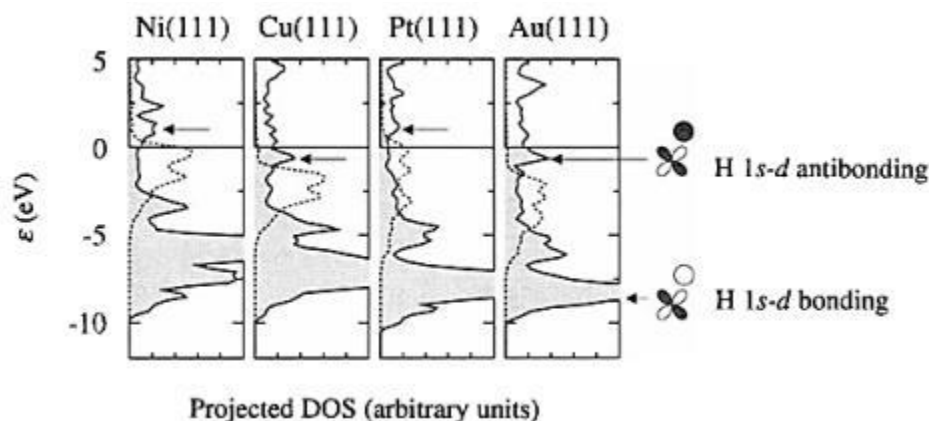


**Figure 2.6.** The density of one-electron states (DOS) for H atomically chemisorbed on the (111) surface of Ni, Cu, Pt and Au [54]. Copyright 1995, Nature Publishing Group.

The  $d$ -band center theory has been more accurately interpreted and applied to a broader range of transition metal catalyst systems [56]. In addition, it was found that the position of the  $d$ -band center depends not only on the number of occupied  $d$ -orbitals but also their shape, affected by the coordination number, crystal plane and lattice spacing of transition metal based catalysts [57]. Up to now, this theory has been widely used to understand activity trends in metal-surface-catalyzed reactions. Some descriptors can be built based on it by use of DFT calculations and machine learning for predicting the activity trends of more complex systems [55, 58].

## 2.2 Reaction pathways

### 2.1.1 Oxygen reduction reaction and oxygen evolution reaction

The oxygen reduction reaction (ORR) reduces  $O_2$  into different oxygen-containing species, relying on the reaction pathways and the electrolytes used for carrying out this reaction. Generally, the ORR occurs *via* two routes [59]:

- (1) A  $4e^-$  reaction pathway: an oxygen molecule directly gets four electrons to form two water molecules in acidic media or to form hydroxide ions ( $OH^-$ ) in alkaline media.

(2) A [2+2] e<sup>-</sup> reaction pathway: an oxygen molecule gets four electrons *via* two successive two-electron steps, accompanying with the generation of a reactive intermediate (e.g., peroxides) and finally to form OH<sup>-</sup> ions or water.

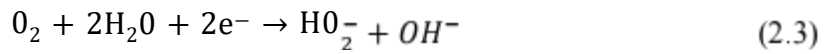
The ORR steps in alkaline and acidic electrolytes are listed as follows:

In alkaline media:

A 4e<sup>-</sup> reaction pathway:



A [2+2] e<sup>-</sup> reaction pathway:

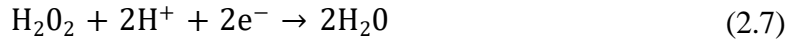


In acidic media:

A 4e<sup>-</sup> reaction pathway:



A [2+2] e<sup>-</sup> reaction pathway:

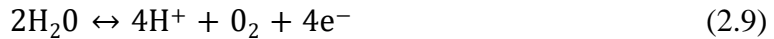


Different from the ORR, molecular oxygen is produced in the oxygen evolution reaction (OER) *via* several proton and electron coupled procedures [60]. The reaction is also highly pH dependent. The OER in alkaline and acidic electrolytes are listed as follows:

In alkaline media:



In acidic media:



The OER electrocatalysis in alkaline solutions is more favorable but difficult in neutral electrolytes. It reaches at very low performance in acidic solutions [61].

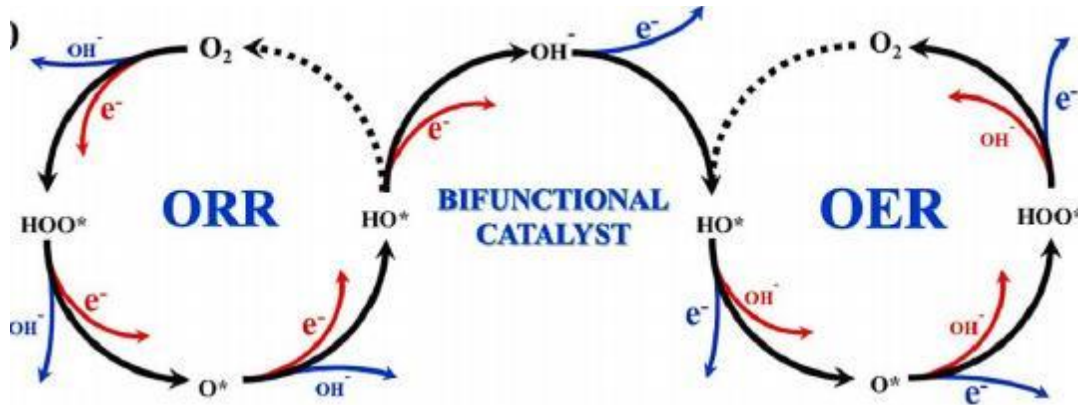
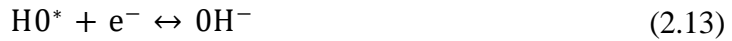
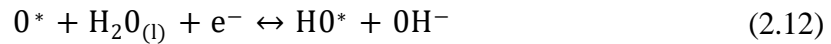
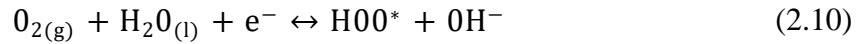


**Figure 2.7.** Proposed ORR (left) and OER (right) mechanism on a solid catalyst [62].

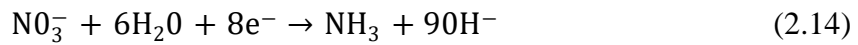
Copyright 2020, Elsevier B.V.

The reaction pathways of ORR and OER in alkaline solution can be divided into four basic steps (**Figure 2.7**). The formulations are listed below:



### 2.1.2 Nitrate reduction reaction

The total nitrate reduction reaction (NITRR) follows an eight-electron process in aneutral electrolyte:



The relationship between the standard equilibrium potentials of the nitrate reduction to  $\text{N}_2$  or ammonia and the pH value of an electrolyte is shown in the Pourbaix diagram of the  $\text{N}_2\text{-H}_2\text{O}$  system (**Figure 2.8**). Under standard conditions,  $\text{N}_2$  and  $\text{NH}_3/\text{NH}_4^+$  are the most thermodynamically stable forms of nitrogen. Additionally, the pH value of an electrolyte directly determines the existing form of ammonia. Moreover, although  $\text{N}_2$  is expected to be the preferred final product, several factors (e.g., electrode materials and electrochemical configurations) can alter the end products of electrocatalytic NITRR.

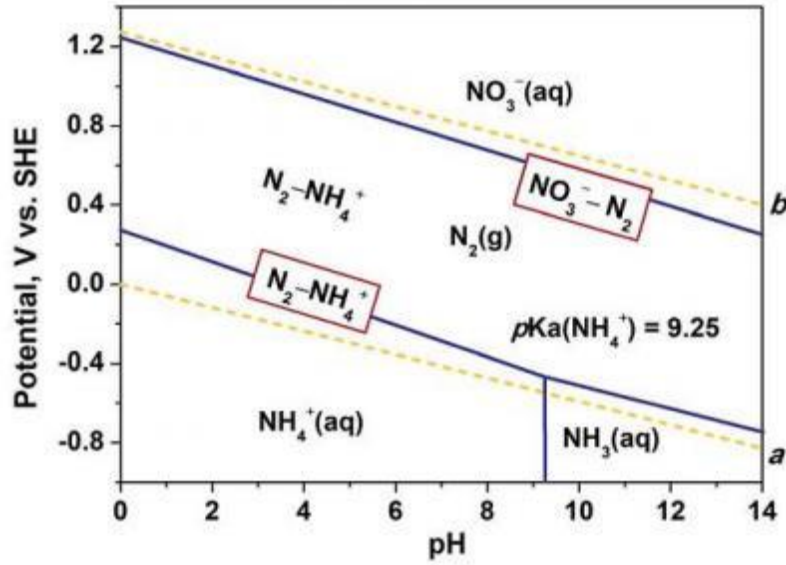
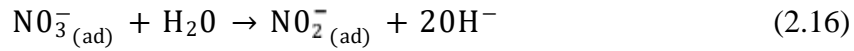
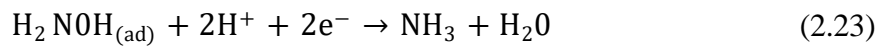
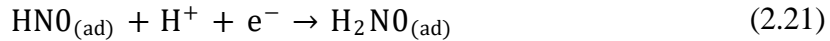
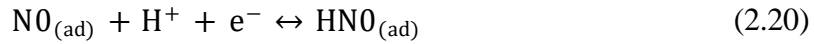
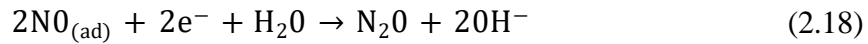
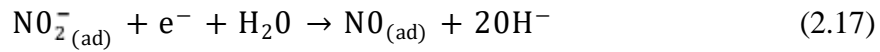


**Figure 2.8.** Pourbaix diagram for the  $N_2$ - $H_2O$  system [15]. Copyright 2022, The Royal Society of Chemistry.



The formation of  $NO_2^-(ad)$  is the rate-determining step in terms of the Tafel slope data ( $120 \text{ mV dec}^{-1}$ ). Therefore, after the nitrate adsorption step where adsorbed nitrite is generated, there are two main methods for nitrite reduction with two different electrocatalytic species.



Additionally, a certain amount of hydroxylamine ( $NH_2OH$ ) can be accumulated, due to the fast reduction rate of  $NO$  to  $NH_3$  during electrocatalytic NITRR at a larger

scale. Another reaction pathway of the NO electrocatalytic NITRR mechanism on transition metal catalysts is as follows:  $\text{NO}^* \rightarrow \text{N}^* \rightarrow \text{NH}^* \rightarrow \text{NH}_2^* \rightarrow \text{NH}_3^* \rightarrow \text{NH}_4^+$ .

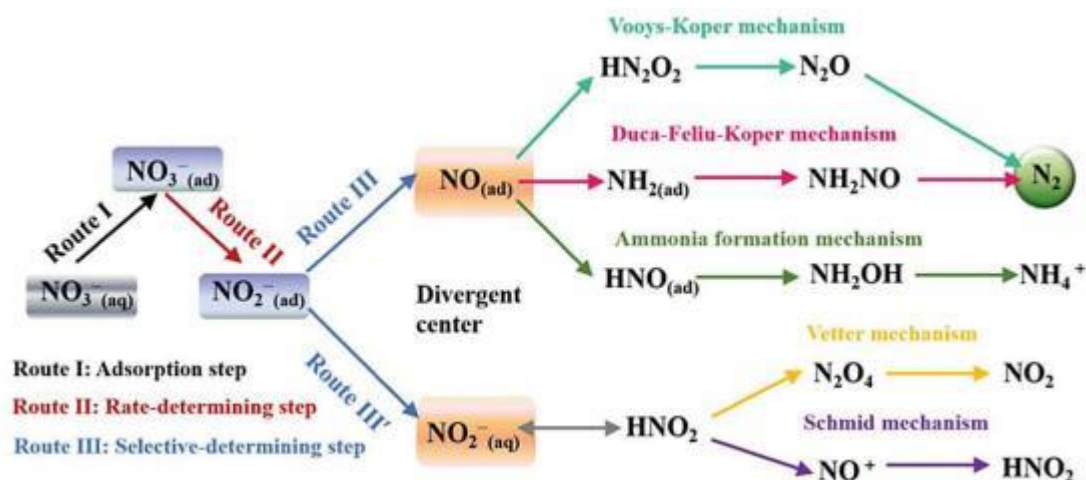


**Figure 2.9.** Proposed NITRR mechanism on a solid catalyst [15]. Copyright 2022, The Royal Society of Chemistry.

### 2.3 Density functional theory calculations

Density-functional theory (DFT) is a computational quantum mechanical modeling method that has been frequently used in physics, chemistry, and materials science to study the electronic structure of many-body systems. By using this theory, the properties of a many-electron system can be determined as a functional of the spatially dependent electron density. The DFT calculation is among the most popular and versatile methods in condensed-matter physics, computational physics and computational chemistry.

Since the 1970s, the DFT has been applied for the calculations in solid-state physics. Nevertheless, it was not considered accurate enough for the calculations in quantum chemistry until the 1990s, when the approximations used in this theory were greatly refined to better model the exchange and correlation interactions. Despite such improvements, there are still difficulties in using the DFT to precisely describe:

- i) intermolecular interactions (of critical importance to understand chemical



reactions), especially *van der* Waals forces (dispersion).

- ii) charge transfer excitations.
- iii) transition states, global potential energy surfaces, dopant interactions and some strongly correlated systems.
- iv) in the calculations of the band gap structures and ferromagnetism in semiconductors.

New DFT methods thus need to be designed to overcome these problems, for example by alterations to the functional [63] or by the inclusion of additive terms [64-68]. However, it is still controversial if the new DFT methods can hold in all conditions. This is because the DFT potentials obtained with adjustable parameters are no longer the true DFT potentials [69, 70].

### 2.3.1 The time-independent Schrödinger equation

In quantum mechanics, if the relativistic effects and time evolution are ignored, the time-independent Schrödinger equation can be presented as follows:

$$H\Psi(\vec{r}, \vec{R}) = E\Psi(\vec{r}, \vec{R}) \quad (2.24)$$

where  $\Psi(\vec{r}, \vec{R})$  is the wave functions,  $E$  is the energy of the system.  $H$  is the Hamiltonian operator, it can be described as:

$$H = H_e + H_n + H_{e-n} = (T_e + V_e) + (T_n + V_n) + V_{e-n} \quad (2.25)$$

$$T_e = - \sum_i \frac{\hbar^2}{2m_e} \nabla_i^2 \quad (2.26)$$

$$V_e = \frac{1}{24\pi\epsilon_0} \sum_{i \neq j} \frac{e^2}{|\vec{r}_i - \vec{r}_j|} \quad (2.27)$$

$$T_n = - \sum_I \frac{\hbar^2}{2M_I} \nabla_I^2 \quad (2.28)$$

$$V_n = \frac{1}{24\pi\epsilon_0} \sum_{I \neq J} \frac{Z_I Z_J e^2}{|\vec{R}_I - \vec{R}_J|} \quad (2.29)$$

$$V_{e-n} = - \frac{1}{4\pi\epsilon_0} \sum_{i,I} \frac{Z_I e^2}{|\vec{r}_i - \vec{R}_I|} \quad (2.30)$$

where  $\vec{r}_i$  and  $\vec{R}_I$  are the position coordinates of electrons and nuclei, respectively;

$m_e$  and  $M_I$  are the mass of electrons and nuclei in the system, respectively. The term of  $T_e$  is the kinetic energy and  $V_e$  is the potential energy of the electrons, while  $T_n$  is the kinetic energy and  $V_n$  is the potential energy of the nuclei. The term of  $V_{e-n}$  is the potential energy for the interaction between electrons and nuclei in the system. Once the wavefunction in the Schrödinger equation is solved, all the physical properties of this multi-particle system are then known. However, there are too many atoms in the solid materials for a direct solution of the Schrödinger equation. Some theoretical approximations must be employed.

### 2.3.2 Hartree-Fock method

In 1927, D. R. Hartree introduced a procedure, so-called by himself as a self-consistent field method, to calculate approximate wave functions and energies for atoms and ions [71]. He attempted to discard empirical parameters and resolve the many-body time-independent Schrödinger equation from fundamental physical principles, i.e., *ab initio*. However, the Hartree method was not widely understood and applied at that time. In 1928, J. C. Slater and J. A. Gaunt proved that the Hartree method can be based on amore rigorous theory by simplifying the wavefunction of the multiple electron system to the multiplication of the wavefunction of individual single electrons. Nevertheless, the Hartree method is still unsuccessful because it does not respect the antisymmetric principle of the wave function.

Until the 1930s, V. A. Fock [72] proposed that the wave function of the system can be given by the Slater determinant as:

$$\Psi = \frac{1}{\sqrt{N!}} \begin{vmatrix} \psi_1(\vec{q}_1) & \psi_2(\vec{q}_1) & \cdots & \psi_N(\vec{q}_1) \\ \psi_1(\vec{q}_2) & \psi_2(\vec{q}_2) & \cdots & \psi_N(\vec{q}_2) \\ \vdots & \vdots & \ddots & \vdots \\ \psi_1(\vec{q}_N) & \psi_2(\vec{q}_N) & \cdots & \psi_N(\vec{q}_N) \end{vmatrix} \quad (2.31)$$

where the pre-determinant of the determinant coefficient is called the normalization factor,  $\psi_i(\vec{q}_i)$  denotes the wavefunction of the  $i$  singlet. The term of  $\vec{q}_i$  contains the bit vector and spin degrees of the freedom. Since the Hamiltonian operator of the system

does not contain spins, the wavefunction  $\psi_i(\vec{q}_i)$  for a single electron can be expressed

as the multiplication of the orbital wave function  $\psi_i(\vec{r})$  with the spin wave function  $x_i(\sigma)$ :

$$\psi_i(\vec{q}_i) = \psi_i(\vec{r})x_i(\sigma) \quad (2.32)$$

Herein, the wavefunction  $\psi_i(\vec{q}_i)$  for a single electron also satisfies the orthogonal normalization condition:

$$\int \psi_i^*(\vec{q}_i) \psi_j(\vec{q}_j) d\vec{q} = \delta_{ij} \quad (2.33)$$

In this case, the energy of the system can be described as:

$$\begin{aligned} E = & \sum_i \int \psi_i^*(\vec{r}) [-(\vec{r})] \psi_i(\vec{r}) d\vec{r} \\ & + \psi_i(\vec{r}) \vec{r} - \vec{r}' \psi_j(\vec{r}') d\vec{r} d\vec{r}' \\ & - \psi_i^*(\vec{r}) \psi_j^*(\vec{r}') \vec{r} - \vec{r}' \psi_j(\vec{r}) \psi_i(\vec{r}') d\vec{r} d\vec{r}' \end{aligned} \quad (2.34)$$

The Schrödinger equation of single electrons is then solved, same as the Hartree approximation. It can be given in the form of, i.e. the Hartree-Fock equation [73]:

$$[-(\vec{r})]\psi(\vec{r}) = \psi(\vec{r}) \quad (2.35)$$

Note that the Hartree-Fock approximation only takes into account the exchange of electrons except for the electron correlation effect, which limits its applications. The omission of electron correlation can lead to large deviations from experimental results in some cases. An alternative method to resolve this problem is density functional theory, which treats both exchange and correlation energies.

### 2.3.3 Density functional theory

The DFT has its roots in the Thomas-Fermi model for the electronic structure of materials. However, it was firstly put on a firm theoretical footing by Walter Kohn and Pierre Hohenberg [74]. The Hohenberg-Kohn theorems are assumed as follows:

Theorem 1: the external potential (and hence the total energy) is a unique function electron density.

Theorem 2: the function that delivers the ground-state energy of the system gives the lowest energy, only if the input density is the true ground-state density.

Based on the two theorems, the ground-state energy can be determined as:

$$E[n(\vec{r})] = F[n(\vec{r})] + \int V(\vec{r})n(\vec{r})d\vec{r} \quad (2.36)$$

For the multi-electron system,  $F[n(\vec{r})]$  can be described as:

$$F[n(\vec{r})] = T[n(\vec{r})] + n(\vec{r})n(\vec{r}')\vec{r} - \vec{r}'\vec{r}d\vec{r}' + E'_{xc}[n(\vec{r})] \quad (2.37)$$

The Hohenberg-Kohn theorem provides a theoretical demonstration of the possibility of using electron density as a basis for calculating ground state properties. However, three factors remain to be identified: i) the electron number density  $n(\vec{r})$ , ii) the kinetic energy generalization  $T[n(\vec{r})]$ , iii) the exchange-correlation generalization  $E'_{xc}[n(\vec{r})]$ .

In 1965, the first two factors were successfully solved by Kohn and Sham [75]. They assumed that the existence of a fictitious system of non-interacting particles generate the same electron number density  $n(\vec{r})$  as any given system of interacting particles. Hence,  $n(\vec{r})$  can be described as:



The kinetic energy of this fictitious system without interactions can be determined

as:

$$T[n(\vec{r})] = \sum_i \int \psi_i^*(\vec{r}) (-\nabla^2) \psi_i(\vec{r}) d\vec{r} \quad (2.39)$$

The solution of the Schrödinger equation reads as follows:

$$[-\nabla^2] \psi_i(\vec{r}) = \epsilon_i \psi_i(\vec{r}) \quad (2.40)$$





---

The equal 3.21 and 3.22 are the typical representation of the Kohn-Sham equations.

The only uncertain factor in the Kohn-Sham equation is the exchange-correlation generalization  $E'_{xc}[n(\vec{r})]$ , which no one knows its concrete equations.

In order to successfully solve the Schrödinger equation of a multi-particle system, approximations and simplification must be used in practical applications. The local density approximation (LDA) and the generalized gradient approximation (GGA) are

two effective and widely used approximation methods. The LDA is suitable for structural optimization, modulus of elasticity and electronic structure calculations for most materials. However, for the systems where the electron number density varies extremely in space, the GGA will provide a more accurate result. Two common GGA methods are PBE and PW91.

### 2.3.4 Pseudopotential

The pseudopotential is an attempt to replace the complicated effects of the motion of the core (i.e., non-valence) electrons of an atom and its nucleus with an effective potential. Hence, the core states are eliminated and the valence electrons are described by pseudo-wave functions with significantly fewer nodes. In this approach, only the chemically active valence electrons are dealt with explicitly, while the core electrons are ‘frozen’ and treated as rigid non-polarized ionic nuclei along with the nucleus. Compared with the all-electric method, the pseudopotential focuses only on the effects of the valence electrons, which can significantly reduce the computational cost. Currently, the main pseudopotentials that are employed in the DFT methods are: the norm-conserving pseudopotential (NCPP), the ultrasoft pseudopotential (USPP), and the projector augmented plane wave pseudopotential (PAW).

The NCPP is accurate to calculate valence electron charge distribution since it exhibits good portability in different chemical environments. However, it is not suitable for localized orbitals such as 2p and 3d. Compared to the NCPP, the USPP discards the mode conservation and has been widely used. This is due to its accuracy and efficiency. Nevertheless, the construction of a highly accurate and portable USPP requires a large section of parameters and extensive experimental testing, which limits the further development. The PAW combines the USPP with linearized augmented plane wave (LAPW). It is therefore related to the full electron wave function using the projector operator. It is very close to USPP in terms of computational efficiency and more strictly accurate than other pseudopotentials. Hence, the PAW is the most widely used

pseudopotential today.

### 3 Experimental

#### 3.1 Film deposition techniques

##### 3.1.1 Microwave plasma enhanced chemical vapor deposition

Microwave plasma chemical vapor deposition (MPCVD) is an advanced technique, where the reaction rate of precursors is increased by use of a microwave plasma. It can be used to prepare high quality films with large areas, high purity, and fine crystalline structures.

During the deposition, the microwaves are created by a microwave generator. A mixture of gas resource is then fed into the reactor and excited by the microwave to form a glow discharge. The dissociation of the reaction molecules produces a plasma that is then deposited on the substrate (**Figure 3.1**). In this thesis, a MPCVD technique in a 915 MHz reactor (Cyrannus, Iplas) was employed.

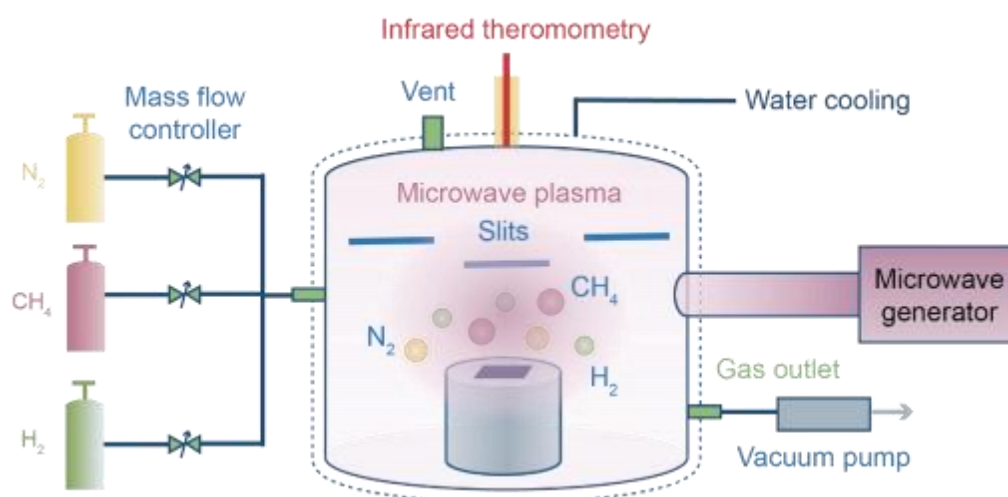


**Figure 3.1.** Illustration of the microwave plasma chemical vapor deposition (MPCVD) of diamond films.

##### 3.1.2 Hot filament chemical vapor deposition

Hot filament chemical vapor deposition (HFCVD) is a technique for the preparation of diamond films by pyrolysis of carbonaceous gases. The insoluble metal (e.g., tungsten, niobium and tantalum) wires are fixed in the upper part of a vacuum reaction chamber and heated to over 2000 °C. Then, the reaction gas sources are

decomposed into ions under a high temperature. The produced carbonaceous groups and atomic hydrogen contribute to the formation of  $sp^3C$  hybrid bonds, resulting in the deposition of a diamond film on the substrate (**Figure 3.2**).

The HFCVD technique is characterized by its simple equipment, easier control of the deposition conditions and a faster growth rate than other CVD methods. In this thesis, an HFCVD technique that was developed by our groups has been employed.

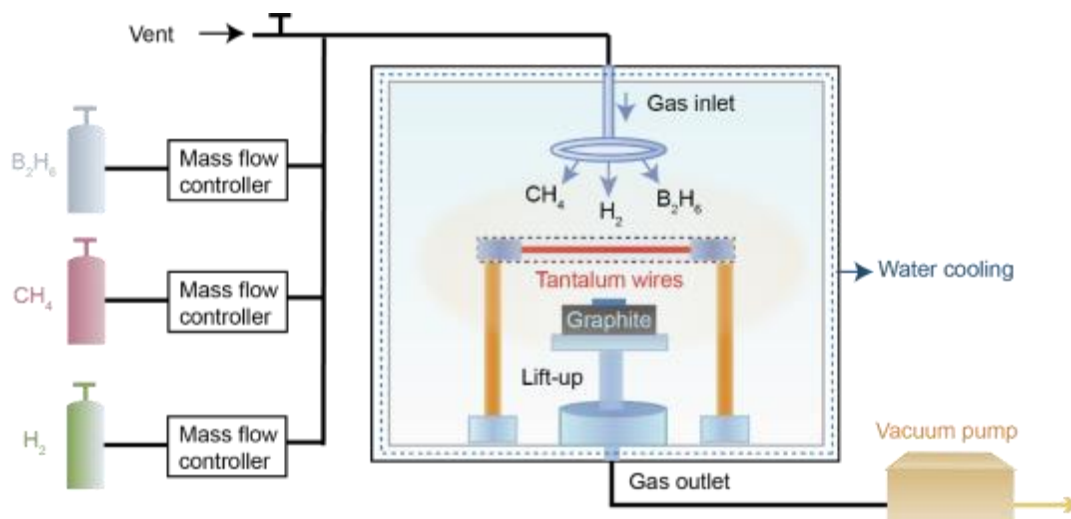


**Figure 3.2** Illustration of the hot filament chemical vapor deposition (HFCVD) of a diamond film.

### 3.1.3 Magnetron sputtering

Magnetron sputtering is a type of physical vapor deposition (PVD) technique. By introducing a magnetic field to the surface of a cathode target to increase the sputtering rate. This method can be used to prepare metals, semiconductors, insulators and many other materials. It has the advantages of simple equipment, easy control, large coating area, and strong adhesion with substrate.

During the deposition, the electrons collide with argon gas under an electric field to generate Ar ions, which are accelerated towards the cathode target and strike the target surface with a high energy, resulting in the sputtering. The sputtered neutral target atoms are deposited on the substrate, while the excited secondary electrons are subjected by electric and magnetic fields, travelling in a circular motion on the target

surface and ionizing a large number of Ar ions. Eventually, the energy of these electrons is depleted and the electrons fall onto the substrate (**Figure 3.3**). Hence, the magnetron sputtering technique is characterized by high deposition rates and low deposition temperatures.

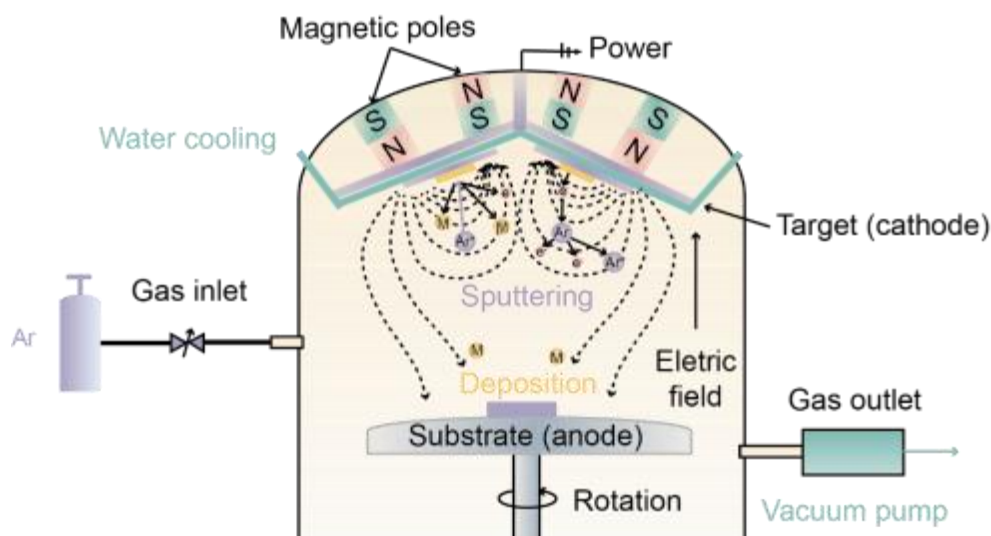


**Figure 3.3** Illustration of the magnet sputtering physical vapor deposition.

### 3.1.4 Electrodeposition

Electrodeposition is the process of electrochemical deposition of a metal or an alloy from an aqueous, non-aqueous solution or molten salt of its compound. These processes usually take place under certain electrolytes and operation conditions in the three-electrode systems (**Figure 3.4**). The process of electrodeposition and the morphology of the deposit are related to the nature of the deposited metal and also dependent on the composition of the electrolyte, pH value of the electrolyte, temperature, current density, and other factors.

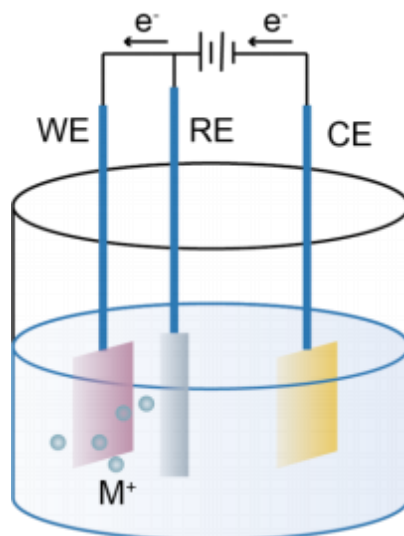


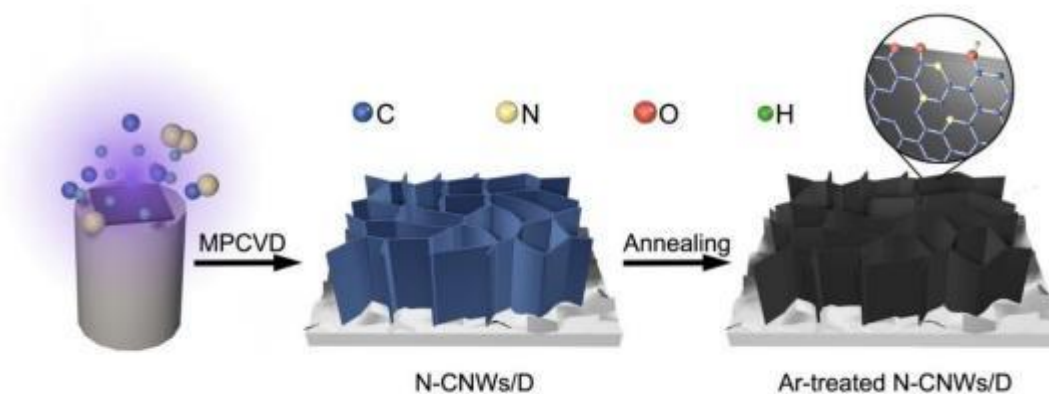
**Figure 3.4** Illustration of the electrodeposition in a three-electrode cell.

## 3.2 Preparation of diamond composites

### 3.2.1 N-CNWs/D composites

The synthetic procedure of the N-CNWs/D composites is illustrated in **Scheme 3.1**. The carbon nanowalls/diamond films (CNWs/D) were prepared on a conductive n-Si (100) wafer using the MPCVD technique in a 915 MHz reactor (Cyrannus, Iplas). Prior to the deposition, the silicon wafer was firstly ultrasonic cleaned in acetone, ethanol and pure water for 20, 10 and 5 min, respectively. Subsequently, it was ultrasonically seeded in the nanodiamond suspension for 30 min. These pretreated substrates were placed on an  $\text{Al}_2\text{O}_3$  holder with a height of 24 mm. The reaction chamber was evacuated to below  $5 \times 10^{-2}$  mbar. During the deposition process, the growth power was kept at 4 kW and the substrate temperature was held at around 875 °C. The deposition time was 60 min. To explore the growth process of the composites, the ratio of gas source flow rate  $\text{CH}_4/\text{H}_2$  was increased from 3% to 27%. The detailed growth parameters are listed in **Table 3.1**. For nitrogen doping of carbon nanowalls/diamond hybrid films (**N-CNWs/D**), pure  $\text{N}_2$  gas was introduced into the chamber with a flow rate varied from 6, 9 to 12 sccm. Other growth parameters remained identified. The as-prepared composites were named as **NCNWs/D-6**, **N-**

CNWs/D-9, and N-CNWs/D-12, respectively. The detailed growth parameters are listed in **Table 3.2**. The sample with 27% ratio named as **N-CNWs/D** was selected for the further studies.



**Scheme 3.1.** Illustration of the preparation of Ar-treated N-CNWs/D composites.

**Table 3.1.** Deposition parameters of CNWs/D composites with different  $CH_4/H_2$  ratios

Sample	$H_2$ (sccm)	$CH_4$ (sccm)	$N_2$ (sccm)	Power (kw)	Temperature (°C)	Time (min)
3% CNWs/D	100	3	0	4	~ 875	60
11% CNWs/D	100	11	0	4	~ 875	60
19% CNWs/D	100	19	0	4	~ 875	60
27% CNWs/D	100	27	0	4	~ 875	60

**Table 3.2.** Deposition parameters of CNWs/D and N-CNWs/D composites

Sample	$H_2$ (sccm)	$CH_4$ (sccm)	$N_2$ (sccm)	Power (kw)	Temperature (°C)	Time (min)
CNWs/D	100	27	0	4	~ 875	60
N-CNWs/D-6	100	27	6	4	~ 875	60
N-CNWs/D-9	100	27	9	4	~ 875	60
N-CNWs/D-12	100	27	12	4	~ 875	60



After that, the as-prepared N-CNWs/D-9 composite was annealed in a tube furnace at a temperature of 400, 500 and 600 °C for 1 h with a heating rate of 5 °C/min (**Figure 3.1**). The annealed samples were named as N-CNWs/D-9 Ar400 °C, N-CNWs/D-9 Ar500 °C and N-CNWs/D-9 Ar600 °C.

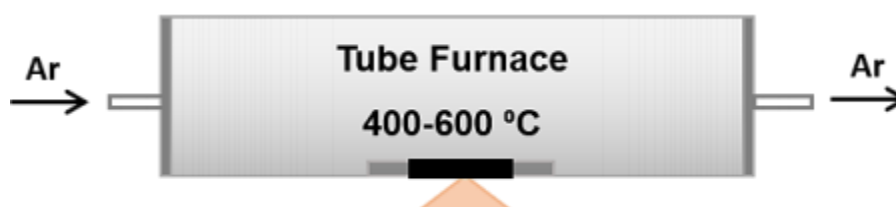
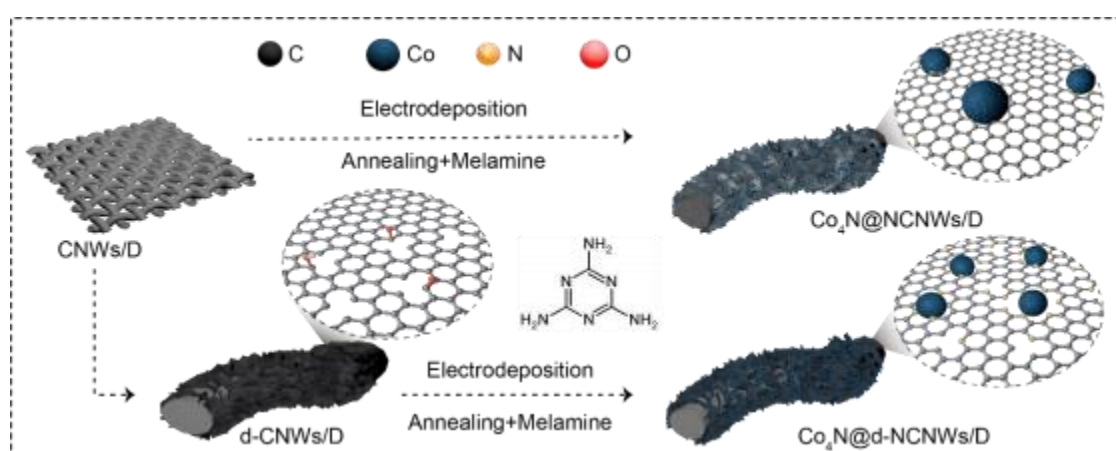


**Figure 3.5.** Illustration of the annealing treatment in a tube furnace.

### 3.2.2 Co<sub>4</sub>N@d-CNWs/D composites

The synthetic procedure of Co<sub>4</sub>N@d-CNWs/D composites is illustrated in **Scheme 3.2**. The detailed preparation process of each sample is as follows:



**Scheme 3.2.** Illustration of the preparation of Co<sub>4</sub>N@d-CNWs/D composites.

**CNWs/D films:** The carbon nanowall/diamond (CNWs/D) composites were prepared on carbon cloth (CC) using a MPCVD technique in a 915 MHz reactor (Cyrannus, Iplas). Prior to the deposition, the carbon cloth was ultrasonically cleaned in acetone, ethanol, pure water and nitric acid for 20, 10, 5, and 30 min, respectively. Such a clean process removed the pollutants and the oxidized layer from CC. It was

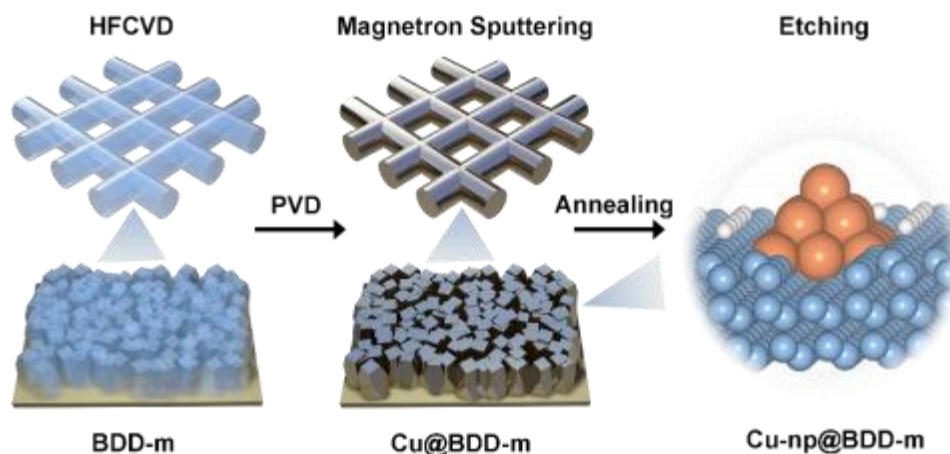
then seeded in a nanodiamond suspension for 30 min with aid of an ultrasonic bath. Detailed experimental parameters are same as those listed in **Table 3.1.1**. During the deposition process, the ratio of flow rate for  $\text{CH}_4/\text{H}_2$  was kept at 20:100 with a growth power of 4 kW and a substrate temperature of around 850 °C. After a deposition time of 60 min, the as-prepared composite was cooled down to the room temperature and restored in vacuum.

**$\text{Co}_4\text{N@NCNWs/D}$  composites:** The as-prepared CNWs/D composites were utilized as the working electrode and further coated with an electrodeposited compounds at room temperature. A three-electrode system was applied, consisting of a saturated calomel electrode (SCE) as the reference electrode and a platinum mesh as the counter electrode. The used aqueous electrolytic bath contained 0.001 M cobalt nitrate ( $\text{Co}(\text{NO}_3)_2 \cdot 6\text{H}_2\text{O}$ ). The  $\text{Co}(\text{OH})_2$  nanoplatelets were deposited within -1.0 to 0 V (vs. SCE) by means of cyclic voltammetry (CV) for 5 cycles at ascan rate of 20 mV/s. The obtained films were then annealed in a tube furnace, where 0.2 g melamine was added at 600 °C with a rate of 5 °C/min for 1 h under  $\text{Ar}/\text{H}_2$  atmosphere. The melamine was placed in a ceramic boat at upstream. The distance between samples and the melamine was kept approximately 10 cm (**Figure 3.2**). As a comparison, the Co films were synthesized directly on the CC *via* the same proto design. Their nitride treatment was conducted in a tube furnace.

**$\text{Co}_4\text{N@d-NCNWs/D}$  composites:** To controllably introduce defects, the as-prepared CNWs/D films were firstly pre-treated with an electrochemical oxidation process in an aqueous 1 M potassium nitrate ( $\text{KNO}_3$ ) at 1.6, 1.8, and 2.0 V (vs.  $\text{Hg}/\text{HgCl}$ ) for 20 min. These samples were named as d-CNw/D- 1.6V, d-CNw/D- 1.8V and d-CNw/D-2.0V composites, respectively. Notably, the d-CNWs/D- 1.8 composite was simply named as the **d-CNWs/D** film. The subsequent processes were applied, same as those applied previously as the  **$\text{Co}_4\text{N@NCNWs/D}$  films**. For the **d-NCNW/D** film, all other processes were the same with those for the  $\text{Co}_4\text{N@d-NCNW/D}$  film, except for the electrodeposition of  $\text{Co}(\text{OH})_2$  nanoplatelets.

### 3.2.3 Cu-np@BDD-m composites

As depicted in **Scheme 3.3**, the Cu-np@BDD-m composites were prepared by the following procedure:



**Scheme 3.3.** Illustration of the preparation of Cu-np@BDD-m composites.

**BDD-m films:** Initially, mesh BDD films were deposited on a copper mesh substrate *via* a hot filament chemical vapor deposition (HFCVD) technique. Prior to the deposition, the copper mesh was ultrasonicated in methanol and ethylene alcohol each for 30 min to remove the impurities from its surface. It was then ultrasonically seeded in the nanodiamond suspension for 30 min. The deposition process can be divided into two stages: carbonization of tantalum wires and diamond film deposition. During the carbonization, 12 tantalum wires with the diameter of 5 mm were employed. The flow rates of H<sub>2</sub> and CH<sub>4</sub> were kept at 400 and 10 sccm, respectively. The current maintained at 210 A for 90 min. After carbonization, the copper mesh was placed on a porous graphite plate to ensure double-sided deposition. During the film deposition, the flow rates of H<sub>2</sub> and CH<sub>4</sub> was kept at 300 and 3 sccm, respectively. While that of B<sub>2</sub>H<sub>6</sub> was varied from 0 to 30 sccm. The power remained above 7 kW and the temperature was kept around 870 °C. After a deposition time of 4 h, the as-prepared film was cooled down to the room temperature and restored in vacuum. For comparison, the **BDD films** were grown on the silicon wafers with the same growth conditions.

**Cu@BDD-m composites:** An ultrathin copper film was deposited on the as-prepared BDD and BDD-m films using a magnetron sputtering technique (DSC 200, Supro, Shenzhen). During the deposition, the Ar gas flow of Ar was continuously introduced at a flow rate of 40 sccm into the chamber to keep the pressure at 0.35 Pa. The power was 50 W and the deposition time was 10 s.

**Cu-np@BDD-m composites:** The Cu@BDD-m films were then annealed in a vacuum tube furnace to convert the ultrathin copper films into the copper nanoparticles. The flow rate of Ar/H<sub>2</sub> (H<sub>2</sub>:Ar = 5%) was 200 sccm and the pressure kept at 0.1 Pa. The annealing temperature was varied from 600 to 800 °C for 1 h with a heating rate of 5 °C/min. Finally, the Cu-np@BDD-m composites were obtained.

### 3.3 Characterization

#### 3.3.1 Morphology and physical structure characterization

##### Scanning electron microscopy (SEM)

The surface and cross-sectional morphology of the synthesized composites and films were characterized by a field emission scanning electron microscope (FE-SEM, Hitachi SU70, Japan) in IMR. The acceleration voltage of the electron gun was 5 to 20 kV. An integrated Oxford Instrument energy dispersive X-ray analysis (EDX) was conducted to quantitatively estimate element contents of as-synthesized films at an acceleration voltage of 10 kV.

##### Transmission electron microscope (TEM)

The microstructures of the synthesized films were depicted by a high-resolution transmission electron microscope (HRTEM, FEI, Tecnai G2 F20, USA) with an acceleration voltage of 200 kV in IMR. The Fast Fourier Transform (FFT), which was generated by stacking individual FFTs from the HRTEM images, was employed to analyze the crystallography of the synthesized films. The TEM samples were prepared as follows: The synthesized films were scraped off the substrate with a small blade and

dispersed in alcohol, followed by sonicating for 1 to 10 min. The mixed solution was then dropped onto the microgrid copper mesh with a pipette and dried for further observation.

### **Raman spectroscopy**

Raman spectroscopy is a non-destructive spectroscopic technique that has been commonly used to identify the vibrational modes of molecules. The information, such as the  $sp^2$  and  $sp^3$  phases in carbon-based materials, dopants, dangling bonds and “fingerprints” of transition metal compounds can be obtained from Raman spectroscopy. In this thesis, Raman measurements were performed on a Horiba LabRAM HR Evolution Spectrometer in IMR with a 532-nm laser to investigate the physical structures of diamond compounds by analyzing the positions and relative intensities of the peaks. The optical encoder is 1800 lines/mm with a magnification of 100 folds. To obtain accurate peak positions, the Raman spectrometer was calibrated to the characteristic peaks of single crystal Si at  $520.7\text{ cm}^{-1}$  before each test.

### **X-ray diffraction (XRD)**

The physical phase and crystallinity of synthesized composites and films were investigated using micro-XRD (Bruker, D8 Discover, USA) based on Co  $K\alpha 1$  radiation ( $\lambda=1.78897\text{ \AA}$ ) in IMR. The scan range was set from  $10^\circ$  to  $90^\circ$ . For pattern indexing, standard diffraction data banks (JCPDS 41-1487 for graphite and JCPDS 41-0943 for *fcc*  $\text{Co}_4\text{N}$  phase) were used.

#### **3.3.2 Surface states analysis**

##### **X-ray photoelectron spectroscopy (XPS)**

The surface chemical compositions and valence states of synthesized samples were analyzed by means of X-ray photoelectron spectroscopy (XPS, Thermal VG/ESCALAB250) in IMR. The theoretical basis of XPS is Einstein's law of

photoelectricity. With a beam of X-rays reaches samples, incident photons interact with samples and the energy is transferred from photons to electrons of the inner shell layer of atoms. These electrons get part of the energy to overcome the binding energy and the work function, and the rest of the energy releases as its kinetic energy, namely, these electrons become photoelectrons, this process is the photoelectric effect. Therefore, the binding energy will be calculated with measured kinetic energy of photoelectrons. For detailed parameters, an Al K $\alpha$  monochromatized radiation ( $h\nu = 1486.6$  eV) was employed as an X-ray source with the energy of 1486.6 eV. The radiation power is 150 W, input voltage is 15 kV, current is 10 mA. The diameter of the collection area is 500  $\mu\text{m}$ . To eliminate the influence of surface contamination, some signals were taken after a sputtering time of 10-30 s. For the sputtering, Ar ion guns with the voltage of 3 kV and the current of 2  $\mu\text{A}$  were employed. The sputtering area is  $2 \times 2$  mm<sup>2</sup>. The binding energies were calibrated using the sp<sup>2</sup>C signal at 284.5 eV as the reference.

For peak splitting, we used the XPSPEAK41 software. The peak positions were fixed (mentioned in the following article), and the data were fitted to match the original curves.

### Ultraviolet photoelectron spectroscopy (UPS)

The UPS measures kinetic energy spectra of photoelectrons, in order to determine molecular orbital energies in the valence region. In this thesis, a UPS setup (Thermal VG/ESCALAB250) was used to investigate the solid surfaces (to 10 nm depth) through the determination of related work function (WF) [76]. Briefly, the secondary edge position was measured and subtracted from the photon energy of the exciting radiation (HeI emission  $h\nu = 21.2$  eV). The difference is then the work function (**equal 3.1**) [77].

$$\text{WF} = h\nu - E_{\text{SE}} \quad (3.1)$$

The typical UPS spectrum of HDABiI<sub>5</sub>/FTO (**Figure 3.6**) shows the position of the secondary edge (e.g., the intersection of the dotted line and x-axis in the diagram). The value of the work function was calculated to be 3.7 eV vs. vacuum by use of the

**equal 3.1:**  $WF = (21.2 - 17.5) \text{ eV} = 3.7 \text{ eV}$ .

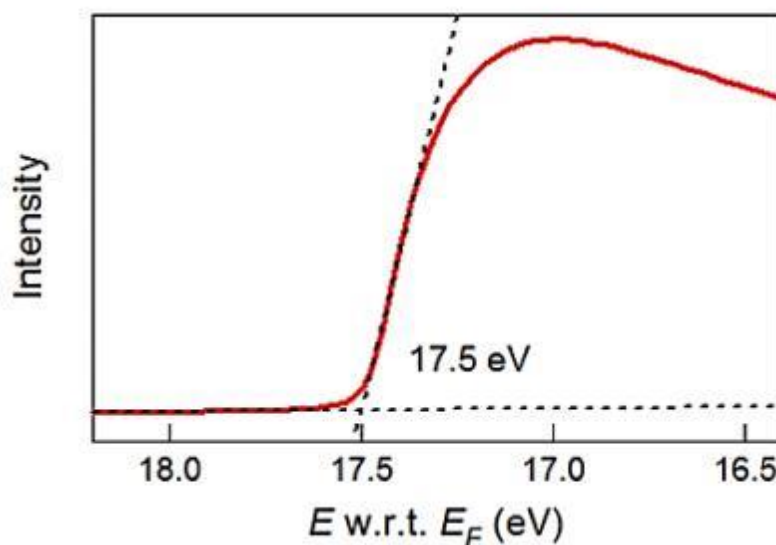


**Figure 3.6.** UPS spectra of HDABiI<sub>5</sub>/FTO for direct determination of the workfunction [78]. Copyright 2016, The Royal Society of Chemistry.

### Wettability

The wettability of the synthesized films is of vital importance to enhance and stabilize their electrocatalytic performance, since it determines the active area in contact with the electrolyte. Static water contact angles (SCA) were measured based on the sessile drop measuring method (Dataphysics QCA2015Pro) to characterize the wettability of the films. The volume of water drop was 2  $\mu\text{L}$ .

### 3.3.3 X-ray absorption spectroscopy (XAS)

The XAS is a microscopic technique to determine the local geometric and electronic structures of catalysts. A special feature of this kind of measurements is that it is usually carried out in synchrotron radiation facilities (**Figure 3.7**), which can provide intense and tunable X-ray beams. Therefore, it has an extremely sensitivity to detect the local microstructures compared to XRD and XPS. In this thesis, XAS was employed to investigate the coordination and bond lengths of metal elements in

transition compounds (e.g.,  $\text{Co}_4\text{N}$ ) and the covalent bond types of non-metallic elements (e.g., C, N).

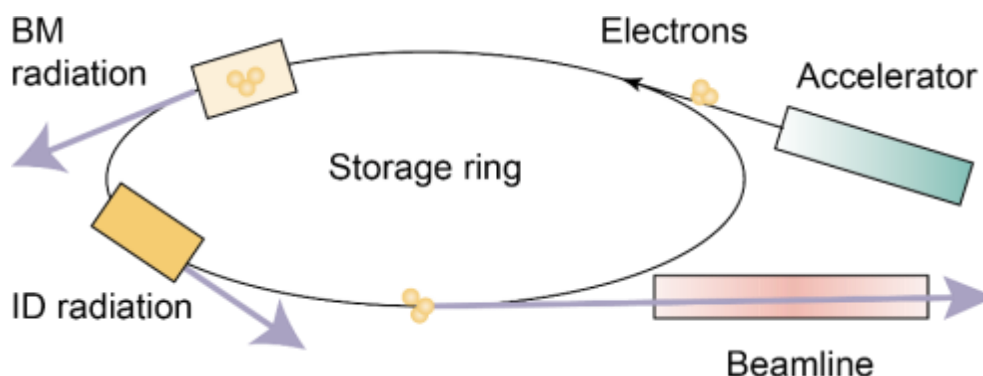


**Figure 3.7.** Synchrotron-radiation sources, X-ray optics and beamlines.

The XAS data were obtained by tuning the photon energy (via a crystalline monochromator) to a range where core electrons of the measured element were excited (0.1- 100 eV). During the scan, a sudden increase in x-ray adsorption occurs when the energy of the X-rays is just above the binding energy of the innermost electron shell of the atoms (1s orbital) interacting with the photons. This point is named as K-edge (**Figure 3.8**). Similarly, the other edges are determined when their core electrons are excited. For instance, an L-edge is obtained with the excitation of a 2s or 2p electron.

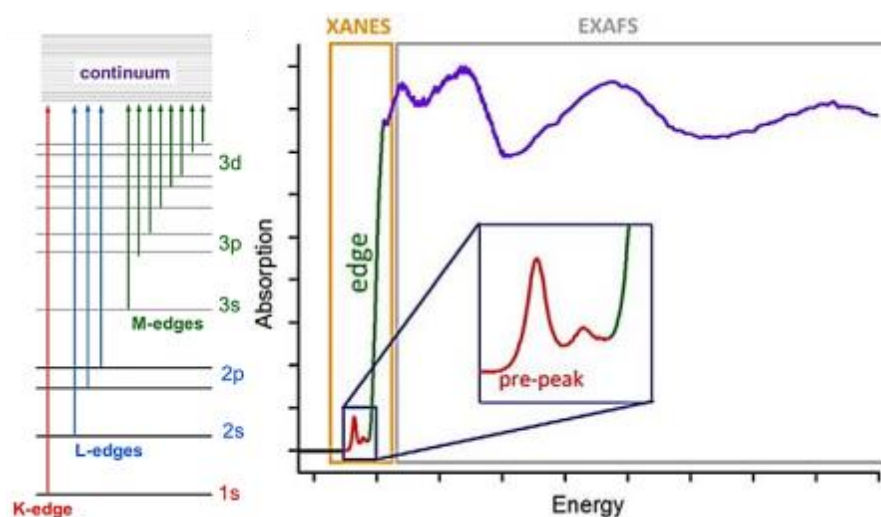


**Figure 3.8.** The K-, L-, and M-edges (left) and three regions of XAS data for the K-edge (right) [79]. Copyright 2014, Elsevier B.V.



The absorption data near the K-edge are most commonly collected. There are three main regions in the spectrum, which are considered as separated spectroscopic techniques (**Figure 3.8**). They are called adsorption threshold, X-ray absorption near-edge structure (XANES), and extended X-ray absorption fine structure (EXAFS), respectively. The XANES is dominated by core transitions to quasi bound states (multiple scattering resonances) for photoelectrons with a kinetic energy in the range from 10 to 150 eV above the chemical potential, while the EXAFS is dominated in the high energy range of the photoelectrons, where the scattering cross-section is weak with neighbor atoms. The XAS methodology can be broadly divided into four experimental categories that can give complementary results to each other: metal K-edge, metal L-edge, ligand K-edge, and EXAFS.

In this thesis, the Co K-edge analysis was performed with Si (111) crystal monochromators at the BL11B beamlines at the Shanghai Synchrotron Radiation Facility (SSRF) (Shanghai, China). The C, N K-edge signals were collected at the Singapore Synchrotron Light Source (SSLS) center. The data of metal K-edge of Co<sub>4</sub>N, ligand K-edge of C, N and EXAFS of Co<sub>4</sub>N were collected and analyzed by the software Athena and Artemis.

### 3.4 Electrochemical investigations

In this thesis, electrochemical methods such as rotating disk electrode (RDE), cyclic voltammetry (CV), linear sweep voltammetry (LSV), impedance spectroscopy (EIS), amperometry (or *i-t* curve), and Galvanostatic charge and discharge (GCD) method were employed to investigate electrochemical properties of synthesized composites and films as well as their electrocatalytic performance toward small molecules.

### 3.4.1 Electrochemical methods

#### Rotating disk electrode (RDE)

A rotating disk electrode (RDE) is a hydrodynamic working electrode that was used in a three-electrode system. The electrode rotates during experiments, inducing a constant flux of an analyte to the electrode (**Figure 3.9**). In this thesis, the working electrode (MSR Rotator, Pine, USA) was employed to evaluate performance of different catalysts toward oxygen reduction reaction.

The disk's rotation is usually described in term of angular velocity. As the disk turns around, some of the solution, which is named the hydrodynamic boundary layer, is dragged by the spinning disk and flange away from the center of the electrode, due to the generated centrifugal force. The main result is that a laminar flow of solution towards and across the electrode. This flow can quickly achieve conditions where the steady-state current is controlled by the solution flow rather than the diffusion. In contrast, the steady-state current in the cell and unstirred experiments such as CV is limited by the diffusion of species in solution. By conducting LSV or other experiments at various rotation rates, some electrochemical phenomena can be studied, such as multi-electron transfer, the kinetics of slow electron transfer processes and electrochemical reaction mechanisms.

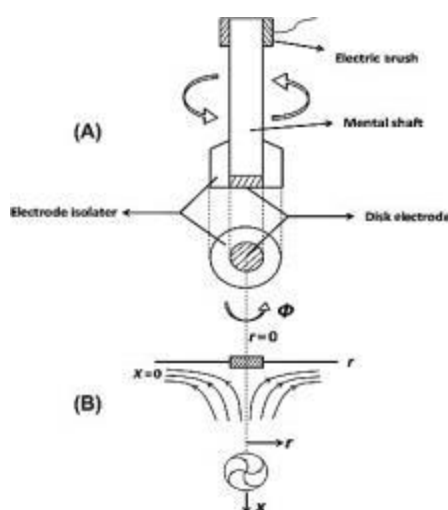


**Figure 3.9.** Illustration of rotating disk electrode method [80]. Copyright 2014, Elsevier B.V.

### **Cyclic voltammetry (CV) and linear sweep voltammetry (LSV)**

Cyclic voltammetry (CV) is a type of voltametric measurements. During the CV measurement, the potential on a working electrode is ramped linearly *vs.* time and then return to the initial potential in the opposite direction after the set potential is reached. These cycles of ramps in potential can be repeated as many times. In cycling phases, the variation rate of the potential is known as the scan rate (V/s). The potential is measured between the working electrode and the reference electrode, while the current is measured between the working electrode and the counter electrode. Hence, CV measurements provide information about redox potentials and electrochemical reaction rates. In addition, this method is also used to confirm whether the electrode surface reaches a static state.

Linear sweep voltammetry (LSV) is another voltametric method where the current at a working electrode is measured while the potential between the working electrode and a reference electrode is swept linearly as a function of time. The oxidation or reduction of species is recorded as a peak or trough in the current signal. Compared with CV, LSV is generally conducted at a lower scan rate (V/s) to ensure the static surface properties during the redox processes.

### **Electrochemical impedance spectroscopy (EIS)**

Electrochemical impedance spectroscopy (EIS) is a highly sensitive electrochemical technique to establish the electrical response of electrode systems. The EIS characterizes the time response of an electrode system using low amplitude alternating current (AC) voltages over a range of frequencies. Quantitative measurements are produced by the EIS and enable the evaluation of small-scale chemical mechanisms at the electrode interface and within the solution. In this thesis, EIS was used to investigate the reaction kinetics, charge transfer resistances, and double-layer capacitances of the synthesized catalysts.

### Amperometry (*ori-t* curve)

Amperometry (or *i-t* curve) records the current obtained at a constant potential as a function of time. It is commonly used in the long-term stability tests of catalytic reactions. In addition, it has also been applied to some constant voltage redox processes such as electrodeposition, electrooxidation and electrosynthesis.

### 3.4.2 Electrocatalytic oxygen reactions

For ORR/OER, the electrochemical tests were conducted by an Autolab workstation (PGSTAT302N) in a typical three-electrode system with an electrolyte of 0.1 M KOH solution at 25 °C. The three-compartment consisted of the synthesized film as the working electrode, a Hg/HgO (1 M KOH) as the reference electrode, and a Pt wire as the counter electrode. The potential was converted versus a reversible hydrogen electrode (RHE) using the following equation:

$$E_{\text{RHE}} = E_{\text{Hg/Hgo}} + 0.098 + 0.0591 \times \text{pH}. \quad (3.2)$$

The working electrodes were composed in the following different ways:

For N-CNWs/D films grown on the silicon substrate, the working electrode was a glassy carbon electrode (GCE, diameter of 5 mm). It was mounted on an RDE, coated with the synthesized films using nafion solution (5%). The Co<sub>4</sub>N@d-NCNWs/D films, which were grown on the CC, were directly used as the working electrodes. They were held by a PTFE clip. For comparison, commercial Pt/C (20 wt%) and RuO<sub>2</sub> working electrodes were prepared with a catalyst loading of 0.15 mg cm<sup>-2</sup> on the GCE or CC as areference.

Prior to OER/ORR measurements, the electrolytes were bubbled with oxygen or nitrogen for at least 30 minto ensure their saturation. The ORR and OER performance were studied by means of either CV at ascan rate of 50 mV s<sup>-1</sup> or LSV at ascan rate of 2 mV s<sup>-1</sup>. All potential data were adjusted with 95 % *iR*-correction. The presented current densities were normalized by the geometric surface areas of the used electrodes.

**Onset potential ( $E_{\text{onset}}$ ), Half-wave potential ( $E_{1/2}$ ), Overpotential ( $E_{10}$ ) and**

### Potential difference ( $\Delta E$ )

The onset potential ( $E_{\text{onset}}$ ) is the point where the current starts to raise from “zero” or a tangent can be drawn to obtain the onset potential (**Figure 3.10**). It presents the potential where all the thermodynamic and kinetic barriers become downhill. The value of  $E_{\text{onset}}$  is inherently sensitive to the surface catalyst loading and the specific surface area of a catalyst. It is thus a generally accepted parameter of electrocatalytic activity of a catalyst.

Half-wave potential ( $E_{1/2}$ ) is a potential at which polarographic wave current is equal to one-half of highest limiting current density ( $j_L$ ) in the ORR curve. The value of  $E_{1/2}$  indicates the capability (or mass activity [81]) of a catalyst.

An overpotential is a potential beyond a reversible potential that produces an increased thermodynamic driving force for the process. For the OER curve, the overpotential ( $E_{10}$ ) was determined as the potential where the current density reaches  $10 \text{ mA cm}^{-2}$ .

Potential difference ( $\Delta E$ ) is the difference between the  $E_{10}$  value of the OER and the  $E_{1/2}$  value of the ORR. It was used to evaluate the activity of abi-functional catalyst in this thesis.

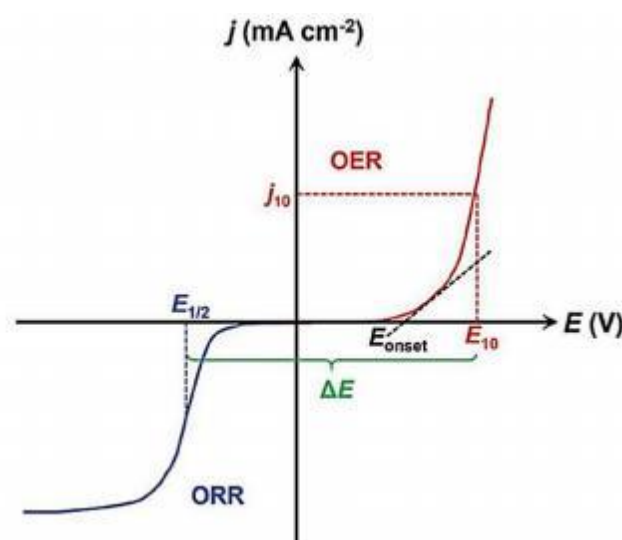


**Figure 3.10.** LSV curves of electrocatalytic ORR/OER [82]. Copyright 2017, Wiley-VCH.

### Electron transfer number

The number of transferred electrons was derived from the experimental data with aid of the Koutecky-Levich (K-L) equation:

$$\frac{1}{j} = \frac{1}{j_k} + \frac{1}{B\omega^{\frac{1}{2}}} \quad (3.3)$$

where  $\omega$  corresponds rotation speed recorded in the RDE test,  $j_k$  represents the kinetic current and can be regarded as a constant. The term  $B$  can be calculated by the following equation:

$$B = 0.2nF(D_0)^{\frac{2}{3}}\nu^{-\frac{1}{6}}C_0 \quad (3.4)$$

Here,  $n$  corresponds to the number of transferred electrons,  $F$  is the Faraday constant ( $= 96485 \text{ C mol}^{-1}$ ),  $D_0$  the diffusion coefficient of  $\text{O}_2$  ( $= 1.9 \times 10^{-5} \text{ cm}^2 \text{ s}^{-1}$ ),  $\nu$  the kinetic viscosity ( $= 0.01 \text{ cm}^2 \text{ s}^{-1}$ ), and  $C_0$  is the bulk concentration of  $\text{O}_2$  ( $= 1.2 \times 10^{-6} \text{ mol cm}^{-3}$ ). The constant 0.2 was employed when the rotation speed was presented in rpm.

### Electrochemical surface area (ECSA)

The electrochemical surface area (ECSA) of a catalyst was estimated by measuring the double-layer capacitance ( $C_{dl}$ ) from related CVs that were recorded at different scan rates (e.g., 4, 8, 12, 16, and 20  $\text{mV s}^{-1}$ ) under a potential range of 0.96 ~ 1.04 V (vs. RHE).

### Long-term stability and methanol resistance

The long-term stability and methanol resistance were examined by analyzing the current-time ( $i-t$ ) curves or chronoamperometric curves in  $\text{O}_2$ -saturated 0.1 M KOH. The potential was kept at a constant of 0.45 V (vs. RHE) when the rotation rate was maintained at 1600 rpm. During the methanol tolerance test, 5 mL methanol (3 M) was subsequently dropped in the electrolyte at 600 s. A graphite rod was employed as a counter electrode for eliminating the influence of Pt dissolution during the long-term

measurements.

### **Zinc-air battery tests**

To test the zinc-air battery (ZAB), the GCD curves were recorded with an electrochemical workstation (CHI 760E, Chenhua, Shanghai, China). The stability of ZABs was checked repeating charge/discharge cycles using galvanostatic pulses for 10 min of discharge, followed by 10 min of charge at a current density of  $1 \text{ mA cm}^{-2}$  (LANBT GRS-BT-2018R Model Battery Test System, GERISI New energy, Wuhan, China).

### **3.4.3 Electrocatalytic nitrate reduction reaction**

Electrochemical measurements of the NITRR were conducted by a CHI 760E electrochemical workstation (CHI760, Chenhua, Shanghai) in an H-type electrolytic cell which was separated by a Nafion membrane (**Figure 3.11**). The synthesized diamond composites, saturated calomel electrode (SCE), and platinum foil were used as the working electrode, reference electrode, and counter electrode, respectively. The geometric surface area of the working electrode was  $1 \text{ cm}^2$ . A  $0.5 \text{ M Na}_2\text{SO}_4$  solution (70 mL) was evenly distributed to both the cathode and anode cells.  $\text{NaNO}_3$  was pipetted into the cathode cell (containing  $10 \text{ mM NO}_3^-$ -N). All potentials were calibrated vs. the reversible hydrogen electrode (RHE). Before the NITRR test, LSV curves were recorded until that the polarization curves reached steady-state at a rate of  $2 \text{ mV s}^{-1}$  from  $0.5$  to  $-1.5 \text{ V vs. RHE}$ . Argon was introduced for at least 30 min to ensure the absence of oxygen. Then the potentiation tests ( $i$ - $t$  curve) were carried out at different potentials for 2 h with a stirring rate of 300 rpm.

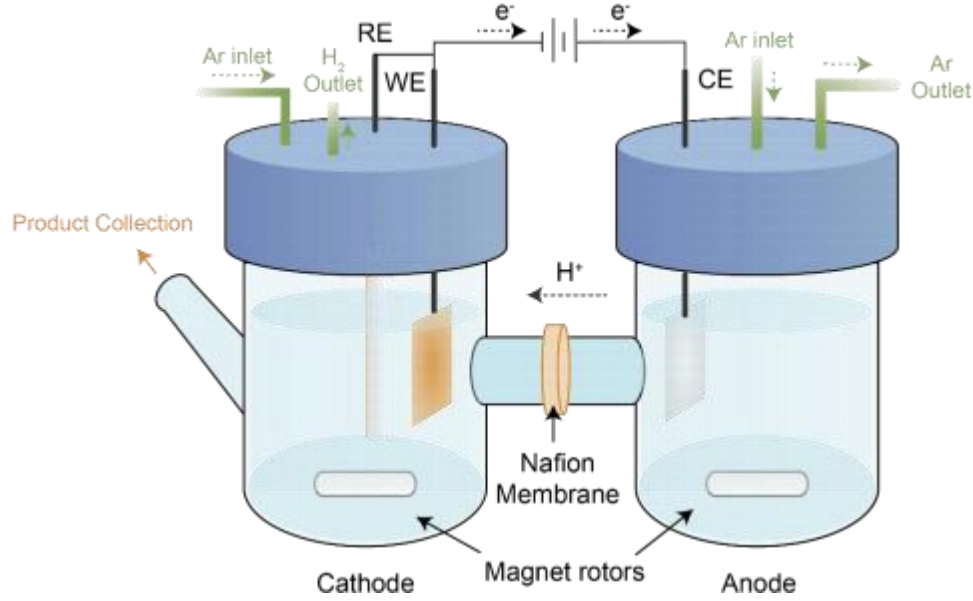


**Figure 3.11.** Schematic illustration of H-type cell for the NITRR.

**Calculation the nitrate conversion, selectivity, the yields of ammonia and Faradaic efficiencies**

For the NITRR, the nitrate conversion was calculated using:

$$\text{Conversion} = \frac{\Delta C_{\text{NO}_3^-}}{C_0} \times 100\% \quad (3.6)$$

The selectivity of ammonia and nitrite was determined by:

$$\text{Selectivity} = \frac{C}{\Delta C_{\text{NO}_3^-}} \times 100\% \quad (3.7)$$

The yield of ammonia was calculated by:

$$\text{yield}_{\text{NH}_3} = \frac{C_{\text{NH}_3} \times V}{M_{\text{NH}_3} \times t \times S} \quad (3.8)$$

The Faradaic efficiency was defined by:

$$\text{FE} = \frac{8F \times C_{\text{NH}_3} \times V}{M_{\text{NH}_3} \times Q} \quad (3.9)$$

where  $\Delta C_{\text{NO}_3^-}$  is the concentration difference of  $\text{NO}_3^-$  before and after the NITRR test,  $C_0$  is the initial concentration of  $\text{NO}_3^-$ ,  $c$  is the produced concentration of ammonia or nitrite.  $C_{\text{NH}_3}$  is the mass concentration of  $\text{NH}_3(\text{aq})$ ,  $V$  is the volume of the electrolyte in the cathode cell ( $= 70 \text{ mL}$ ),  $M_{\text{NH}_3}$  is the molar mass of  $\text{NH}_3$ ,  $t$  is the synthesis time ( $= 2 \text{ h}$ ),  $S$  is the geometric area of working electrode ( $= 1 \text{ cm}^2$ ).  $F$  is the Faradaic constant



(= 96485 C mol<sup>-1</sup>),  $Q$  is the total charge passing the electrode, which was calculated as the area integral of the  $i$ - $t$  curve.

### 3.5 Ion detection

The UV-Vis spectroscopy refers to adsorption spectroscopy or reflectance spectroscopy in part of the ultraviolet and the full, adjacent visible regions of the electromagnetic spectrum. Being relatively inexpensive and easily implemented, this methodology is widely applied in analytical chemistry for the quantitative determination of diverse analytes. In this thesis, the UV-Vis was employed for the quantitative analysis of reactant products and intermediates in the NITRR tests.

#### Determination of NO<sub>3</sub><sup>-</sup>N

After the NITRR, 0.1 mL of electrolyte was collected from the cathode cell and diluted to 5 mL to reach the detection range. The mixture of 0.1 mL 1 M HCl and 0.01 mL 0.8 wt% H<sub>3</sub>NSO<sub>3</sub> (sulfamic acid) solution were added into the diluted solution. The absorption spectrum was then recorded. The absorption intensities at a wavelength of 220 and 275 nm were collected to calculate the final absorbance value:  $A = A_{220} - 2A_{275}$  nm. The absorbance-concentration curve was calibrated using a series of standard sodium nitrate solutions (**Figure 3.12**).

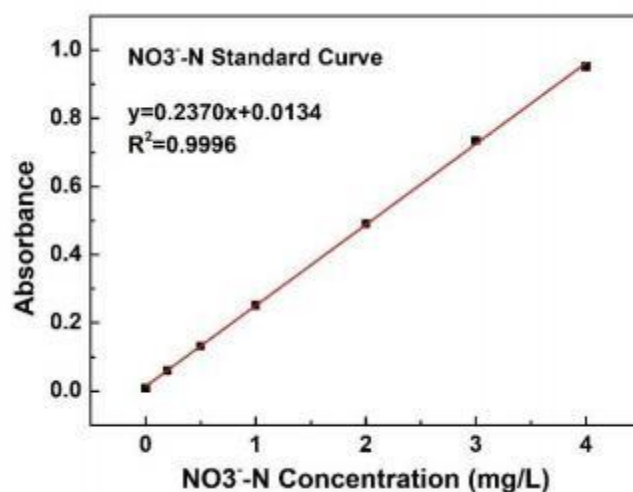


**Figure 3.12.** The absorbance-concentration calibration curves of NO<sub>3</sub><sup>-</sup>N.

### Determination of $\text{NO}_2^- \text{N}$

A color reagent was prepared by mixing 0.1 g of  $\text{C}_{12}\text{H}_{14}\text{N}_2$  (*N*-(1-naphthyl)ethyldiamine dihydrochloride), 1.0 g of  $\text{C}_6\text{H}_8\text{N}_2\text{O}_2\text{S}$  (sulfanilamide) and 2.94 L of  $\text{H}_3\text{PO}_4$  in 50 mL of deionized water. After the NITRR test, 0.5 mL of electrolyte was removed and diluted to 5 mL. Subsequently, 0.1 mL of color reagent was injected into the above-mentioned 5 mL solution. The absorption intensity at a wavelength of 540 nm was recorded after a reaction time of 30 min. The absorbance-concentration curve was calibrated using a series of standard sodium nitrite solutions (**Figure 3.13**).

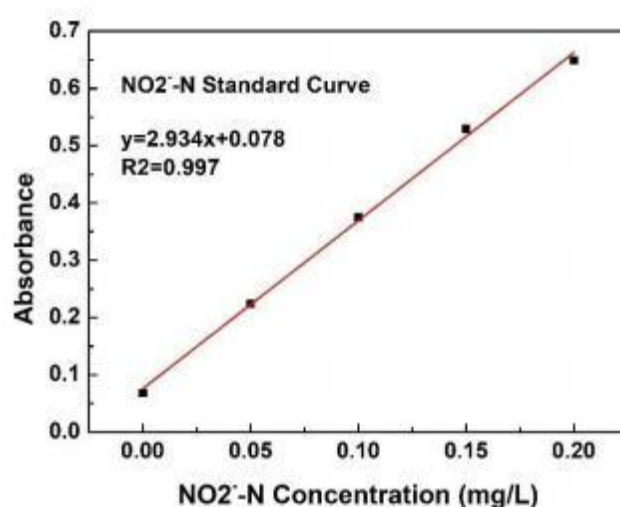


**Figure 3.13.** The absorbance-concentration calibration curves of  $\text{NO}_2^- \text{N}$ .

### Determination of $\text{NH}_3\text{-N}$

Ammonia was quantified by the indophenol blue method. The color reagent was prepared by diluting the 0.36 M  $\text{C}_7\text{H}_6\text{O}_3$  (salicylic acid), 0.36 M NaOH and 0.18 M  $\text{Na}_3\text{C}_6\text{H}_5\text{O}_7$  (sodium citrate). After the NITRR test, 1 mL of the electrolyte was mixed with 125  $\mu\text{L}$  of the coloring reagent, 12.5  $\mu\text{L}$  of 0.034 M SNP (sodium nitroprusside solution) and 12.5  $\mu\text{L}$  of NaClO (available chlorine 5.0 wt%). The mixture was reacted for 1 h to ensure a complete coloring reaction. The absorbance-concentration curve was calibrated using a series of standard ammonium chloride solutions (**Figure 3.14**).

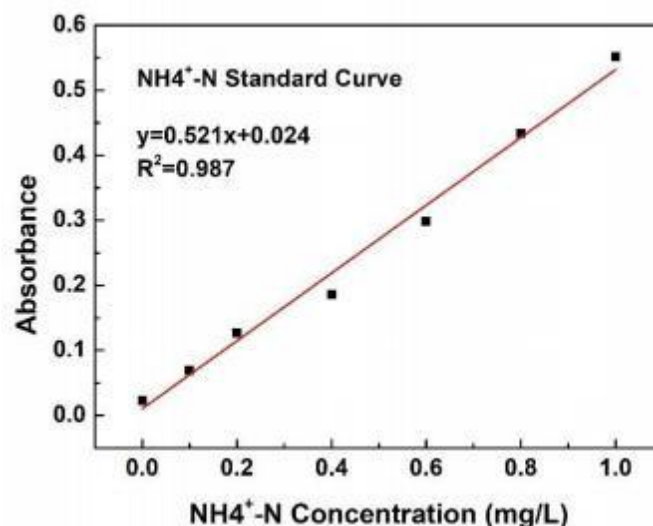


**Figure 3.14.** The absorbance-concentration calibration curves of  $\text{NH}_3\text{-N}$ .

### 3.6 Computer simulations

#### 3.6.1 Computer software

In this thesis, GGA-level spin-polarized DFT calculations were conducted with the plane-wave based Vienna *abinitio* simulation package (VASP 5.4.4) code. The PAW pseudopotentials were adopted to describe the ion-electron interactions. The Perdew-Burke-Ernzerhof exchange-correlation function was employed in the calculations of the exchange correlation energies.

3D-RISM-DFT calculations were carried out using the PWscf code as implemented in the Quantum ESPRESSO 7.1. The ultrasoft pseudopotential were used to represent the ionic cores and the Perdew-Burke-Ernzerhof exchange-correlation function was employed in the calculations of the exchange correlation energies. The atomic charge and ion-solvent interactions were described using the all-atom force field. Solvent interactions were described using a modified transferable five-point intermolecular potential (TIP5P) force field.

#### 3.6.2 Modelling details and parameters

To model the NCNW/D and d-NCNW/D surfaces, a supercell was used. It consisted of  $4\times 4$  graphene unit cells, where a N atom was replaced and a seven-layer

slab for the Co<sub>4</sub>N (111) was a vacuum region of 20 Å in the vertical direction. The lattice mismatch between the nitrogen-doped graphene and Co<sub>4</sub>N (111) is about 1.79 %. The maximum force on a single atom was smaller than 0.01 eV Å<sup>-1</sup>. The Brillouin zone was sampled by 3×3×1 *k* point mesh. The overpotentials ( $\eta$ ) at various sites were calculated by the standard hydrogen electrode method that was developed. The free energies of H<sub>2</sub> and H<sub>2</sub>O were calculated by placing them in a 10×10×10 cubic lattice.

As for Cu-np@BDD-m composites, a supercell C89B1Cu5 consisting of 10 layers of BDD (111) at the bottom and 5 Cu atoms at top. The size of supercell is  $a=7.57$  Å,  $b=6.55$  Å with a vacuum region of 30 Å in the vertical direction. As a comparison, two supercells, namely C89B1 represents the BDD-m composite and Cu36 relates to the Cu@BDD-m composite were established. The Brillouin zone was sampled by 3×3×1 *k* point mesh. The free energies of NO<sub>3</sub><sup>-</sup>, NH<sub>3</sub>, H<sub>2</sub> and H<sub>2</sub>O were calculated by placing them in a 10×10×10 cubic lattice.

With respect to 3D-RISM, the Cu-np@BDD-m composites was simulated at 300 K with the following salt solutions: 0.5 M Na<sub>2</sub>SO<sub>4</sub> and 10 mM NaNO<sub>3</sub>. The aqueous solutions were represented using the implicit solvation approach, providing a detailed statistical description of the simulated electrical double layer structure. The kinetic energy and charge density cutoffs were set at 36 and 360 Ry, respectively. The self-consistent electronic convergence limit was set to  $1 \times 10^{-5}$  eV.

## 4 N-CNWs/D composites for electrocatalytic ORR

Metal-free catalysts from various carbon nanomaterials (e.g., carbon nanotubes, graphene) have been widely studied in the past decades, due to their high abundance, low costs, and high conductivities [8, 83, 84]. It is well known that a pristine carbon material exhibits poor ORR activity. Many efforts have been thus made to disrupt the integrity of the carbon lattice for subsequent modifications. For instance, N-doping [59, 85-87] or co-doping of a carbon material with a second heteroatom (e.g., B, O, S, or P) [88-90] has led to the modulation of electronic properties and surface polarities of different carbon nanomaterials. To further adjust electronic structures and optimize the triple-phase reaction surface properties of these carbon nanomaterials, creation of topological defects, introduction of surface functional groups and edge-suspended bonds have been proposed as alternative ways. Using these carbon nanomaterials as the electrocatalysts, the ORR activity was much improved [31, 91]. Taking holey graphene as an example, it was generated by etching graphene with Ar plasma. As an ORR electrocatalyst, it exhibited high performance [92]. However, this powder-like and defect-rich graphene only featured conventional morphology and still suffered from partial blocking stemmed from the usage of polymer binder and aggregation during a long-term redox reaction. In these regards, this graphene electrocatalyst has limited active sites and unsatisfactory electrochemical stability. Different from conventional powder catalysts, carbon films with well-developed 3D nanostructures possess abundant accessible active sites, fast electron and mass transfer rates, good stability derived from the great mechanical adhesion between the catalyst layer and current collectors. Namely, they hold catalysts tightly on the surface without detaching [93, 94].

Carbon nanowalls (CNWs), one kind of vertically aligned multilayer graphene nanosheets, are known to be possible to be grown on a variety of substrates by use of CVD techniques in a vacuum chamber. If their accessible graphitic edges are combined with tunable valence band structures that are derived from dopants, improved O<sub>2</sub> adsorption and accelerated electron transfer are foreseen, eventually leading to

enhanced ORR selectivity and activity [95, 96]. For example, carbon nanowalls/diamond hybrid films have been proved to possess high electrochemical activity of edge-rich CNWs and mechanical stability, owing to the presence of a diamond nanoplatelet [97]. A further doping of such films with nitrogen, efficient and stable ORR electrocatalysts or catalytic electrodes are expected to be produced.

In this chapter, the synthesis and characterization nitrogen-doped carbon nanowalls/diamond (N-CNWs/D) composite nanostructures are summarized together with their ORR performance before and after their annealing post-treatment. The different roles of these two-steps were thoroughly analyzed, namely separately examining the reaction characteristics of nitrogen doping levels and Ar annealing post-treatment at different temperatures. The structure-performance relationship of the actual active sites in terms of the ORR pathway mechanism is also discussed. Such a binder-free carbon-based film electrode is expected to be promising for the ORR applications in energy devices.

#### 4.1 Modulation of N-CNWs/D composite nanostructures

The morphologies of the CNWs/D composites with the increased  $\text{CH}_4/\text{H}_2$  ratio from 3% to 27% were examined by FE-SEM. Note that only a thin nanodiamond (ND) layer was grown on the silicon substrate when the  $\text{CH}_4/\text{H}_2$  ratio was 3% (**Figure 4.1a, e**). As the  $\text{CH}_4$  flux rate was gradually increased, CNWs structures were grown out of the ND layers. As shown in **Figure 4.1b-d**, the lateral and vertical dimensions of CNWs are both enlarged with the increasing  $\text{CH}_4/\text{H}_2$  ratio. Meanwhile, the open channels are formed. The height of the CNWs rises up from 1.1 to 1.8  $\mu\text{m}$ , as measured in their cross-sectional images (**Figure 4.1f-h**). It is assumed that the high concentration of adsorbed methyl groups accelerates the growth rate of the CNWs.

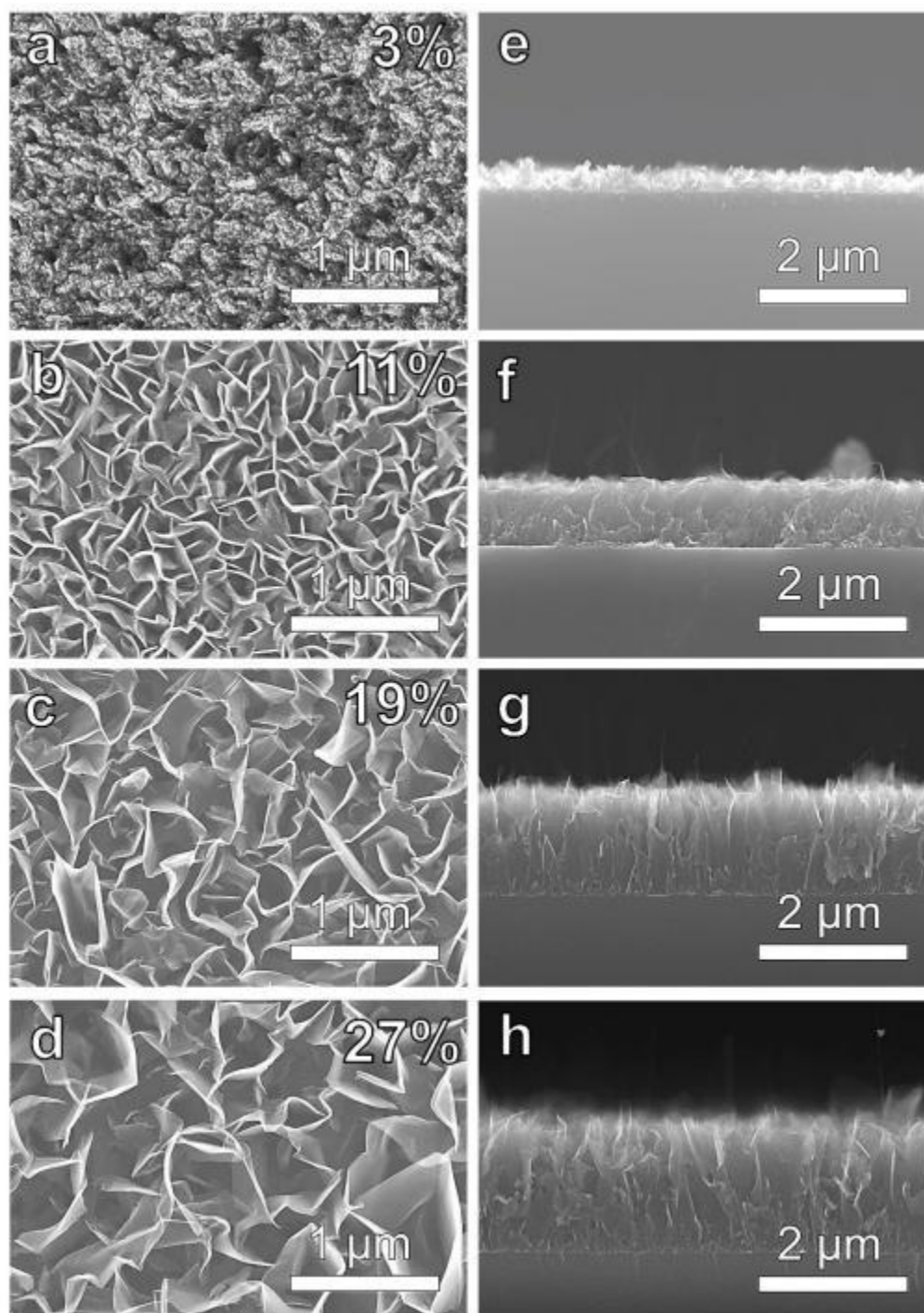


**Figure 4.1.** (a-d) Top view, (e-h) side view SEM images of CNW/D composites with various  $\text{CH}_4/\text{H}_2$  ratios from 3% to 27%.

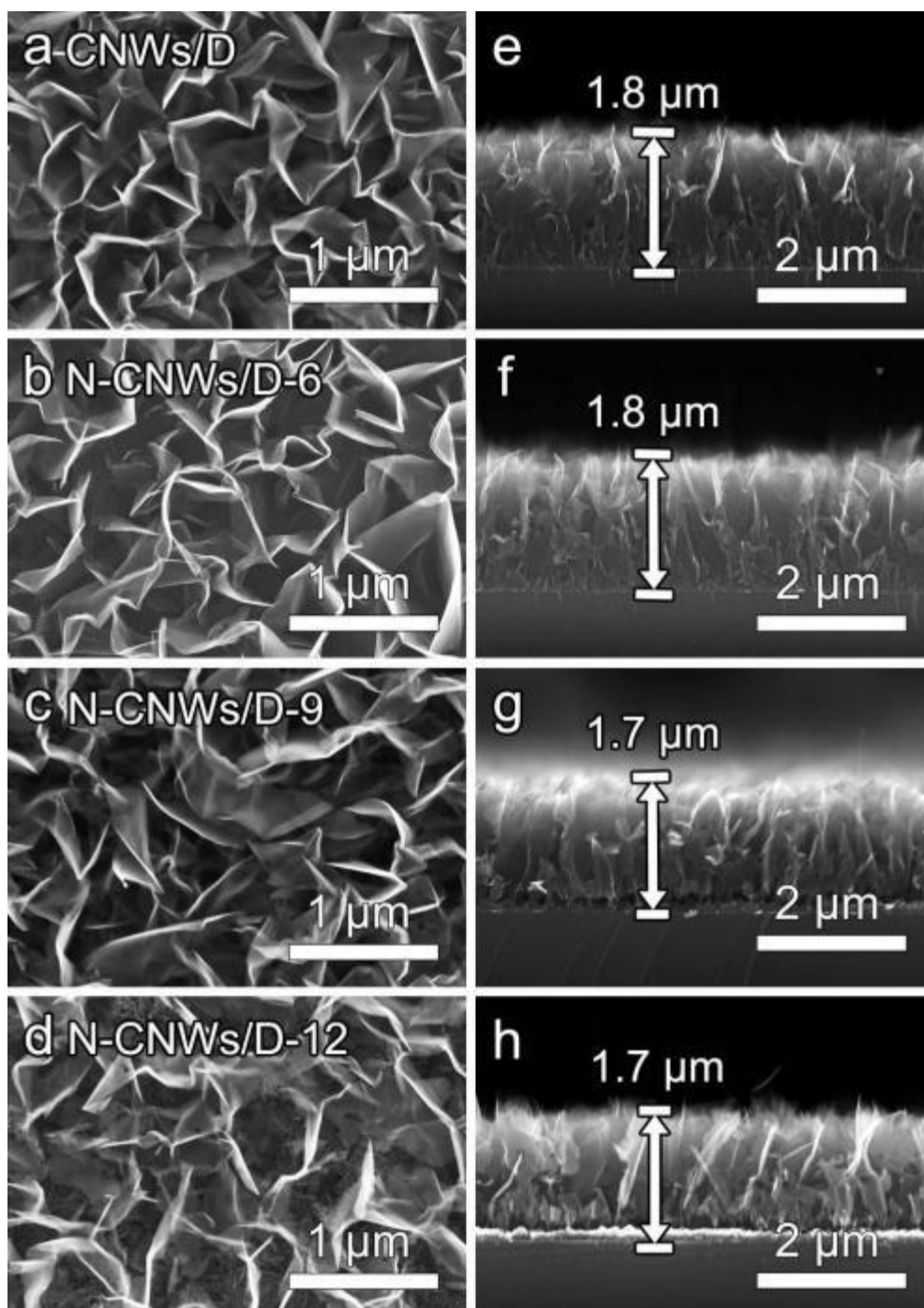


**Figure 4.2.** (a-d) Top view, (e-h) side view SEM images of CNWs/D, N-CNWs/D-6, N-CNWs/D-9 and N-CNWs/D-12 composites.

The deposition parameters with the  $\text{CH}_4/\text{H}_2$  ratio of 27% were chosen for further investigations. The morphologies of as-prepared CNWs/D and N-CNWs/D composites are depicted in **Figure 4.2**. An open structure with large and separated channels can be



seen on the as-prepared CNWs/D composites (**Figure 4.2a**). Meanwhile, such a film possesses abundant knife-like sharp edges in the growth layers. After the introduction of nitrogen dopants, the as-prepared N-CNWs/D-6, N-CNWs/D-9 and N-CNWs/D-12 composites exhibit more branching morphology, which is further varied with an increase of  $N_2$  flow rate (**Figure 4.2b, c, d**). When the nitrogen flux rises to 12 sccm, the structure of CNWs is partially damaged (**Figure 4.2d**). As confirmed in the cross-sectional images of these CNWs (**Figure 4.2e-h**), the height of all CNWs/D and N-CNWs/D composites is around 1.7 - 1.8  $\mu\text{m}$  under the same deposition times of 60 min. It's noteworthy that the thickness of the ND buffer layer between the Si substrate and vertical growth carbon sheets is varied as a function of the  $N_2$  flow rate applied in the doping process.

This ND layer is known to be formed during the scratching pretreatment using diamond powders. Its growth rate is promoted when the content of nitrogen dopants is increased, owing to the enhanced etching rate of amorphous-carbon (a-C) from  $N_2$  [98]. The CNWs are generated mainly from the boundary regions of the interisland in the ND layer and then vertically aligned by the crowding effects [99]. Hence, the configuration of the CNWs nanostructure is expected to be influenced by the growth process of a ND layer.

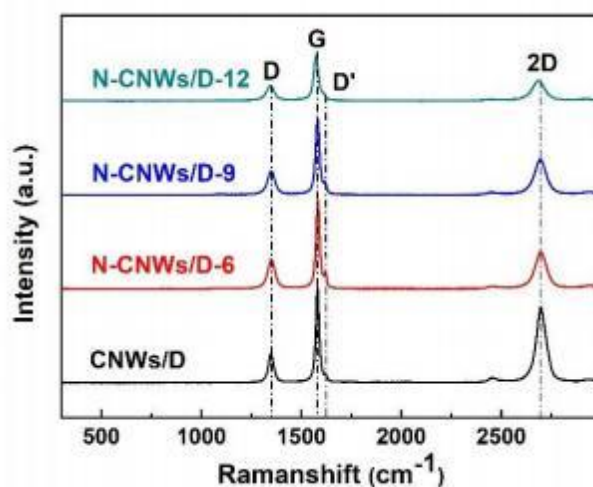


**Figure 4.3.** Raman spectra of CNWs/D, N-CNWs/D-6, N-CNWs/D-9 and N-CNWs/D-12 composites.

In the Raman spectra of these composites (**Figure 4.3**), four primary peaks appear at  $\sim 1345$ ,  $\sim 1580$ ,  $\sim 1621$  and  $\sim 2697$   $\text{cm}^{-1}$ . They correspond to the D band, G band, D' and 2D band of graphene, respectively [100]. Generally, the  $I_D/I_G$  intensity ratio is proportional to the number of defects in a carbon material. For these N-CNWs/D films, the  $I_D/I_G$  ratios are below 0.4 (**Table 4.1**). value is lower than that reported in the previous works [101], an indication of a high graphite crystallinity. The  $I_D/I_G$  value and the Full-width at half-maximum (FWHM) of these bands increase slightly with the nitrogen flow rate, revealing that the introduction of nitrogen leads to the generation of defects in the C atom lattice. In addition, it is obviously that the intensity of the 2D band decreases sharply in the N-CNWs/D composites, again manifesting that the introduction of nitrogen boosts the defect level of the CNWs/D composite. Moreover, the peak position of 2D band is shifted from  $2699$   $\text{cm}^{-1}$  for the CNWs/D to  $2695$ ,  $2691$  and  $2683$   $\text{cm}^{-1}$  for three N-CNWs/D composites, respectively (**Table 4.1**). Note that this red-shift of 2D band indicates a n-type doping state [102, 103]. Furthermore, all N-CNWs/D composites show outstanding D' bands, which correspond to abundant edge sites. Since these edge carbon atoms possess more active sites than the basal-plane ones, much faster electron transfer rate are expected to be provided for better electrocatalytic ORR performance [104].

**Table 4.1.** The FWHM of the D-, G-, 2D-band, positions of 2D-band and  $I_D/I_G$  ratios of CNWs/D and N-CNWs/D composites.

Sample	FWHM <sub>D</sub> ( $\text{cm}^{-1}$ )	FWHM <sub>G</sub> ( $\text{cm}^{-1}$ )	FWHM <sub>2D</sub> ( $\text{cm}^{-1}$ )	$\nu_{2D}$ ( $\text{cm}^{-1}$ )	$I_D/I_G$
CNWs/D	32.9	20.4	62.9	2699.1	0.321
N-CNWs/D-6	43.0	20.8	67.6	2695.5	0.333
N-CNWs/D-9	44.3	23.8	69.1	2691.2	0.335
N-CNWs/D-12	43.9	28.5	77.4	2683.3	0.360

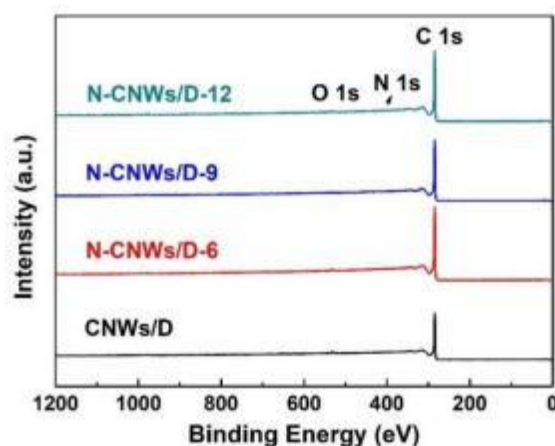


**Figure 4.4.** XPS spectra of CNWs/D, N-CNWs/D-6, N-CNWs/D-9 and N-CNWs/D-12 composites.

X-ray photoelectron spectroscopy (XPS) was utilized to analyze the compositions and chemical states of as-prepared CNWs/D and N-CNWs/D composites. In their survey spectra (**Figure 4.4**) C 1s, O 1s and N 1s are observed. The C1s peak in the survey spectra was further divided into five peaks. They are located at  $284.5 \pm 0.1$ ,  $285.2 \pm 0.1$ ,  $285.8 \pm 0.1$ ,  $286.6 \pm 0.1$ , and  $289.3 \pm 0.1$  eV, attributed to aromatic  $sp^2$  bond carbon ( $sp^2$ ),  $sp^3$  bonded carbon ( $sp^3$ ), C-N, C-O, and shakeup  $\pi-\pi^*$  satellite, respectively (**Figure. 4.5a**) [105]. It can be observed that the ratio of  $sp^3$  carbon is increased in the N-CNWs/D composites, while the value of  $sp^2/sp^3$  is decreased from 5.6 to 4.1, 2.8 and 2.5 for the CNWs/D, N-CNWs/D-6, N-CNWs/D-9 and N-CNWs/D-12 composites, respectively (**Table 4.3**). This is probably because that incorporation of nitrogen atoms disrupts  $sp^2$  hybridization of carbon atoms, leading to more defects in the lattice. Such a statement is in accord with the Raman results of these composites. Meanwhile, the presence of aND layer can lead to an increase of  $sp^3$  carbon. Moreover, the C-N group peak is seen, verifying the incorporation of N element in the N-CNWs/D composites. In the high-resolution N 1s spectrum (**Figure. 4.5b**), the N1s peaks are split into three peaks at  $398.7 \pm 0.1$ ,  $400.2 \pm 0.1$ , and  $401.5 \pm 0.1$  eV. They correspond to pyridinic N, pyrrolic N, and graphitic N, respectively. Three types of N are distributed

uniformly on the surface of the as-prepared N-CNWs/D composites (**Table 4.4**). The contents of doped nitrogen for the N-CNWs/D-6, N-CNWs/D-9 and N-CNWs/D-12 composites are 1.4%, 1.5% and 1.2%, respectively (**Table 4.2**). The N-CNWs/D-9 composite possesses the highest nitrogen doping level. The lowest nitrogen doping level of the N-CNWs/D-12 composite is probably caused by the damage on the surface structure (**Figure 4.2d**). It is noteworthy that a trace amount of O has also been found, which might be owing to the physically adsorption of oxygen at ambient atmosphere.

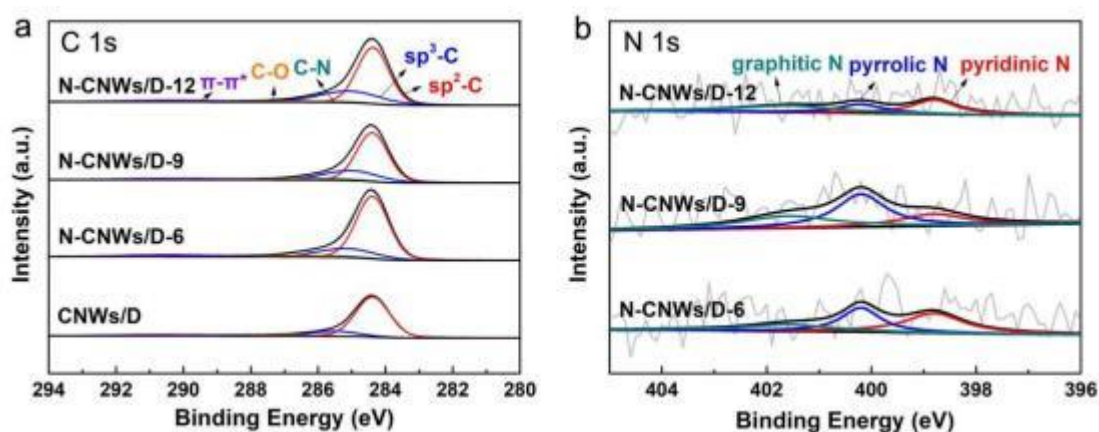


**Figure 4.5.** High-resolution XPS C 1s spectra (a) and N 1s spectra (b) of CNWs/D, N-CNWs/D-6, N-CNWs/D-9 and N-CNWs/D-12 composites.

**Table 4.2.** Deconvolution of relative compositions of XPS.

Sample	C (%)	O (%)	N (%)
CNWs/D	98.0	1.9	0
N-CNWs/D-6	96.4	1.5	1.4
N-CNWs/D-9	97.1	1.2	1.5
N-CNWs/D-12	97.5	1.3	1.2
N-CNWs/D-9 Ar600 °C	92.4	5.5	1.7

**Table 4.3.** Distribution of C species obtained from the de-convolution of the C 1s peaks by XPS.

Sample	sp <sup>3</sup> -C	sp <sup>2</sup> -C	sp <sup>2</sup> /sp <sup>3</sup>	C-N	C-O	$\pi$ - $\pi^*$
CNWs/D	13.8	76.7	5.6	-	3.1	5.9
N-CNWs/D-6	17.4	70.8	4.1	3.3	3.3	5.3
N-CNWs/D-9	23.5	66.7	2.8	3.6	1.9	4.3
N-CNWs/D-12	26.0	64.7	2.5	2.3	2.3	4.6

**Table 4.4.** Distribution of N species obtained from the de-convolution of the N 1s peaks by XPS.

Sample	pyridinic N	pyrrolic N	graphitic N
N-CNWs/D-6	30.0	52.6	17.3
N-CNWs/D-9	22.1	45.9	31.9
N-CNWs/D-12	37.9	23.4	38.6

## 4.2 ORR performance of N-CNWs/D composites

The LSV-RDE measurements were conducted to evaluate the ORR activity of the as-prepared CNWs/D and N-CNWs/D composites in O<sub>2</sub>-saturated 0.1 M KOH electrolyte, namely to explicate the role of nitrogen doping toward the ORR. From the LSV polarization curves of these films measured at a rotation rate of 1600 rpm (**Figure 4.6**), one can see that the ORR onset potential and diffusion limiting current density of the N-CNWs/D composites is improved with an increase of doped nitrogen content. The N-CNWs/D-9 composite exhibits the highest ORR activity in that its onset potential is 0.733 V (vs. RHE), much more positive than that (0.670 V) using the CNWs/D composite. Meanwhile, the highest diffusion limiting current density ( $j_L$ ) is

increased from  $0.42 \text{ mA cm}^{-2}$  to  $1.89 \text{ mA cm}^{-2}$ . These results suggest that the doping of nitrogen into N-CNWs/D composites can positively shift the onset potential and facilitate the reaction kinetics of ORR. As then-type doping changes the valence band structure of a carbon material (e.g., to increase the density of  $\pi$  states near the Fermi level), the  $\text{O}_2$  adsorption is thus enhanced, leading to improving the ORR performance [106]. The ORR activity of the N-CNWs/D composites is further found to be proportional to the nitrogen doping level, which is consistent with the XPS results. However, the ORR performance of the N-CNWs/D-9 composite is still very poor when compared to other nitrogen doped carbon-based catalysts [107]. Its further enhancement is still required.

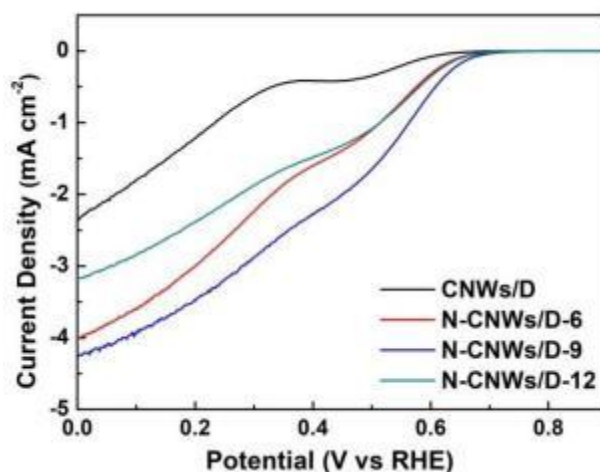


**Figure 4.6.** LSVs of CNWs/D, N-CNWs/D-6, N-CNWs/D-9 and N-CNWs/D-12 composites at a rotation speed of 1600 rpm in  $\text{O}_2$  saturated  $0.1 \text{ M KOH}$  at a scan rate of  $10 \text{ mV s}^{-1}$ .

### 4.3 Annealing treatment and enhancing ORR performance

In the SEM images of the N-CNWs/D-9 composites after Ar annealing treatment for 2 h at  $400^\circ\text{C}$  (Figure 4.7a),  $500^\circ\text{C}$  (Figure 4.7b),  $600^\circ\text{C}$  (Figure 4.7c), similar macroscopic surface morphologies are clearly seen. To reveal their defect levels, the Raman spectra of these N-CNWs/D-9 films were recorded (Figure 4.7d). The value of

$I_D/I_G$  is increased from 0.335 to 0.395 with an increase of the annealing temperature (Table 4.5). Moreover, the FWHMs of all bands are gradually enlarged, indicating that the annealing treatment leads to the generation of more defects on the N-CNWs/D-9 composite.

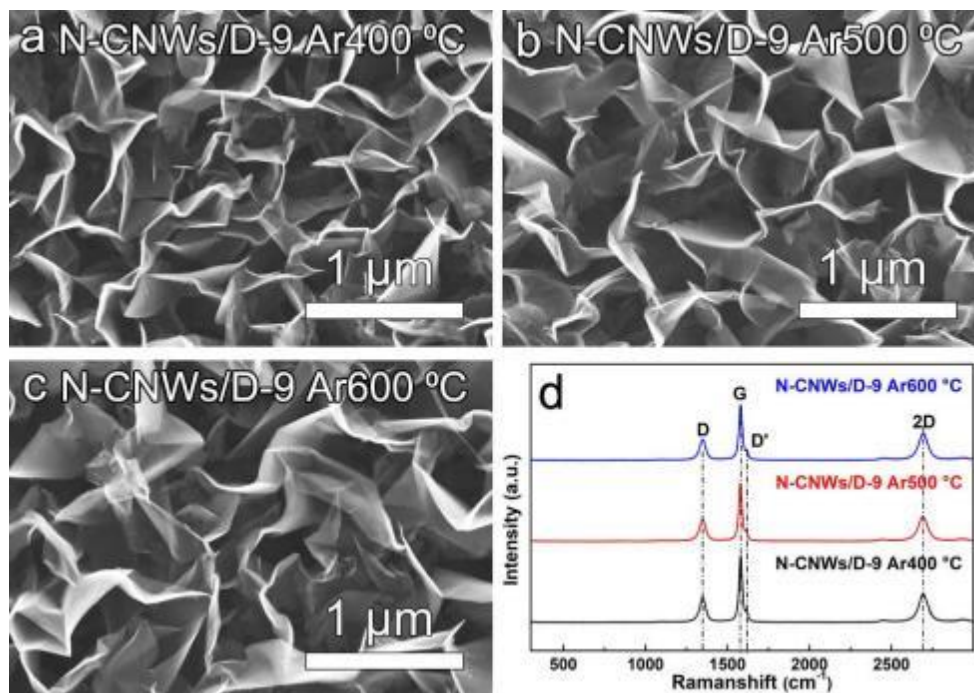


**Figure 4.7.** SEM images of the N-CNWs/D-9 composites after Ar annealing treatment at (a) 400 °C, (b) 500 °C, and (c) 600 °C as well as corresponding Raman spectra.

**Table 4.5.** The FWHM of the D-, G- and 2D-band and  $I_D/I_G$  ratio of N-CNWs/D-9 composites after Ar annealing treatment at 400 °C, 500 °C and 600 °C.

Sample	FWHM <sub>D</sub> (cm <sup>-1</sup> )	FWHM <sub>G</sub> (cm <sup>-1</sup> )	FWHM <sub>2D</sub> (cm <sup>-1</sup> )	$I_D/I_G$
N-CNWs/D-9 Ar400 °C	40.39	24.21	61.92	0.385
N-CNWs/D-9 Ar500 °C	44.35	24.25	66.25	0.388
N-CNWs/D-9 Ar600 °C	46.98	25.9	65.77	0.395

The ORR electrocatalytic activities of the N-CNWs/D-9 composites after Ar



annealing treatment at different temperatures were evaluated. As a comparison, a commercial Pt/C powder was utilized and measured under the identified conditions. In the cyclic voltammograms (CVs) recorded in  $N_2$ - and  $O_2$ -saturated 0.1 M KOH (**Figure 4.8a**), one can see that obvious reduction peaks appear in the  $O_2$ -saturated electrolyte for all N-CNWs/D-9 composites, while these peaks are absent in  $N_2$ -saturated one. Compared with the as-prepared N-CNWs/D-9 composite, the Ar-treated N-CNWs/D-9 composites exhibit higher peak currents with a gradually positive shift of the reduction peak potential, indicating their remarkable enhancement in the ORR activities.

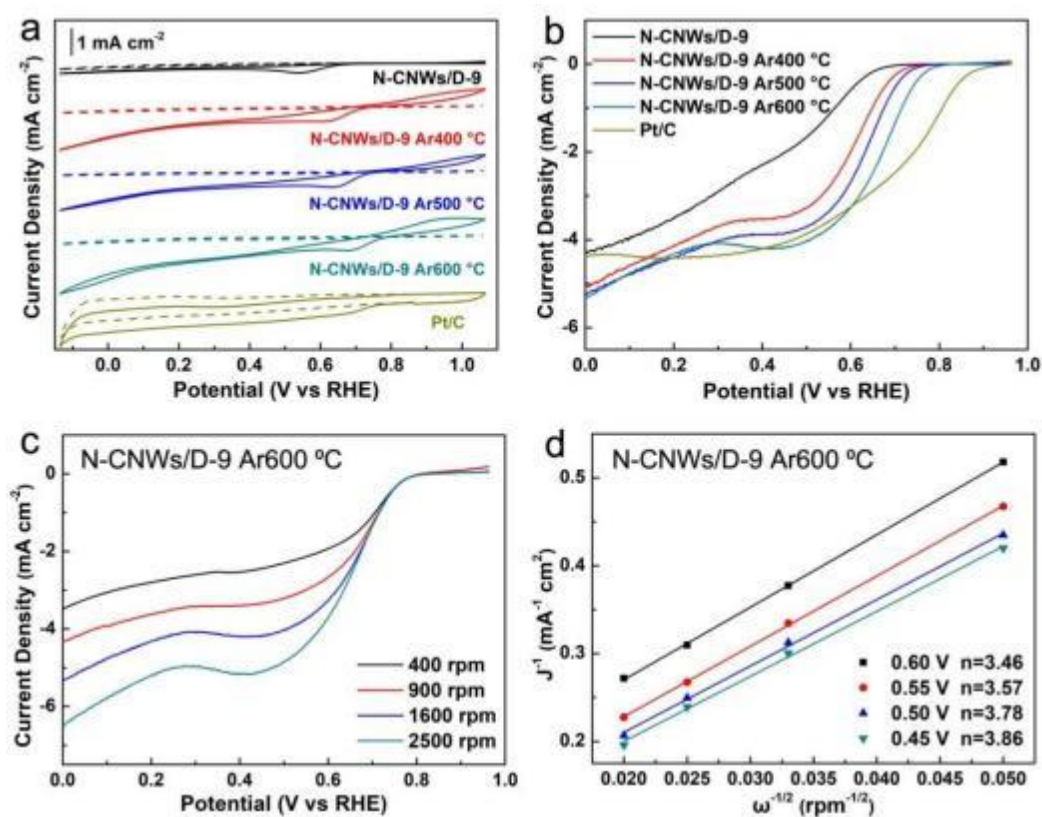


**Figure 4.8.** (a) CVs of as-prepared and Ar-treated N-CNWs/D-9 composites in  $N_2$  and  $O_2$  saturated 0.1 M KOH at a scan rate of  $100\ mV\ s^{-1}$ ; (b) the LSVs of as-prepared and Ar-treated N-CNWs/D-9 composites at a rotation speed of 1600 rpm in  $O_2$  saturated 0.1 M KOH at a scan rate of  $10\ mV\ s^{-1}$ ; (c) RDE curves of 600 °C Ar-treated N-CNWs/D-9 composite at different rotation speeds and (d) corresponding K-L plots.



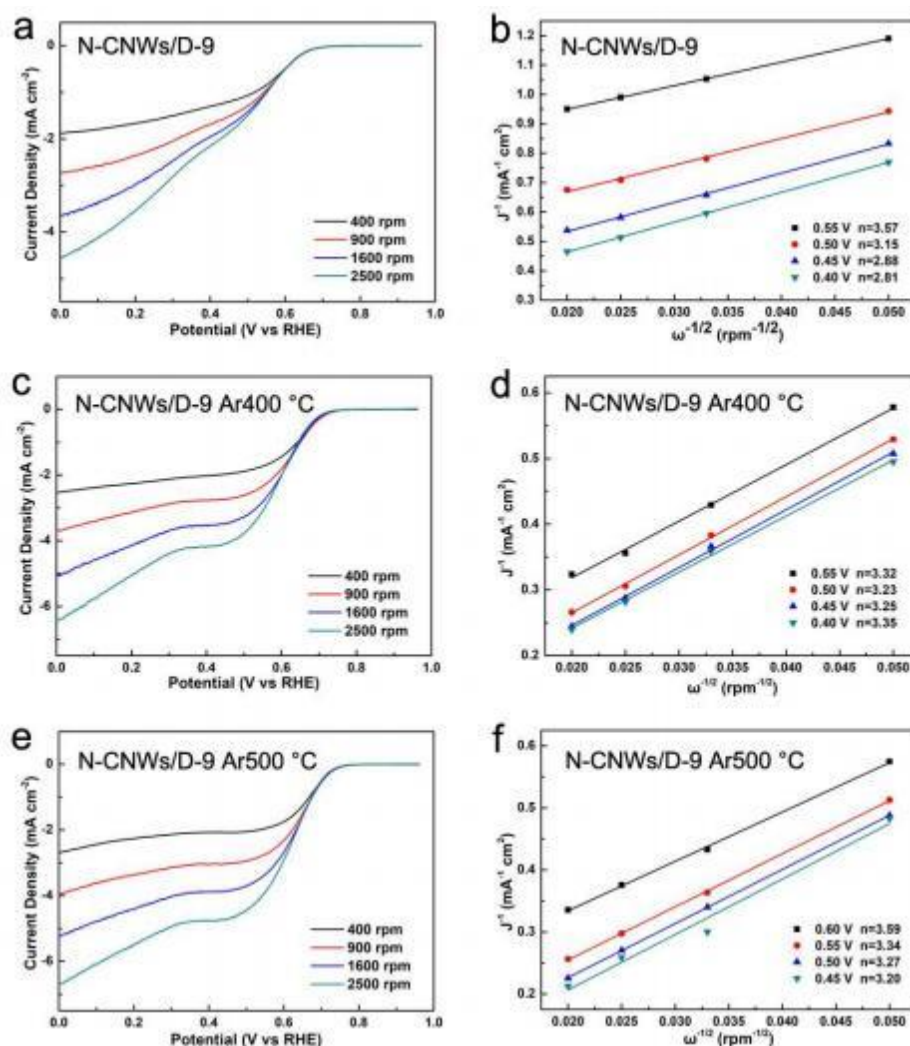


**Figure 4.9.** RDE curves tested at different rotation speeds (rpm) and the corresponding K-L plots ( $J^{-1}$  vs.  $\omega^{-1/2}$ ) for an as-prepared N-CNWs/D-9 composite (a, b) and annealed in a tube furnace at 400 °C (c, d) and 500 °C (e, f).

The reaction kinetics and high activity of the ORR on as-prepared and Ar-treated N-CNWs/D-9 composites were further confirmed by the rotating disk electrode (RDE) at a rotation speed of 1600 rpm. The N-CNWs/D-9 composites exhibit the improvement in limited diffusion current density and onset potential when the annealing temperature is increased (**Figure 4.8b**). Notably, the N-CNWs/D-9 composite after Ar annealing treatment at 600 °C presents the best ORR performance, as reflected by the most positive onset potential ( $E_{\text{onset}}$ ) of 0.835 V and the highest limiting current density ( $j_L$ ) of -4.18 mA cm<sup>-2</sup>. Such performance is far outdistancing that of as-prepared N-

CNWs/D-9 film, although still inferior to a conventional Pt/C catalyst. The LSVs of as-prepared and Ar-treated N-CNWs/D-9 composites recorded at different rotating rates (400-2500 rpm) (**Figure 4.8** and **Figure 4.9**) were employed to redraw the Koutecky-Levich (K-L) plots.

The K-L plots with high linearity and parallelism for the 600 °C Ar-treated N-CNWs/D-9 composite (**Figure 4.9d**) reveals the first-order kinetics for the ORR process [108]. The transferred electron number ( $n$ ), calculated by use of the K-L equation (see **chapter 3.4.2**) is around 3.86 at 0.45 V (*vs.* RHE) (**Figure 4.9d**) for the N-CNWs/D-9 composite after Ar annealing treatment at 600 °C. It is superior to that of as-prepared N-CNWs/D-9 composite ( $n = 2.88$  at 0.45 V *vs.* RHE) (**Figure 4.9a, b**). These numbers prove a mixture of [2+2]- and 4-electron ORR pathway on the N-CNWs/D-9 composite. Consequently, the Ar-treated N-CNWs/D-9 composite at 600 °C displays high ORR activity and great selectivity to a four-electron pathway, which also surpasses the highest onset potential of other reported CNWs and surface modified binder-free electrodes (**Table 4.6**). Obviously, much work should be devoted to further improve the ORR performance when compared with the powder form nitrogen-doped graphene catalysts.

**Table 4.6** Comparison of ORR performance on Ar-treated N-CNWs/D-9 composite with other analogous metal-free carbon-based catalysts.

Materials	$E_{\text{Onset}}$ vs RHE (mV)	$j_L$ (mA cm <sup>-2</sup> )	$n^a$	Ref
N-doped graphene	876	-5.21	3.89	[107]
VG/SPF-NCD/a-C	850	~-2.1	>4	[31]
P-CC	760	~-3.2	3.50	[109]
CNWs	770	~-2.5	2	[110]
hCNWs	830	-2.3	2	[104]
<b>Ar-treated N-CNWs/D</b>	<b>835</b>	<b>-4.18</b>	<b>3.86</b>	<b>This work</b>

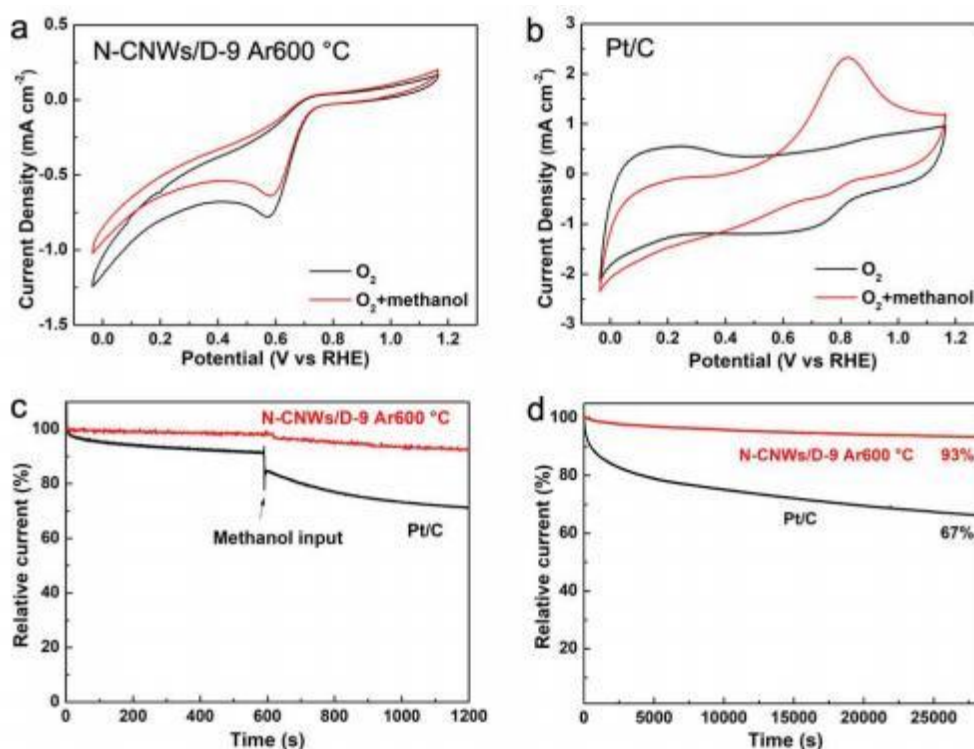


**Figure 4.10.** (a, b) CVs of the Ar-treated N-CNWs/D-9 composite (a) and Pt/C (b) in O<sub>2</sub>-saturated 1 M methanol/0.1 MKOH solution; (c) Chronoamperometric curves of the Ar-treated N-CNWs/D-9 composite and Pt/C in 0.1 M KOH solution before and after adding methanol; (d) Chronoamperometric curves of the Ar-treated N-CNWs/D-9 composite and Pt/C tested at 0.35 V vs. RHE in O<sub>2</sub>-saturated 0.1 M KOH solution.

The resistance to methanol crossover and long-term stability are known to be required for practical application in devices. The CVs of the Ar-treated N-CNWs/D-9 composite (**Figure 4.10a**) and a Pt/C catalyst (**Figure 4.10b**) were then collected in the electrolyte with and without methanol. The CVs of the Ar-treated N-CNWs/D-9 composite exhibit almost no change before and after the addition of methanol, revealing their comfortable tolerance to methanol crossover. For the Pt/C catalyst, the ORR peak is weakened while a new peak relating to methanol oxidation arises. In addition, the long-term stability of the N-CNWs/D-9 composite and the Pt/C catalyst was evaluated by recording the current-time (*i-t*) or chronoamperometric curves at 0.45 V (vs. RHE) with a rotating speed of 1600 rpm. During the measurement, pure oxygen gas was

continuously bubbled to ensure the O<sub>2</sub>-saturation of the electrolyte. When 3 M methanol was dropped into the electrolyte, no obvious change but slowly decreasing of the current for Ar-treated N-CNWs/D-9 composite was achieved, while the current decreases instantaneously for the Pt/C catalyst (**Figure 4.10c**). The long-term chronoamperometric response of the Ar-treated N-CNWs/D-9 composite and the Pt catalyst toward the ORR was also studied (**Figure 4.10d**). The current retention of the Ar-treated N-CNWs/D-9 composite remains the 93% of the initial current after 8 h, which is much higher than that (67%) of the Pt/C catalyst. Additionally, the top- and side-view SEM images (**Figure 4.11a, b**) suggest that the overall structure of the Ar-treated N-CNWs/D-9 composite is well retained after the ORR stability tests. The well-developed efficient and stable interface between the active sites embedded in the 3D network CNWs and electrolyte has been reserved, preventing the blockage of the mass transfer pathway and overwhelming of catalytic sites even during along-term reaction. It is demonstrated that the Ar-treated N-CNWs/D-9 composite possesses a higher resistance to methanol crossover as well as better stability than the Pt/C catalyst, which makes it a promising electrode for practical applications.

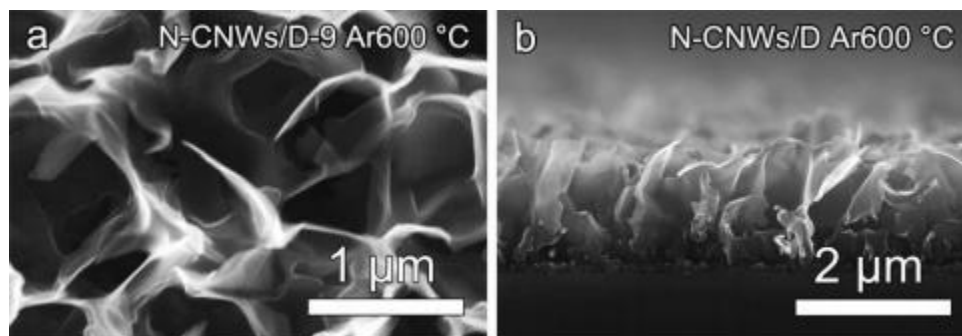


**Figure 4.11.** Top view (a) and side view (b) SEM images of an Ar-treated N-CNWs/D-9 composite after stability tests.

#### 4.4 Effect of an annealing treatment in terms of ORR activity

To precisely explore the effect of Ar treatment on the microstructure of as-prepared and Ar-treated N-CNWs/D-9 composites, their TEM images were recorded (**Figure**

**4.12).** An as-prepared N-CNWs/D-9 composite contains several graphene layers. Their interlayer spacing was measured to be 0.35 nm, which is in agreement with our previous work [111]. The Ar-treated N-CNWs/D-9 composite exhibits an increased spacing of graphene layers (e.g., up to 0.38 nm). The histograms of the thickness of two kinds of composites were obtained from more than 100 locations for each sample (**Figure 4.12e, f**). The histogram of the N-CNWs/D-9 composite reveals a maximum thickness of 20-25 nm. For the N-CNWs/D-9 composite after the Ar-annealing treatment (**Figure 4.12f**), its thickness peak lies up to 30-35 nm. Therefore, the Ar-annealing treatment can directly change the microstructure of the N-CNWs/D-9 composite, namely the expanded interspace between layers, resulting in the thicker graphene layers. Furthermore, the Ar-treated N-CNWs/D-9 composite possesses a highly disordered crystal structure (**Figure 4.12d**). The N-CNWs/D-9 composite with such a structure is expected to provide more edge plane sites and lattice defects inline with those observed in the previous Raman and XPS results.

Furthermore, the compositions and chemical states of as-prepared and Ar-treated N-CNWs/D-9 composites were analyzed by means of XPS. For example, the XPS C1s spectra of an as-prepared (**Figure 4.13a**) and the Ar-treated (**Figure 4.13b**) N-CNWs/D-9 composites were recorded. Compared to an as-prepared N-CNWs/D-9 composite, the ratio of  $sp^2/sp^3$  C of the Ar-treated N-CNWs/D-9 composite is decreased from 2.84 to 2.28 (**Table 4.7**), implying the presence of more defects and edges, which is again in line with the TEM and Raman results.

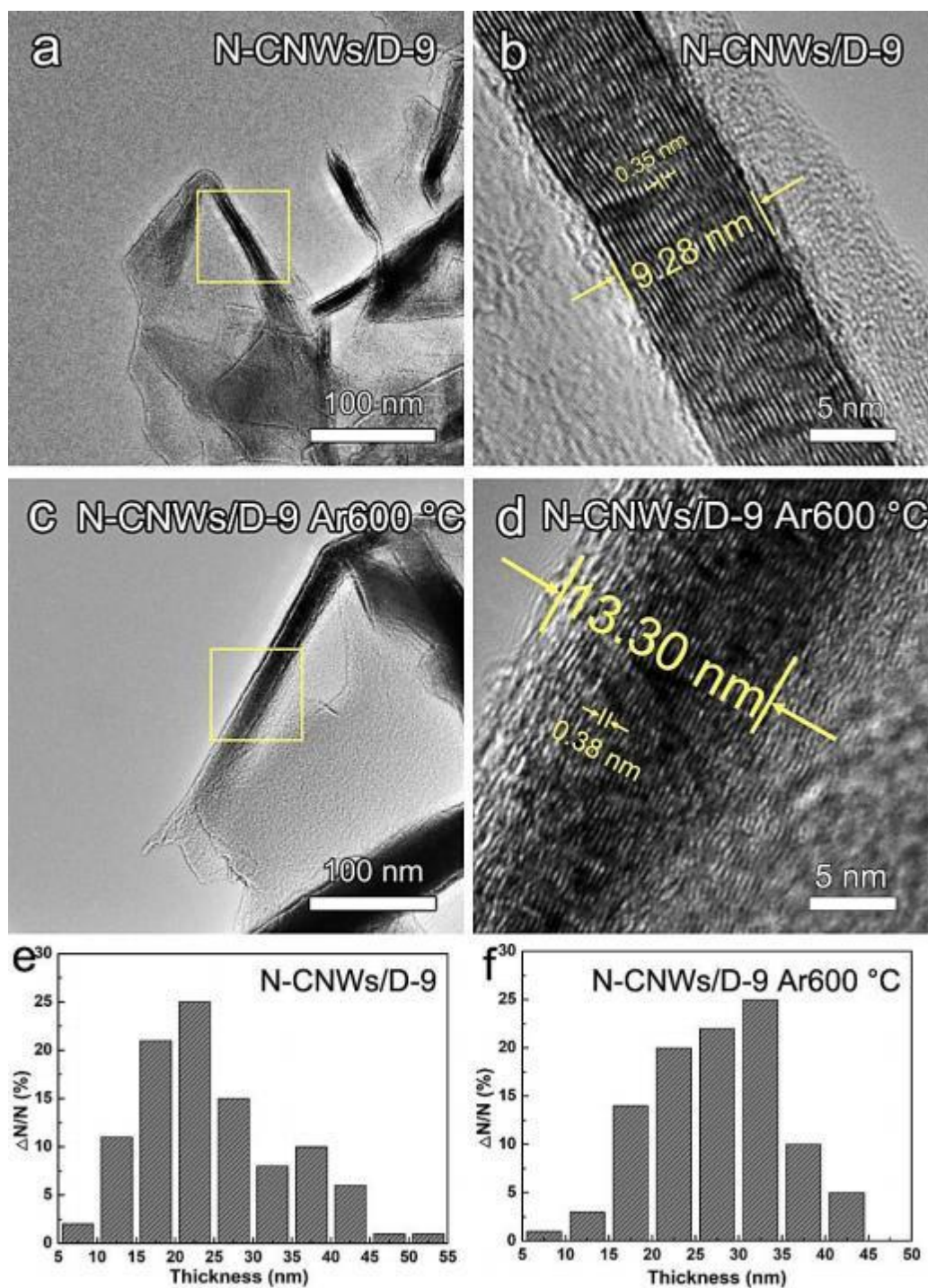


**Figure 4.12.** HRTEM images of the N-CNWs/D-9 composite layer (a) before and (b) after Ar-annealing treatment at 600 °C; Histograms of the thickness of the N-CNWs/D-9 layer (c) before and (d) after Ar-annealing treatment at 600 °C.



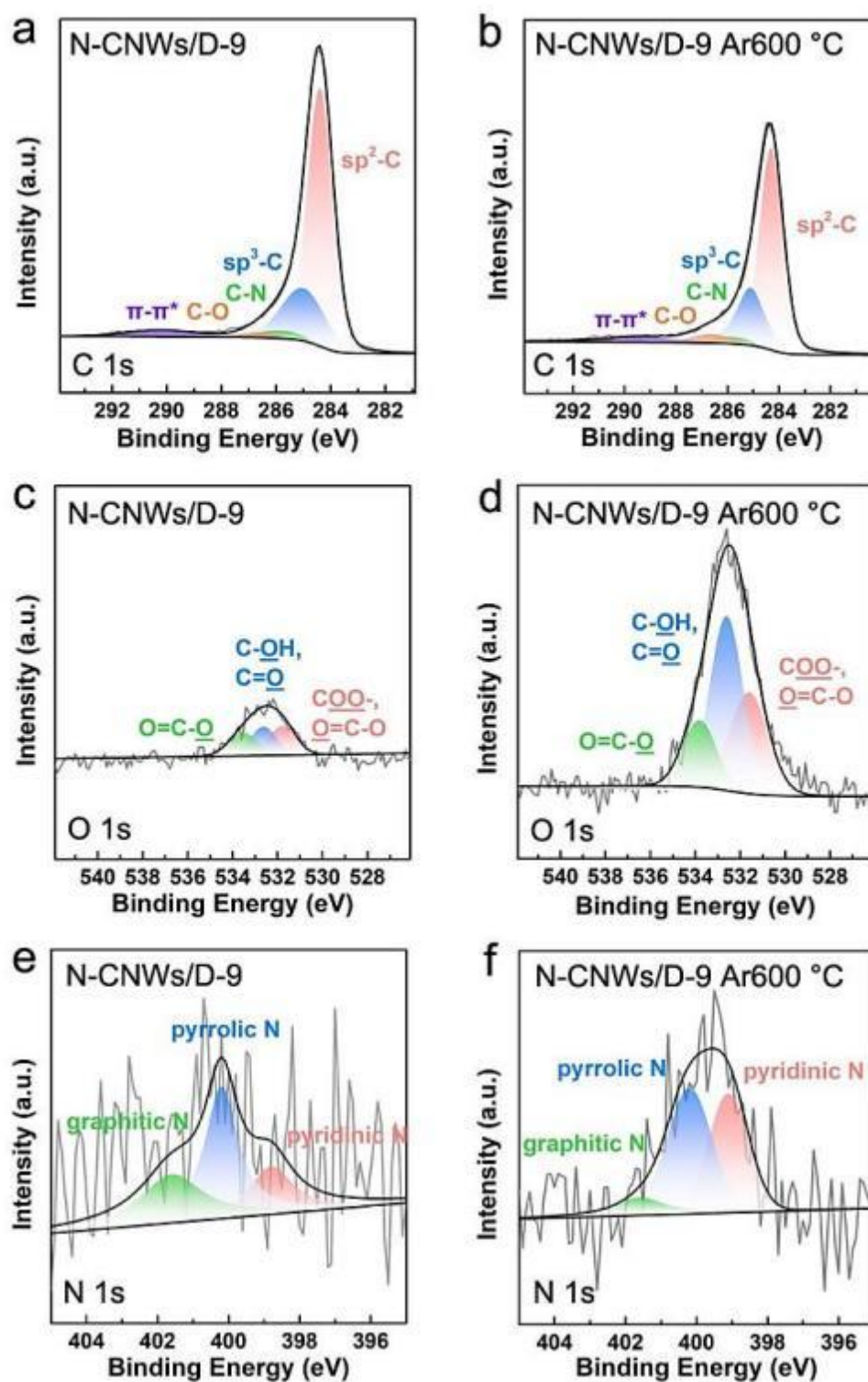


**Figure 4.13.** (a, b) High-resolution XPS C 1s spectra, (c, d) O 1s spectra, (e, f) N 1s spectra of N-CNWs/D-9 composites before and after Ar annealing treatment at 600 °C.

After the Ar-annealing treatment, there is an obvious increase of oxygen content (e.g., from 1.1% for as-prepared to 5.5% for the Ar-treated N-CNWs/D-9 composites). The peaks of O1s in an as-prepared (**Figure 4.13c**) and Ar-treated N-CNWs/D-9 (**Figure 4.13d**) composites can be split into three contributions (**Table 4.8**), including the carboxyl group (COO-) in carboxylate and the oxygen double bond to carbon (O=C-O) at 531.6 eV, the hydroxyl (C-OH) and carbonyl (C=O) functional groups at 532.6 eV, and the oxygen single bond in esters and carboxylic acids (O=C-O) at 533.8 eV [109]. The contents of three types of oxygen functional groups are increased after the Ar-annealing treatment, probably resulted from carbon oxidation at the edge defects after exposing them in air. Interestingly, the nitrogen content on the surface of the N-CNWs/D-9 composite is slightly increased from 1.5% to 1.7% (**Table 4.9**). In addition, the high resolution XPS N 1s spectra of as-prepared (**Figure 4.13e**) and Ar-treated (**Figure 4.13f**) N-CNWs/D-9 composites were de-convoluted. The distribution of graphitic N is found to be decreased from 31.7% for as-prepared N-CNWs/D-9 composites to 11.6% for the Ar-treated ones, while that of pyridinicN is increased from 22.2% to 40.5% (**Table 4.9**). The conversion of nitrogen species is owing to more edge defects generated by the annealing treatment [112]. Overall, the Ar-annealing treatment creates more lattice and edge defects, as well as more oxygen functional groups on the N-CNWs/D-9 composite. Meanwhile, the nitrogen doping sites have been partially conversed and activated.

**Table 4.7.** Distribution of C species obtained from the de-convolution of the C 1s peaks by XPS.

Sample	sp <sup>2</sup>	sp <sup>3</sup>	sp <sup>2</sup> /sp <sup>3</sup>	C-N	C-O	$\pi$ - $\pi^*$
N-CNWs/D-9	66.7	23.5	2.8	3.6	1.9	4.3
N-CNWs/D-9 Ar600 °C	59.9	26.2	2.3	3.3	4.3	6.3



**Table 4.8.** Distribution of O species obtained from the de-convolution of the O 1s peaks by XPS.

Sample	COO-	C-OH	O=C-O
N-CNWs/D-9	36.1	33.4	30.5
N-CNWs/D-9 Ar600 °C	33.5	47.7	18.9

**Table 4.9.** Distribution of N species obtained from the de-convolution of the N 1s peaks by XPS.

Sample	pyridinic N	pyrrolic N	graphitic N
N-CNWs/D-9	22.2	46.1	31.7
N-CNWs/D-9 Ar600 °C	40.5	47.9	11.6

In spite of the micro-/nano-structure and electronic structure of these N-CNWs/D-9 composites, the surface properties of these film electrodes are also essential to their catalytic performance. To check such a micro/nano-structure, the static water contacts angles (SCAs) of the as-prepared and Ar-treated N-CNWs/D-9 composites were measured (**Figure 4.14a**). The SCA of an as-prepared N-CNWs/D-9 composite is 136°, suggesting its high hydrophobic properties. After the Ar-annealing treatment, the SCA of the N-CNWs/D-9 composite is decreased to 34°, an indication of a hydrophilic surface. This originates from an increase of oxygen function groups at edges and defects of basal planes and the change of the H-terminated surface to O-terminated one [113]. Such a modified surface is more beneficial to electrolyte infiltration, dissolved oxygen, and ion transportation. Furthermore, the CVs of two films were accomplished at scan rates between 4 and 20 mV s<sup>-1</sup> in 0.1 M KOH (**Figure 4.14b, c**). Their electrochemical surface areas (ECSAs) were then estimated by their electrochemical double-layer capacitances ( $C_{dl}$ ). The  $C_{dl}$  of an Ar-treated N-CNWs/D-9 film is increased from 13.3

$\mu\text{F}$  for an as-prepared N-CNWs/D-9 composite to  $178.3 \mu\text{F}$ , which can be attributed to the enhanced surface wettability, and more accessible active sites involved in the electrocatalytic reaction [114, 115].

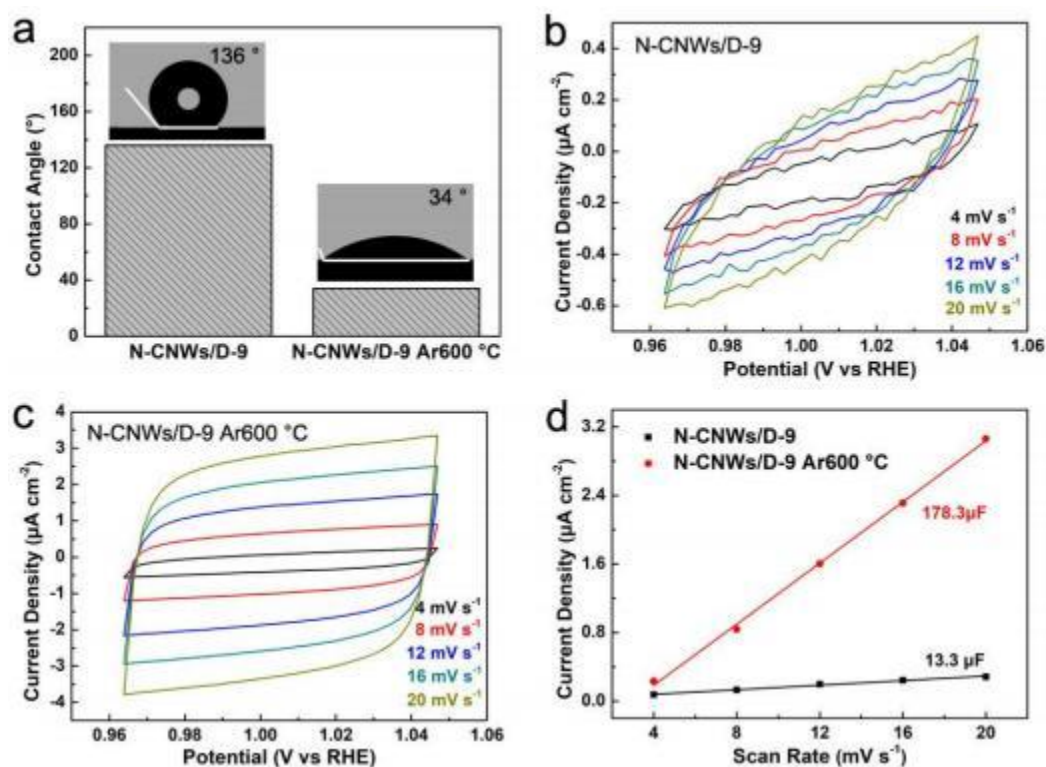


**Figure 4.14.** (a) SCA of water droplet on the N-CNWs/D-9 composite before and after Ar-annealing treatment at 600 °C; (b, c) The CVs in the potential region of 0.96 - 1.04 V (vs. RHE) in 0.1 MKOH of (b) an as-prepared N-CNWs/D-9 composite and (c) Ar-treated N-CNWs/D-9 composite; (d) The corresponding electrochemical double-layer capacitances.

The results from Raman, TEM, XPS, SCA, and ECSAs lead one to conclude that more active sites generated by the Ar-annealing treatment endow the enhanced ORR activity. The surface wettability of the N-CNWs/D composites is improved and a large contact area of a real reaction tri-phase is obtained, attributing to a fast mass and ion transport pathway. Significantly, it can be explicated that the activated pyridinic N species at graphene edges after the Ar-annealing treatment plays significant roles on the enhancement of ORR selectivity and activity. As the nitrogen doping at graphene edges

has been reported to be favorable to promote the adsorption of  $O_2$ , the first electron transfer process (equal 4) is facilitated, leading to decreased ORR overpotentials [116]. Meanwhile, the pyridinic-like N conversing from the outermost graphitic N has been considered to be the active site in the reduction of  $OOH^-$  (equal 4.2). It thus results in highly selectivity toward the four-electron pathway (as depicted in **Figure 4.15**) [117, 118].

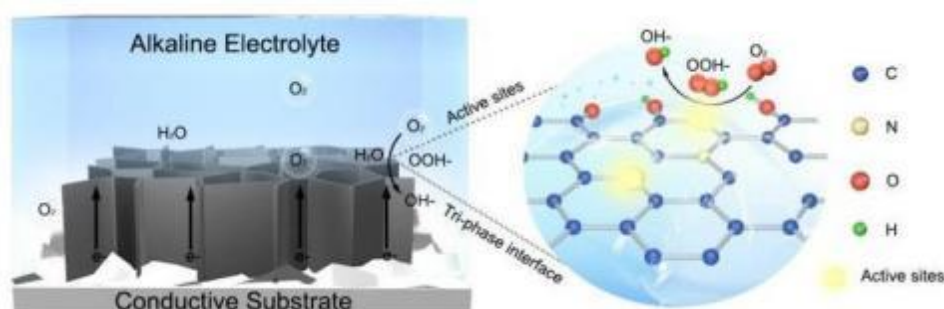
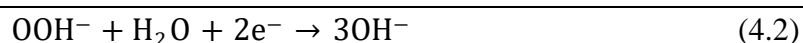
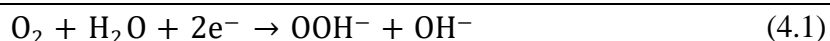


**Figure 4.15.** Schematic pathway for oxygen reduction reaction on the Ar-treated N-CNWs/D composites.

## 4.5 Conclusions

A controllable method is proposed using a MPCVD system to fabricate high-quality N-CNWs/D composites, namely by introduction of nitrogen during the CVD growth process to realize N dopants into graphite lattice. More lattice disorders and edge defects are further generated by the Ar-annealing post-treatment. The resultant Ar-treated N-CNWs/D composite possesses not merely a robust interface with appropriate nitrogen dopants, but also a large electrochemical surface area, exhibiting more accessible active sites for the ORR. In addition, its interconnected and vertical 3D network nanostructure provides a fast electron and mass transfer pathway, accelerating the kinetics of reaction process. Consequently, the Ar-treated N-CNWs/D-9 composite exhibits satisfactory ORR activity (with  $E_{onset}$  of 0.835 V vs. RHE and  $j_L$  of -4.18 mA

cm<sup>-2</sup>), four-electron selectivity ( $n=3.85$ ), excellent stability and methanol tolerance. In summary, this work provides a scalable method to synthesis a unique binder-free carbon-based film catalyst. A throughout understanding for the ORR kinetics is also presented to explore more novel 3D network nanostructure catalysts for practical devices.

## 5 Co<sub>4</sub>N@d-NCNWs/D composites for electrocatalytic ORR/OER and zinc-air batteries

Metal-nitrogen-carbon (M-N-C) systems are composed of earth-abundant transition metal compounds and carbon substrates. They have received enormous interest for different catalytic reactions, especially the cobalt-based ones, due to their low-costs and high efficiencies [119, 120]. On one hand, cobalt-based compounds (e.g., oxides, hydroxide, nitride, etc.) hold superior intrinsic activities, originated from their multipole valences and various chemical compositions [121, 122]. On the other hand, carbon-based materials (e.g., graphene, carbon nanotubes, etc.) can enhance the adsorption of oxygen and related intermediates after their modification with intrinsic defects and heteroatom doping [59]. Particularly, the Co-N-C bond formed at the interface of carbon and cobalt is considered to be a highly active site for the ORR, while the Co-Co or Co-N bonds presented in cobalt nitride (Co<sub>4</sub>N) are the active centers for the OER [123]. Unfortunately, the overall catalytic performance of such composites is often limited by the morphology of carbon supports, the sizes and distribution of Co<sub>4</sub>N nanoparticles, and the coordination environment at the heterointerface. Hitherto, the effective combination of the Co-N-C bonds with highly active Co<sub>4</sub>N nanoparticles at the composite interface, is still a daunting challenge.

Carbon nanowalls/diamond (CNWs/D) composite is a newtype of catalyst support. It consists of vertically aligned multilayer graphene that are directly grown on diamond. If it is further deposited on a current collector, an integrated electrode can be assembled [124]. Note that the (CNWs/D) composites have exhibited excellent ORR performance, caused by the vertical electron transfer pathway and a large number of exposed edge sites. Meanwhile, these composites lack strong bridged bonds and interactions, owing to the huge mismatch of lattice constants and fermi levels between ideal graphite and metals. Such composites are thus expected to have inhomogeneous loadings and insufficient active sites. It has been also reported that modification of a substrate by means of surface hydroxylation [125], heteroatom doping [126] and the generation of

vacancy defects can reduce the substrate surface energy and improve the interaction between the supports and metal nanoparticles since these approaches introduce anchoring sites for metal atoms [127]. With such a strong metal-supporting interaction (SMSI), an electronic effect is possible to be induced on the heterointerface, namely to have an impact on the ORR/OER reaction pathways.

In this chapter, the DFT calculations were firstly employed to elucidate the effects of different configurations of N dopants on the coordination environments at the heterointerface of the Co<sub>4</sub>N@d-NCNW/D composite. Subsequently, as-synthesized Co<sub>4</sub>N@d-NCNW composites were characterized and their ORR/OER performance was analyzed. To explore the practical applications, this composite was used as an air-cathode to assemble rechargeable aqueous and flexible Zn-Air batteries. Since this work provides both experimental and theoretical evidence for the electrocatalytic mechanism of Co-N-C catalysts, it thus shines new light into the structural design of binder-free ZAB cathodes for practical applications.

### 5.1 DFT calculations of heterointerface and ORR/OER mechanisms

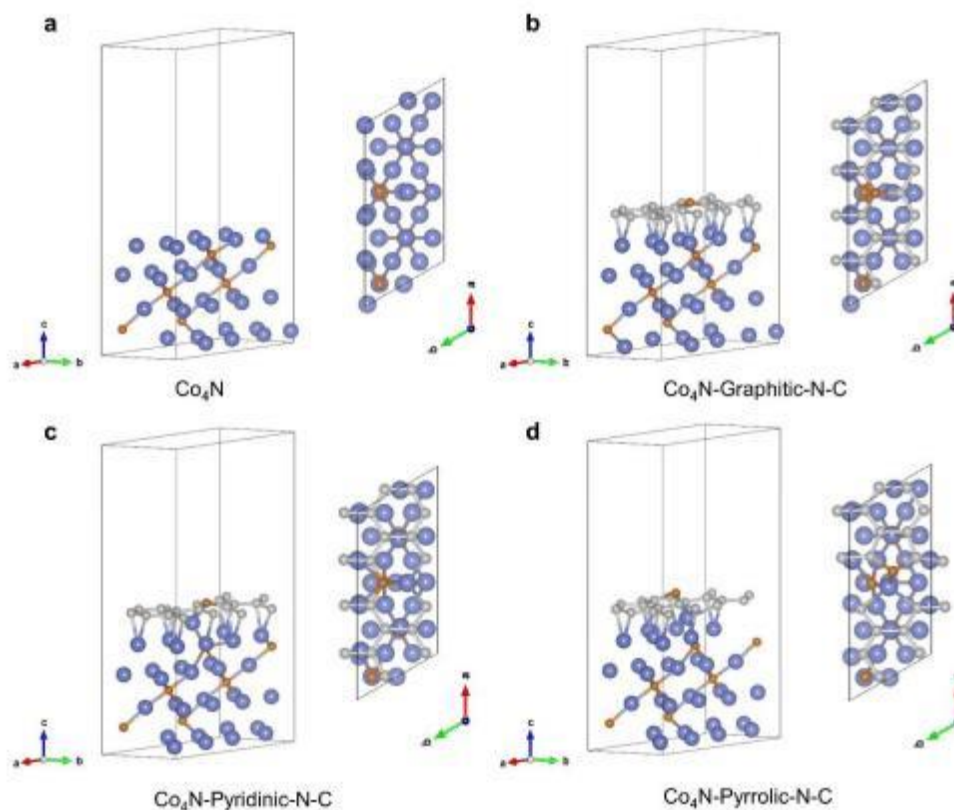


**Figure 5.1.** Module of (a) Co<sub>4</sub>N (111) facet, (b) Co<sub>4</sub>N-Graphitic-N-C interface, (c) Co<sub>4</sub>N-Pyridinic-N-C interface, (d) Co<sub>4</sub>N-Pyrrolic-N-C interface.

Prior to synthesis of as-mentioned catalysts, the DFT calculations were firstly conducted to investigate the influence of nitrogen dopants on different coordination environments. Several models of graphene monolayers were constructed with graphitic N atoms, pyridinic N atoms, pyrrolic N atoms and their compounds with cobalt nitride (**Figure 5.1**). When N dopants have different configurations (**Figure 5.2a**), the difference of the Bader charges and charge densities on the interface of these models can be calculated (**Figure 5.2b**). The charge distribution at the heterointerface is formed to be influenced by different configurations of nitrogen dopants in graphene monolayers. The charge densities of carbon atoms near pyridinic N atoms are stronger than those of graphitic N atoms, namely with a value shift from +0.2 to +0.4. This charge transfer can be considered as an effect of interfacial charge redistribution, arising from the

formation of a heterojunction [128]. Theoretically, the strength and direction of this charge transfer are known to be highly dependent on the type of metal nanoparticles and doped nitrogen configurations [129]. In this context, the charge transfer from Co<sub>4</sub>N to nitrogen-doped graphene occurs. It becomes starker when the dopants of pyridinicN atoms are presented. Meanwhile, an enhanced charge transfer is suggested to imply stronger interactions, impacting on the electronic structures of bonding atoms [130].

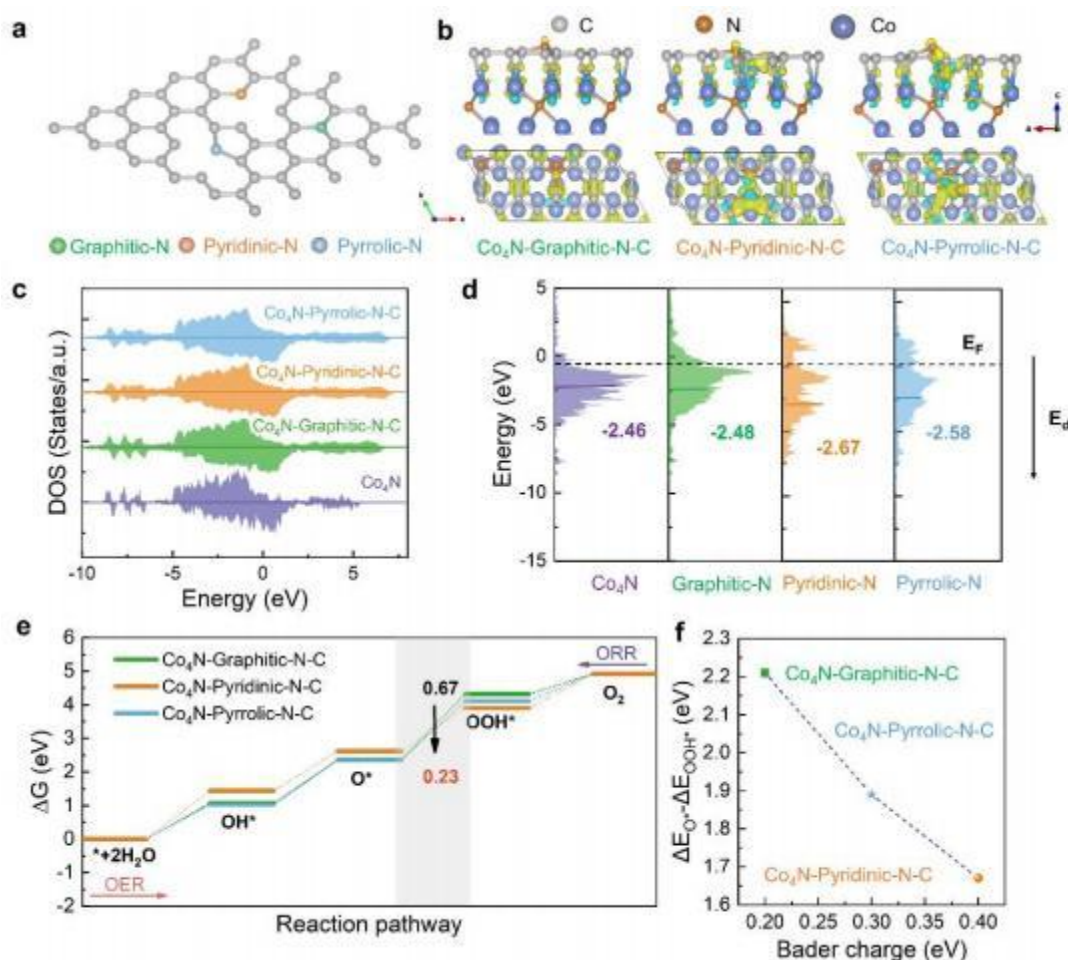


**Figure 5.2.** (a) Different configurations of N dopants in monolayer graphene, (b) Charge density differences on the interface of Co<sub>4</sub>N-Graphitic-N-C, Co<sub>4</sub>N-Pyridinic-N-C and Co<sub>4</sub>N-Pyrrolic-N-C, (c) Density of states (DOS) of different interfaces, the Fermi level is shifted to 0 eV, (d) Projected DOS (PDOS) of the Co 3d orbitals and d-band center in different interfaces, (e) The calculated free energy diagrams for the ORR/OER of Co<sub>4</sub>N-Graphitic-N-C, Co<sub>4</sub>N-Pyridinic-N-C and Co<sub>4</sub>N-Pyrrolic-N-C. (f) The relationship between the Bader charge and the free energy of  $\text{O}^*$ - $\text{OOH}^*$ .



The density of states (DOS) of the Co<sub>4</sub>N, Co<sub>4</sub>N-Graphitic-N-C, Co<sub>4</sub>N-Pyridinic-N-C and Co<sub>4</sub>N-Pyrrolic-N-C interfaces were calculated (**Figure 5.2c**). The projected DOS (PDOS) of the Co 3d orbitals was calculated and investigated together with the *d*-band center in the Co<sub>4</sub>N, Co<sub>4</sub>N-Graphitic-N-C, Co<sub>4</sub>N-Pyridinic-N-C and Co<sub>4</sub>N-Pyrrolic-N-C interfaces (**Figure 5.2d**). The electron transfers away from Co<sub>4</sub>N to nitrogen-doped graphene is found to cause a decrease in the density of electronic states near the Fermi level. A downshifting *d*-band center of the Co<sub>4</sub>N-Graphitic-N-C, Co<sub>4</sub>N-Pyridinic-N-C and Co<sub>4</sub>N-Pyrrolic-N-C is varied from -2.46 to -2.48, -2.67 and -2.58 eV. In the *d*-band center theory [131], the position of the *d*-band center is known to represent the filling degree of its antibonding orbitals when combined with adsorbed molecules. This thus determines the stability of the bonding and the adsorption strength of a molecule [132]. Therefore, the downshift of the *d*-band center in our case implies an increased desorption for certain oxygen-contained intermediates, which is essential to balance the adsorption energies of intermediates at the active sites and eventually to reduce the energy barriers for both ORR and OER. In addition, the charge transfer towards carbon atoms increases the electronic states density near the Fermi level, resulting in the enhanced adsorption of oxygen molecules to the carbon substrate [133].

To further elaborate the effect of electronic structures on the reaction mechanisms of the ORR/OER, the Gibbs free energies of each step along different reaction pathways were calculated (**Figure 5.2e**). Note that for the C site, the rate-limiting step in the ORR/OER is the conversion process from O\* intermediates to OOH\* intermediates. Namely, the ORR/OER activity is governed by the adsorption strength of the OOH\* intermediates. In contrast, on the Co site, the rate-limiting step is the detachment of OH\* intermediates [134]. Hence, when the nitrogen-doped graphene composites are compounded with Co<sub>4</sub>N, the energy barrier for the O\*-OOH\* process is gradually decreased. Meanwhile, the desorption of OH\* intermediates is greatly improved, corresponding to the downshift in the *d*-band center. Consequently, the enhanced Co-pyridinic N-C bonds at such an heterointerface are the highly active sites and

dramatically reduce the total reaction overpotential of ORR/OER from 0.67 to 0.23 eV. Consequently, the pyridinic N dopants induce an interfacial electronic effect. They play a key role in promoting the bi-functional ORR/OER performance of the Co<sub>4</sub>N-Pyridinic-N-C composites (**Figure 5.2f**).

## 5.2 Characterization of Co<sub>4</sub>N@d-NCNWs/D composites

Triggered by these simulation results, a strategy to modify the CNWs/D composites was developed (described in chapter 3.2.2), where more defects and pyridinic N dopants were introduced. In this way, the interfacial effects between Co<sub>4</sub>N nanoparticles and the d-NCNWs/D composites were clarified. Initially, then knife-shape CNWs/D are vertically grown on the individual CC fibers by means of a MPCVD technique, followed by electro-oxidation pretreatment to realize surface modification. The CC consists of connected textile carbon fibers with a diameter of approximately 10  $\mu\text{m}$  (**Figure 5.3a** and inset). After the application of a MPCVD process, the entire surface of the CC is uniformly coated with densely interlaced CNWs/D, of which thickness is about 500 nm (**Figure 5.3b**). The electro-oxidation pretreatment did not change the morphology of the d-CNWs/D significantly (**Figure 5.3c**), indicating that this treatment does not disrupt the three-dimensional structure of CNWs, although their microscopic structure and chemical surface states might be varied. Further electrodeposition of Co (OH)<sub>2</sub> nanoplatelets (**Figure 5.3d**) is then conducted on the d-CNWs/D composite, followed by the annealing treatment of this composite in an Ar/H<sub>2</sub> atmosphere at 600 °C. During this annealing process, melamine was added. Thin Co (OH)<sub>2</sub> nanoplatelets were then minimized to small Co<sub>4</sub>N nanoparticles on d-NCNWs/D. Namely, the Co<sub>4</sub>N@d-NCNWs/D composites are synthesized.

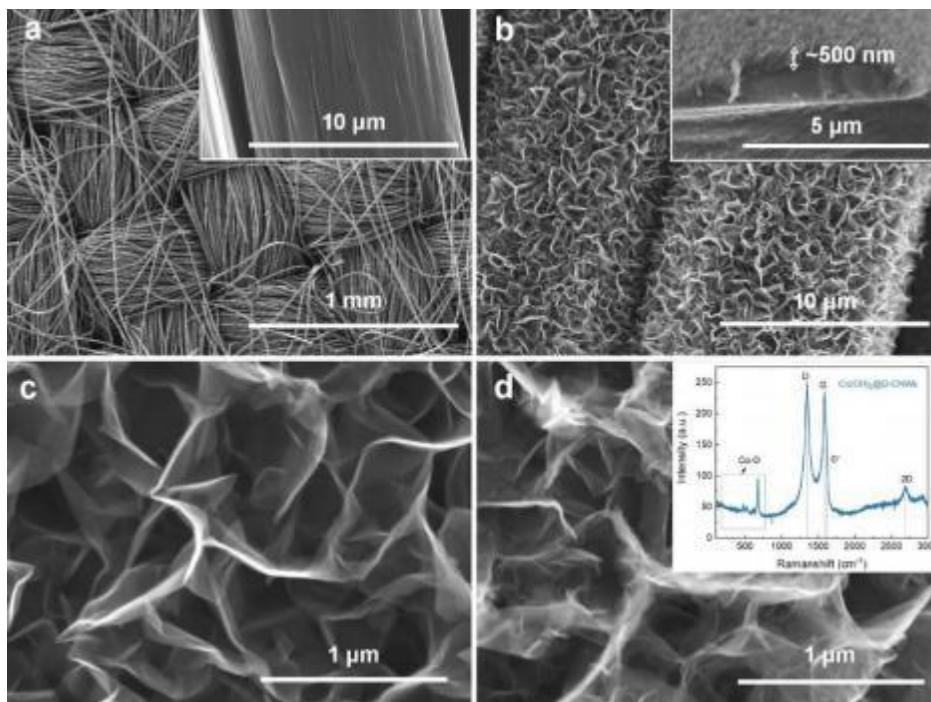


**Figure 5.3.** SEM images of (a) CC, (b) CNWs/D composite on CC, (c) d-CNWs/D composite on CC, (d) Co (OH)<sub>2</sub> nanoplatelets on the d-CNWs/D composite, Raman spectrum of Co (OH)<sub>2</sub> nanoplatelets on the d-CNWs/D composite (inset).

As-synthesized Co<sub>4</sub>N@d-NCNWs/D composites were then characterized using different microscopy, spectroscopy, and electrochemical techniques. In their SEM images (**Figure 5.4a** and **b**), Co<sub>4</sub>N nanoparticles are noticed to be uniformly dispersed on the d-NCNWs/D composite and their mean size is smaller than 10 nm. For comparison, the Co<sub>4</sub>N@NCNWs/D composites were prepared using the same synthetic procedure but without the electro-oxidation pretreatment of CNWs/D. In their SEM images, inhomogeneous Co<sub>4</sub>N nanoparticles are seen and some of them are partially connected into individual islands (**Figure 5.4c**). This might be due to the weak interactions between Co<sub>4</sub>N nanoparticles and the NCNWs/D composite. More remarkably, the diameter of Co<sub>4</sub>N nanoparticles that are directly grown on the CC film without the CNWs/D composite is distinctly bigger (**Figure 5.4d**). These results suggest that the d-NCNWs/D composite can serve as a suitable three-dimensional network to

support well-dispersed metal nanoparticles and meanwhile enhance the interaction between Co<sub>4</sub>N nanoparticles and the d-NCNWs/D composite. The latter effectively resists the sintering, caused by Ostwald ripening [42].

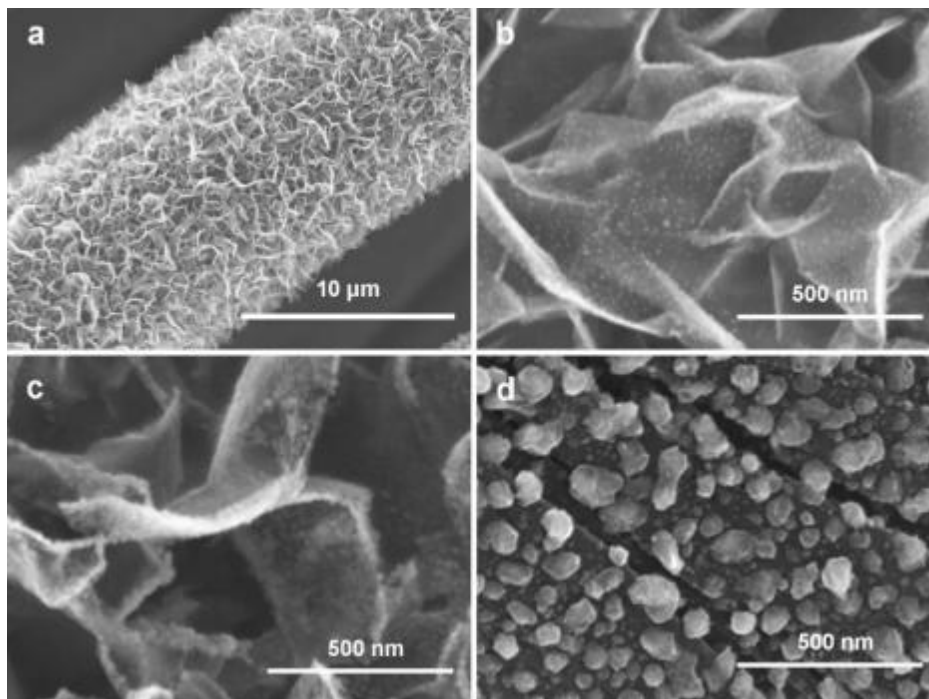


**Figure 5.4.** SEM images of (a, b) Co<sub>4</sub>N@d-NCNWs/D composite, (c) Co<sub>4</sub>N@NCNWs/D composite and (d) Co<sub>4</sub>N nanoparticles.

To precisely investigate the morphology and crystallographic features of the Co<sub>4</sub>N@d-NCNWs/D composites, their high-resolution transmission electron microscopy (HRTEM) images and the X-ray diffraction (XRD) patterns were collected. Their HRTEM image (**Figure 5.5b**) depicts densely dispersed Co<sub>4</sub>N nanoparticles. According to a standard distribution, the average diameter of these nanoparticles is about 2.5 nm, much smaller than that of those previously reported [135, 136]. The lattice fringes of such a nanoparticle (**Figure 5.5b**) reveal a Co<sub>4</sub>N (111) plane with the interlayer space of ~2.1 Å, slightly larger than that (2.04 Å) of a Co (111) plane. This is probably due to the doping of N heteroatoms into the lattice spaces during the nitridation process [137]. In the related fast Fourier transform (FFT) patterns (the inset in **Figure 5.5b**), the lattice spacings of 0.211, 0.209, and 0.189 nm are associated with

the (111) and (200) crystal planes of an *fcc* Co<sub>4</sub>N phase. The sections around the blue arrows are consistent with a graphite (002) plane with an interlayer spacing of about 3.4 Å. Therefore, Co<sub>4</sub>N nanoparticles are successfully anchored on the d-NCNWs/D composite. In addition, the XRD diffraction patterns of the Co<sub>4</sub>N@d-NCNWs/D composite (**Figure 5.5c**) further confirm the present of Co<sub>4</sub>N nanoparticles. The dominant peaks are located at 51.2° and 59.8°, assigned to the (111) and (200) facets of *fcc* Co<sub>4</sub>N phase (JCPDS 41-0943), respectively. The broad peak in the range of 22 to 34° corresponds to a defective carbon structure [138].

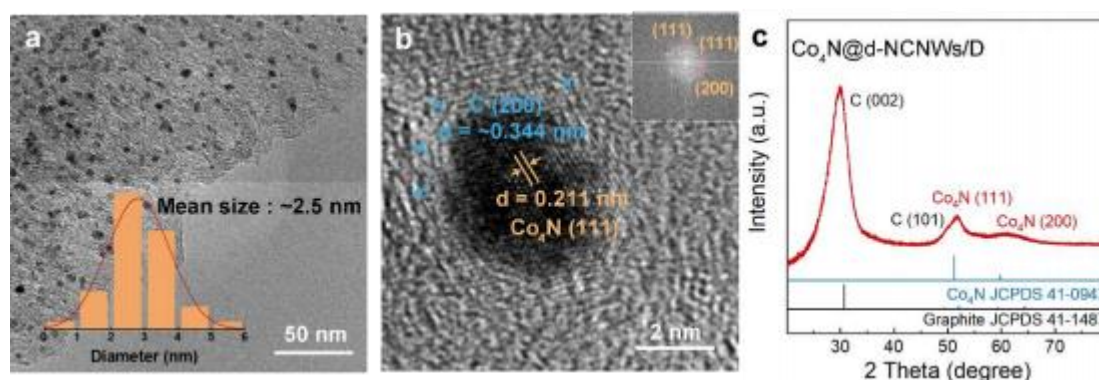


**Figure 5.5.** (a) TEM image and size distribution (inset) of Co<sub>4</sub>N nanoparticles on the d-NCNWs/D. (b) HRTEM image of the Co<sub>4</sub>N@d-NCNWs/D and related FFT pattern (inset). (c) XRD patterns of the Co<sub>4</sub>N@d-NCNWs/D composites.

As presumed by the DFT calculations, the properties of the Co<sub>4</sub>N@d-NCNWs/D composites are highly dependent on the coordination environments at their heterointerface. Chemical elements and bonding configurations of the Co<sub>4</sub>N@d-NCNWs/D composites were then investigated by means of X-ray photoelectron spectroscopy (XPS). In their full XPS surveys (**Figure 5.6a,b, c**), the elements of C, N, Co, and O are detected on the surface and their contents were estimated (**Table 5.1**). In high-resolution C 1s spectrum of the Co<sub>4</sub>N@d-NCNWs/D composite (**Figure 5.6d**), the deconvolution peaks at 283.9, 285.3, and 287.1 eV are assigned to sp<sup>2</sup>-C, sp<sup>3</sup>-C, and C-N, respectively. Since the ratio of sp<sup>2</sup>-C to sp<sup>3</sup>-C usually corresponds to the defect degree in a graphite material [109], the presence of sp<sup>3</sup>-C and C-N peaks jointly indicate

that N atoms are successfully doped into the carbon lattice of the Co<sub>4</sub>N@d-NCNWs/D composites. Their proportions are higher than those of the unmodified Co<sub>4</sub>N@NCNWs/D composites (**Table 5.2**). The N 1s spectrum of the Co<sub>4</sub>N@d-NCNWs/D (**Figure 5.6e**) was fitted with four types of nitrogen configurations. They are located at 397.8, 398.3, 399.2, and 400.5 eV, corresponding to pyridinicN, Co-N, pyrrolic N, and graphitic N, respectively. These results further demonstrate the simultaneous formation of C-N and Co-N bonds in the Co<sub>4</sub>N@d-NCNWs/D composite. The N 1s spectrum of the d-NCNWs composite was also de-convoluted into four peaks. They are centered at 398.2, 400.5, 402.8, and 404.3 eV, stemming from pyridinic N, pyrrolicN, graphitic N, and oxidized N, respectively. However, there is no Co-N bond (**Figure 5.7**). Moreover, the total N content in the d-NCNWs/D is 6.3%, much lower than that (9.1%) in the Co<sub>4</sub>N@d-NCNWs/D composite. More importantly, the proportion of pyridinic N in the Co<sub>4</sub>N@d-NCNWs/D composite is 35%, significantly higher compared to that (28%) in the unmodified Co<sub>4</sub>N@NCNWs/D composite (**Table 5.3**). This indicates that the electro-oxidation pre-treatment of the Co<sub>4</sub>N@d-NCNWs/D composite does lead to the formation of pyridinic N atoms. Furthermore, the Co 2p spectrum of the Co<sub>4</sub>N@d-NCNWs/D composite was de-convoluted (**Figure 5.6f**). The peaks for the Co<sup>3+</sup> species, the Co<sup>2+</sup> species, and the Co-N bond are observed at 780.1, 782.5, and 784.3 eV, respectively. Note that the proportion of the Co-N bond in the Co<sub>4</sub>N@d-NCNWs/D composite is higher compared to that in the Co<sub>4</sub>N@NCNWs/D composite, again suggesting that the introduction of pyridinic N atoms favors the anchoring of Co<sub>4</sub>N nanoparticles on the NCNWs/D composite [139]. The decrease in the ratio of Co<sup>2+</sup>/Co<sup>3+</sup> confirms that the coordination structure of Co atoms is also possible to be regulated (**Table 5.4**). These results are well in line with our calculation predictions. In addition, the hydroxyl-O content in the Co<sub>4</sub>N@d-NCNWs/D composite remains at 4.1% (**Table 5.5**), indicating the existence of many oxygen-containing functional groups on the surface of the Co<sub>4</sub>N@d-NCNWs/D composite.

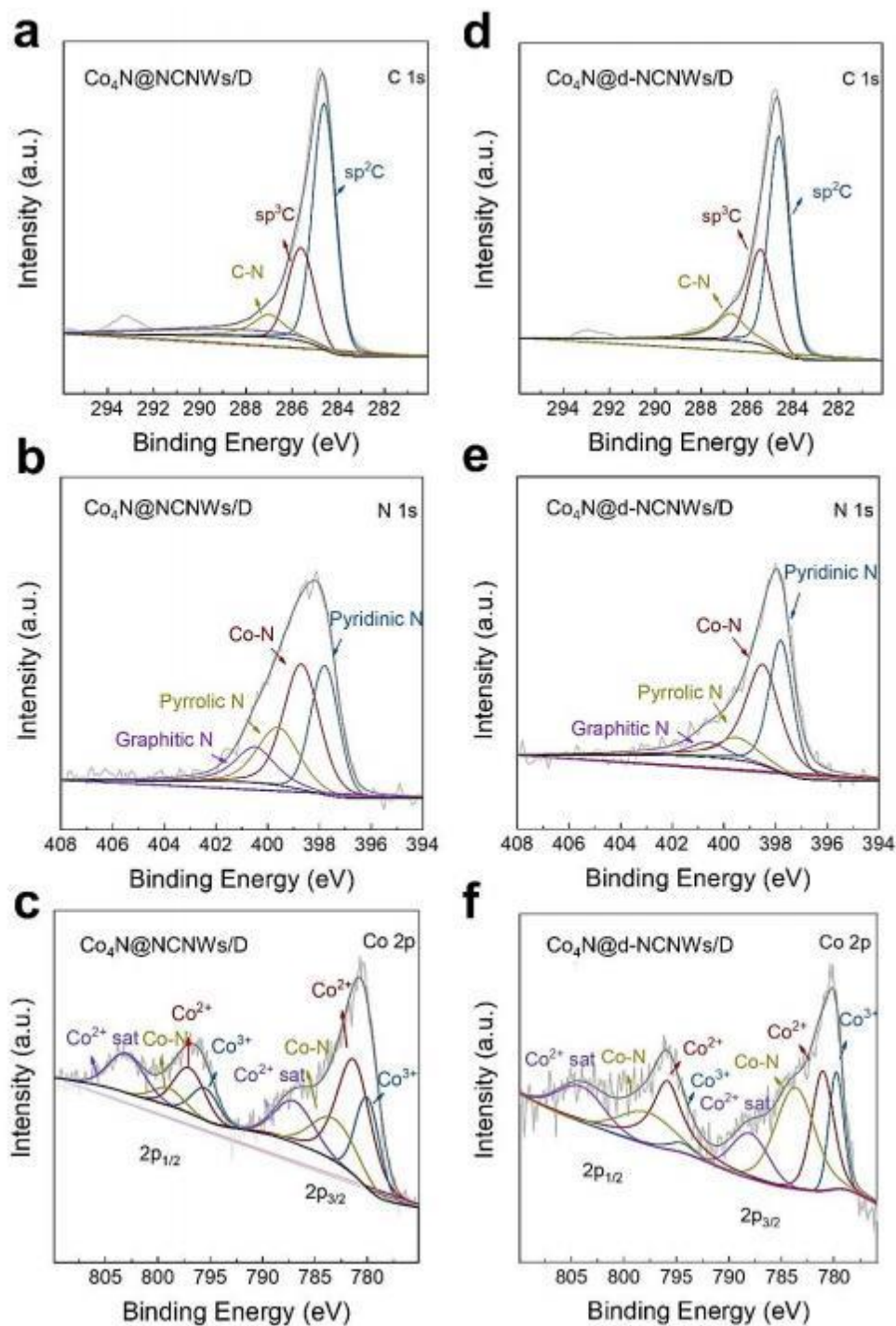


**Figure 5.6.** High-resolution (a) C 1s, (b) N 1s, (c) Co 2p spectra of the Co<sub>4</sub>N@NCNWs/D and (d) C 1s, (e) N 1s, (f) Co 2p spectra of the Co<sub>4</sub>N@d-NCNWs/D composites. The rough lines are experimental results. The smooth lines are fitted ones.

**Table 5.1.** The atomic proportions of the C, N, O, Co elements on the d-NCNWs/D, Co<sub>4</sub>N@NCNWs/D, and Co<sub>4</sub>N@d-NCNWs/D composites, which were estimated from their XPS analysis.

Sample	C	N	O	Co
d-NCNWs/D	86.9%	6.3%	6.8%	0
Co <sub>4</sub> N@NCNWs/D	80.5%	9.0%	7.9%	2.5%
Co <sub>4</sub> N@d-NCNWs/D	80.1%	9.1%	9.3%	2.8%

**Table 5.2.** Distribution of C 1s spectra of the Co<sub>4</sub>N@NCNWs/D and Co<sub>4</sub>N@d-NCNWs/D composites.

Sample	sp <sup>2</sup> -C	sp <sup>3</sup> -C	C-N
Co <sub>4</sub> N@NCNWs/D	62.3%	26.6%	11.0%
Co <sub>4</sub> N@d-NCNWs/D	57.2%	28.9%	13.8%

**Table 5.3.** Distribution of N 1s spectra of the d-NCNWs/D, Co<sub>4</sub>N@NCNWs/D, and Co<sub>4</sub>N@d-NCNWs/D composites.

Sample	Pyridinic-N	Pyrrolic-N	Graphitic N	Co-N
d-NCNWs	65.1%	23.8%	11.1%	0
Co <sub>4</sub> N@NCNWs/D	27.7%	20.8%	13.7%	37.7%
Co <sub>4</sub> N@d-NCNWs/D	35%	12.8%	7.5%	44.7%



**Table 5.4.** Distribution of Co 2p spectra of the Co<sub>4</sub>N@NCNWs/D and Co<sub>4</sub>N@d-NCNWs/D.

Sample	Co <sup>3+</sup>	Co <sup>2+</sup>	Co-N
Co <sub>4</sub> N@NCNWs/D	25.2%	52.9%	21.8%
Co <sub>4</sub> N@d-NCNWs/D	19.2%	32.8%	48.0%

**Table 5.5.** The Content of O 1s distribution spectrum of the Co<sub>4</sub>N@d-NCNWs/D composites.

Sample	Lattice-O	Hydroxyl-O	Adsorbed-O
Co <sub>4</sub> N@d-NCNWs/D	0.9%	4.1%	4.3%

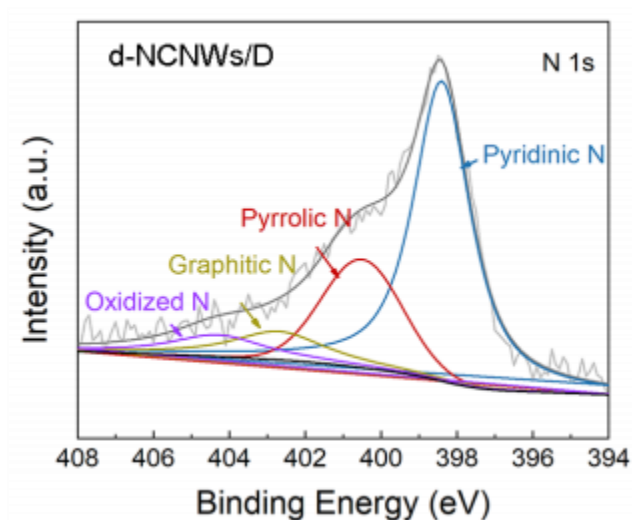


**Figure 5.7.** High-resolution N 1s spectra of d-NCNWs/D composite.

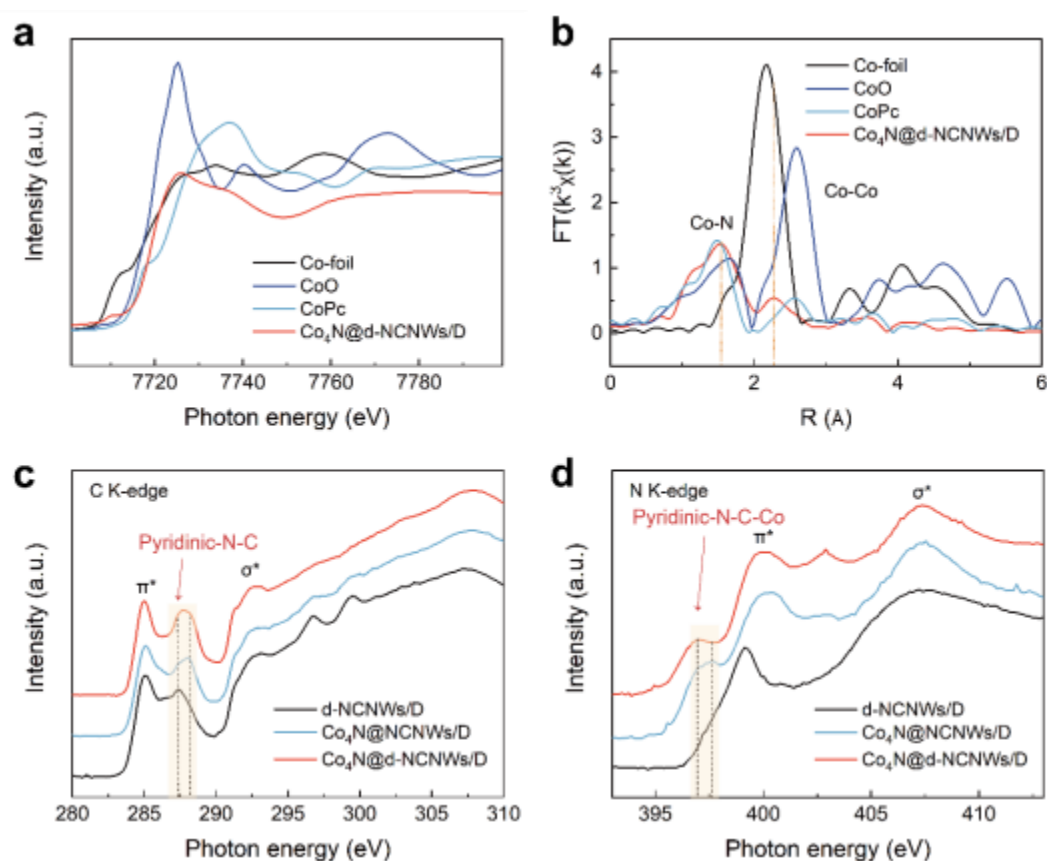


**Figure 5.8.** (a) CoKedgeXANES spectra and (b) Fourier transformsEXAFS spectra for Cofoil, CoO, CoPc and Co<sub>4</sub>N@d-NCNWs, (c) CK-edge and (d) NK-edge XANES spectra of d-NCNWs/D, Co<sub>4</sub>N@NCNWs/D and Co<sub>4</sub>N@d-NCNWs/D composites.

To precisely analyze the local coordination structure of the Co<sub>4</sub>N@d-NCNWs/D composite, X-ray absorption spectroscopy (XAS) was employed. The X-ray adsorption near-edge spectroscopy (XANES) of Co K-edge of the Co<sub>4</sub>N@d-NCNWs/D composite exhibits a different trend compared with the reference Co foil, CoO and cobalt phthalocyanine (CoPc) (**Figure 5.8a**). Fourier transformed (FT)  $k^3$ -weighted extended X-ray absorption fine structure (EXAFS) spectrum was further conducted to investigate the coordination environments of Co atoms. The EXAFS spectra display similar curves to that of the reference of CoPc, indicating that the Co-N bonds could be the main form in the Co<sub>4</sub>N@d-NCNWs/D composite. In addition, compared with Co foil, the Co-Co bond length of the Co<sub>4</sub>N@d-NCNWs/D composite are stretched, while not exceeding that of CoO and CoPc (**Figure 5.8b**). This result provides strong evidence that these N

atoms are incorporated into the Co lattice to form a Co<sub>4</sub>N phase, in good accordance with the TEM and XRD results.

Moreover, the local chemical configurations of the elements C and N are obtained by soft XANES. As shown in **Figure 5.8c**, the C K-edge XANES spectra of the d-NCNWs, Co<sub>4</sub>N@NCNWs/D and Co<sub>4</sub>N@d-NCNWs/D composites display several typical spectroscopic features: a  $1s \rightarrow \pi^*$  transition at about 284.4 eV, a  $1s \rightarrow \sigma^*$  transition occurred at about 291.5 eV. Two weak peaks, which is in the range between  $\pi^*$  and  $\sigma^*$  transition, can be assigned to the C-N bonds. Note that the peak at about 287.4 eV proves a strong pyridinic N-C bonds in the Co<sub>4</sub>N@d-NCNWs/D composite. It is even starkind-NCNWs/D composite, revealing that the electrochemical oxidation pre-treatment will create defect-rich pyridinic-N sites. More importantly, after its anchoring with Co<sub>4</sub>N nanoparticles, the peak at around 397 eV in the NK-edge XANES spectra appears and shifts towards lower energy, confirming that a dominant number of pyridinic-N-C-Co bonds formed in the Co<sub>4</sub>N@d-NCNWs/D composite (**Figure 5.8d**). This result also indicates a starker charge transfer at the interface of the Co<sub>4</sub>N@d-NCNWs/D composite than that of the Co<sub>4</sub>N@NCNWs/D composite.

### 5.3 Electrocatalytic ORR/OER performance

To estimate the catalytic activities of the Co<sub>4</sub>N@d-NCNWs/D composite toward both the OER and ORR, electrochemical measurements were performed using atypical three-electrode system in O<sub>2</sub>-saturated 0.1 M KOH. Among studied electrocatalysts (**Figure 5.9a**), the Co<sub>4</sub>N@d-NCNWs/D composite exhibits the highest ORR activity, namely the most positive onset potential (0.93 V *vs.* RHE) and half-wave potential (0.83 V *vs.* RHE). These values are 0.85 and 0.75 V (*vs.* RHE), 0.87 and 0.78 V (*vs.* RHE), and 0.9 and 0.81 V (*vs.* RHE) for the d-NCNWs/D composite, the Co<sub>4</sub>N film, and the Co<sub>4</sub>N@NCNWs/D composite, respectively. The higher ORR activity of the Co<sub>4</sub>N@d-NCNWs/D composite is quite reasonable since the Co<sub>4</sub>N@d-NCNWs/D composite combines the features of individual components of Co<sub>4</sub>N nanoparticles and the d-

NCNWs/D composite. More importantly, they benefit from the interfacial enhancement accomplished during their electro-oxidation pre-treatment.

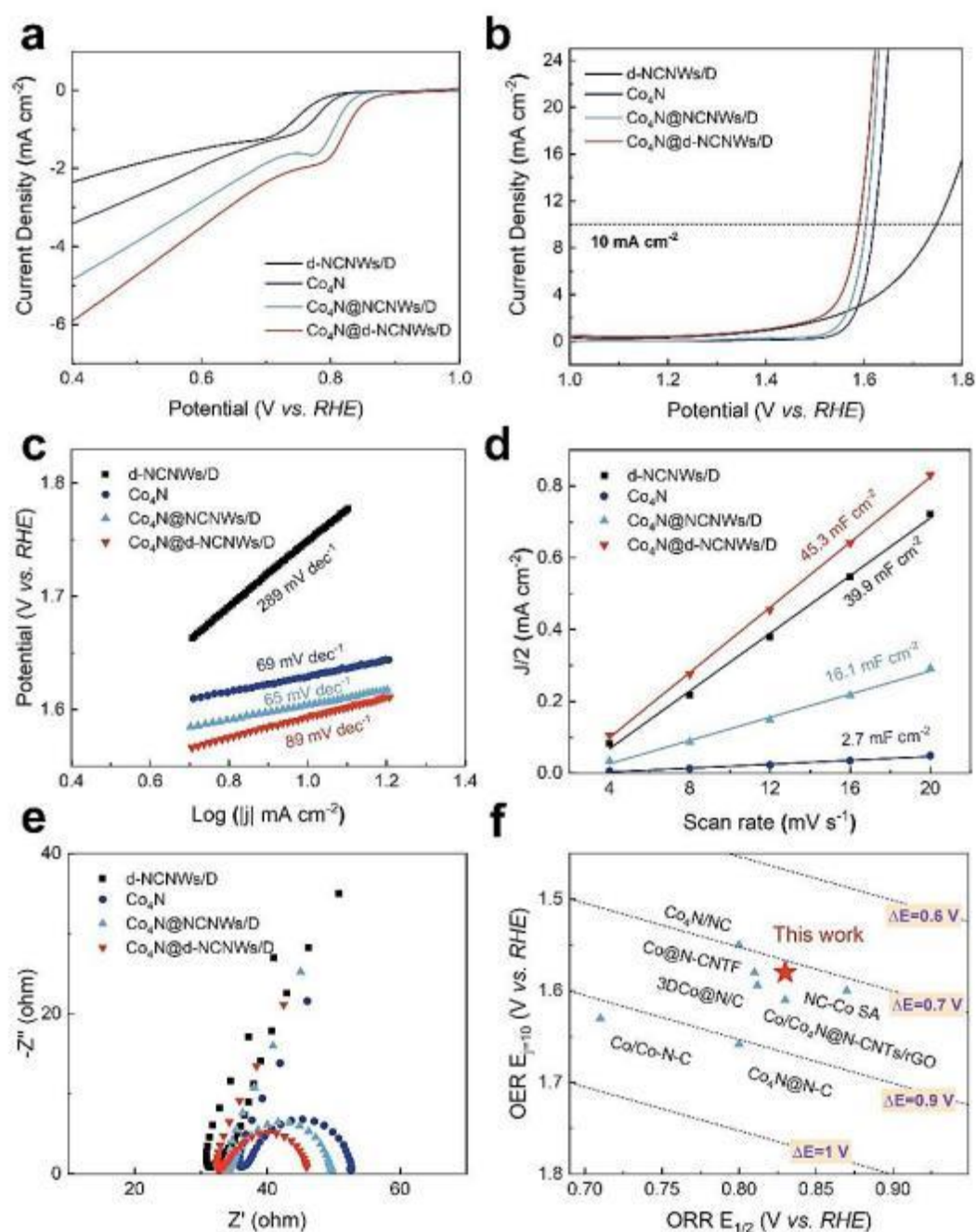


**Figure 5.9.** (a) ORR polarization curves, (b) OER polarization curves in an O<sub>2</sub>-saturated 0.1 M KOH with a scan rate of 2 mV s<sup>-1</sup>, (c) OER Tafel plots, (d) The capacitive current density as a function of scan rate at 1.0 V (vs. RHE), (e) Nyquist plots, (f) Diagram for comparing the potential gap (ΔE) values of Co<sub>4</sub>N@d-NCNW/D films with other reported electrocatalysts.

The OER catalytic performance of the Co<sub>4</sub>N@d-NCNWs/D composite was also assessed in O<sub>2</sub>-saturated 0.1 M KOH and further compared with that of other catalysts. In their OER polarization curves (**Figure 5.9b**), the Co<sub>4</sub>N@d-NCNWs/D composite possesses the lowest OER overpotential. It only requires 340 mV to achieve a current density of 10 mA cm<sup>-2</sup>, much smaller than that of the d-NCNWs/D composite (510 mV), the Co<sub>4</sub>N film (380 mV), and the Co<sub>4</sub>N@NCNWs/D composite (360 mV). The Tafel slope of the Co<sub>4</sub>N@NCNWs/D composite is 65 mV dec<sup>-1</sup> (**Figure 5.9c**), smaller than that of the d-NCNWs/D composite (289 mV dec<sup>-1</sup>) and the Co<sub>4</sub>N film (69 mV dec<sup>-1</sup>). A facilitated OER process thus occurs on the Co<sub>4</sub>N@d-NCNWs/D composite [140].

Electrochemical impedance spectroscopy (EIS) tests were conducted to evaluate the charge transfer rates of the studied catalysts. In their EIS Nyquist plots (**Figure 5.9d**), the Co<sub>4</sub>N@d-NCNWs/D composite displays the smallest semicircle in the high-frequency region with a value of 13 Ω, lower than that of the d-NCNWs/D composite (112 Ω), the Co<sub>4</sub>N film (17 Ω), and the Co<sub>4</sub>N@NCNWs/D composite (16 Ω). This manifests the reduced charge-transfer resistance of the Co<sub>4</sub>N@d-NCNWs/D composite and enhanced electron transfer kinetics at the interface of the electrolyte on the Co<sub>4</sub>N@d-NCNWs/D composite [141]. In addition, the onset position in the low-frequency region responds to the internal resistance of a catalyst. The addition of the d-NCNWs/D composite improves the electrical conductivity of Co<sub>4</sub>N nanoparticles or reduces the internal resistance of Co<sub>4</sub>N nanoparticles from 33.2 Ω to 28.7 Ω. All these results confirm well promoted charge transfer of the Co<sub>4</sub>N@d-NCNWs/D composite, which is induced by the so-named enhanced interfacial effect.

To further explain high performance of the Co<sub>4</sub>N@d-NCNWs composite toward the ORR/OER, its electrochemically active surface area (ECSA) was evaluated *via* the electrochemical double-layer capacitance measurements in a non-faradaic potential region (**Figure 5.10**) [142]. The electrochemical double-layer capacitance (*C<sub>dl</sub>*) of the Co<sub>4</sub>N@d-NCNWs/D composite is 45.3 mF cm<sup>-2</sup>, larger than that of the d-NCNWs/D composite (39.9 mF cm<sup>-2</sup>), the Co<sub>4</sub>N film (2.7 mF cm<sup>-2</sup>) and the Co<sub>4</sub>N@NCNWs/D

composite ( $16.1 \text{ mF cm}^{-2}$ ). The higher  $C_{dl}$  values of both Co<sub>4</sub>N@d-NCNWs/D and d-NCNWs/D composite can be ascribed to the defect-rich surface [143], where many accessible active sites are highly exposed. The Co<sub>4</sub>N@d-NCNWs/D composite thus has excellent bi-functional ORR/OER performance.

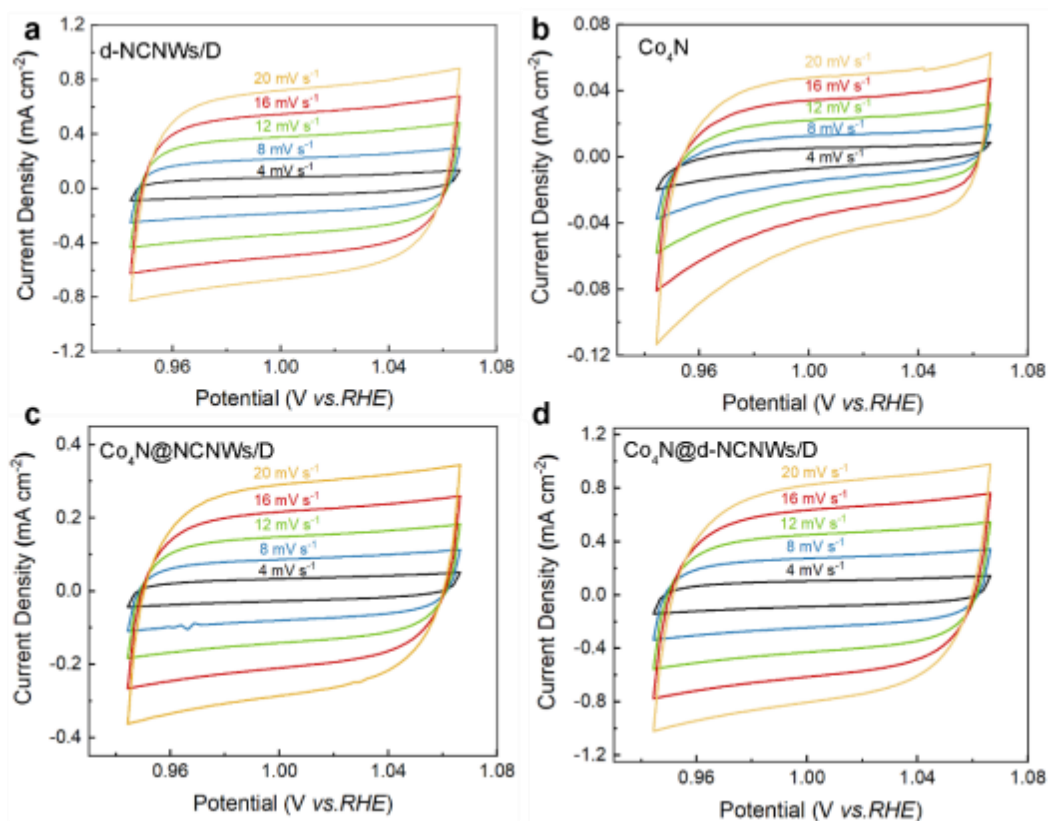


**Figure 5.9.** Cyclic voltammograms of the d-NCNWs/D, Co<sub>4</sub>N, Co<sub>4</sub>N@NCNWs/D and Co<sub>4</sub>N@d-NCNWs/D composites within a potential window from 0.94 to 1.06 V (vs. RHE) at scan rates of 4 - 20  $\text{mV s}^{-1}$ .

In order to evaluate the overall ORR/OER performance of the Co<sub>4</sub>N@d-NCNWs/D composite, the potential difference was calculated between  $E_{j=10}$  for the OER and  $E_{1/2}$  for the ORR. A smaller  $E$  is known to mean better bi-functional activity [7]. The Co<sub>4</sub>N@d-NCNWs/D composite owns a  $\Delta E$  value of 0.75 V (**Figure 5.9f**), smaller than most of the reported Co-N-Cbi-functional ORR/OER electrocatalysts [119, 139, 144-148].

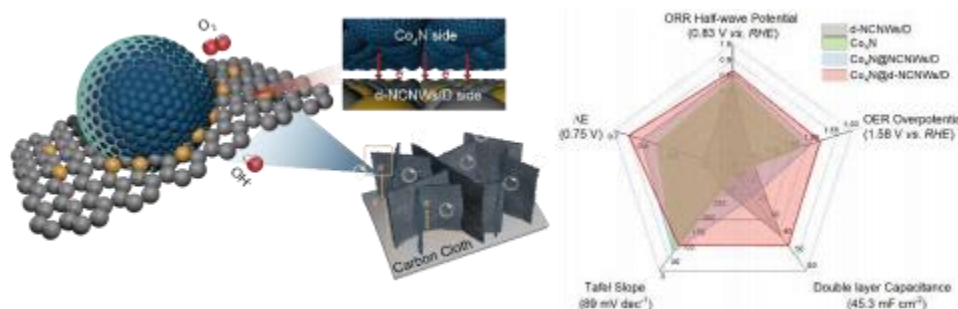


**Figure 5.11.** Schematic illustration of enhanced ORR/OER performance of the Co<sub>4</sub>N@d-NCNWs/D composite (left). Radar plots of the Co<sub>4</sub>N@d-NCNWs/D composite toward the OER and ORR regarding their half-wave potentials, overall potentials,  $\Delta E$ , Tafel slopes, and double layer capacitances.

Based on these DFT calculations and experimental results, we assume (**Figure 5.11**) that the excellent bi-functional activity of the Co<sub>4</sub>N@d-NCNWs/D composite is originated from three aspects. Firstly, many reactants and electrons are fast transferred at the three-phase reaction interface of the Co<sub>4</sub>N@d-NCNWs/D composite, stemming from its large active area and its vertically aligned electron transfer pathways of the d-NCNWs/D composite. Secondly, homogeneously dispersed Co<sub>4</sub>N nanoparticles expose more interfacial Co-pyridinic N-C bonds, improving the density and utilization efficiency of active sites. Thirdly, the heterointerface with pyridinic N atoms promotes the charge transfer from Co<sub>4</sub>N nanoparticles to the d-NCNWs/D composite. In other words, the electronic structures of Co and C atoms are adjusted at the interface, effectively boosting the intrinsic activities of the active sites on the Co<sub>4</sub>N@d-NCNWs/D composite.

Since our strategy of electro-oxidation pre-treatment introduces more pyridinic N atoms into the composite interface, and further improves the bi-functional catalytic activity of such a composite toward the ORR/OER, varied potentials during the electro-oxidation pre-treatment have been applied to check the tunability of this strategy. The catalysts obtained at the potentials of 1.6, 1.8, and 2.0 V are named in this thesis as the

Co<sub>4</sub>N@d-NCNWs/D- 1.6V, the Co<sub>4</sub>N@d-NCNWs/D- 1.8V (previously shorten as Co<sub>4</sub>N@d-NCNWs/D), and the Co<sub>4</sub>N@d-NCNWs/D-2.0V. In the first step, Raman spectroscopy was employed to characterize the phase structures and defect levels of four catalysts (**Figure 5.12**). The appeared six primary peaks are named D band, Gband, D', D+D'', 2D and D+D' band, respectively. All of them are related to CNWs [100]. Other five additional peaks in the range of 100 - 800 cm<sup>-1</sup> are associated with different vibrational modes of the Co-N bond [149, 150]. It is widely accepted that the defect levels in carbon-based materials can be theoretically assessed using the proportion of the intensity of the D band to that of the G band ( $I_D/I_G$ ). The  $I_D/I_G$  values for the Co<sub>4</sub>N@NCNWs/D, the Co<sub>4</sub>N@d-NCNWs/D- 1.6V, Co<sub>4</sub>N@d-NCNWs/D- 1.8V, and the Co<sub>4</sub>N@d-NCNWs/D-2.0V are 0.435, 0.713, 0.993, to 1.163, respectively. The increase of the  $I_D/I_G$  values after electro-oxidation treatment reveals the generation of more defects in the graphite lattice of the d-NCNWs/D. In addition, the strength of the Co-N bond is increased, an indication of the contribution of introduced defects to the anchoring of Co<sub>4</sub>N nanoparticles. Note that the tendency of their ORR activities (e.g., onset potentials) is firstly improved and then becomes worse with an increase of the applied potentials during the electro-oxidation treatment (**Figure 5.13**). That is probably because excessive defects disrupt the conductivity of the Co<sub>4</sub>N@d-NCNWs/D-2.0V. In this context, rational modulation of the coordinate environment of an electrocatalyst is important for its catalyst activities toward different reactions.



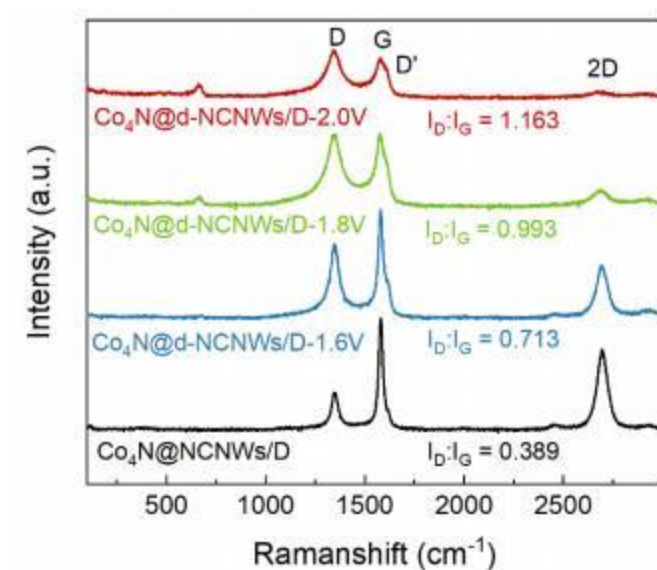


**Figure 5.12.** Raman spectra of Co<sub>4</sub>N@NCNWs/D, Co<sub>4</sub>N@d-NCNWs/D-1.6V, Co<sub>4</sub>N@d-NCNWs/D-1.8V and Co<sub>4</sub>N@d-NCNWs/D-2.0V composites.

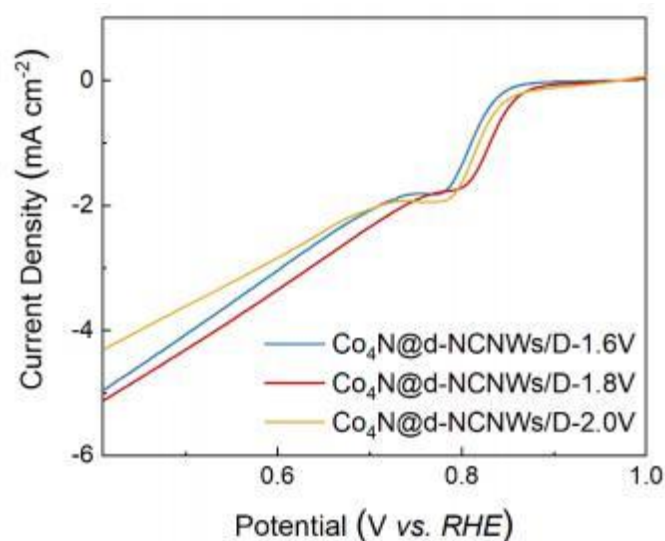


**Figure 5.13.** LSV curves of ORR/OER performance of Co<sub>4</sub>N@d-NCNWs/D-1.6V, Co<sub>4</sub>N@d-NCNWs/D-1.8V and Co<sub>4</sub>N@d-NCNWs/D-2.0V composites.

The charge transfer at the interface of the Co<sub>4</sub>N@d-NCNWs/D composite has been quantified by means of ultraviolet photoelectron spectroscopy (UPS) measurements (**Figure 5.14**). The calculated work functions of the d-NCNWs/D and the Co<sub>4</sub>N@d-

NCNWs/D composites are 6.2 and 5.4 eV, respectively. Electron redistribution thus occurs at the interface of the Co<sub>4</sub>N@d-NCNWs/D composite, owing to the difference in the work functions of the d-NCNWs/D and the Co<sub>4</sub>N@d-NCNWs/D composites [40]. The charge transfers from the Co<sub>4</sub>N phase to the d-NCNWs and eventually reaches equilibrium. Such a statement is also supported by related XPS analysis. In more detail, the XPS peak of pyridinic N (**Figure 5.15a**) shifts to a lower binding energy (namely from 398 eV for the d-NCNWs to 397.5 eV for the Co<sub>4</sub>N@d-NCNWs/D composite), while that of Co 2p (**Figure 5.15b**) shifts to a higher binding energy (namely from 799.8 eV for the Co<sub>4</sub>N to 780.7 eV for the Co<sub>4</sub>N@d-NCNWs/D composite). Some deviations existing between the experimental values and simulation results are probably caused by complex surface states of the Co<sub>4</sub>N@d-NCNWs/D composite, where simulations are still needed to model the actual environment of this catalyst surface.

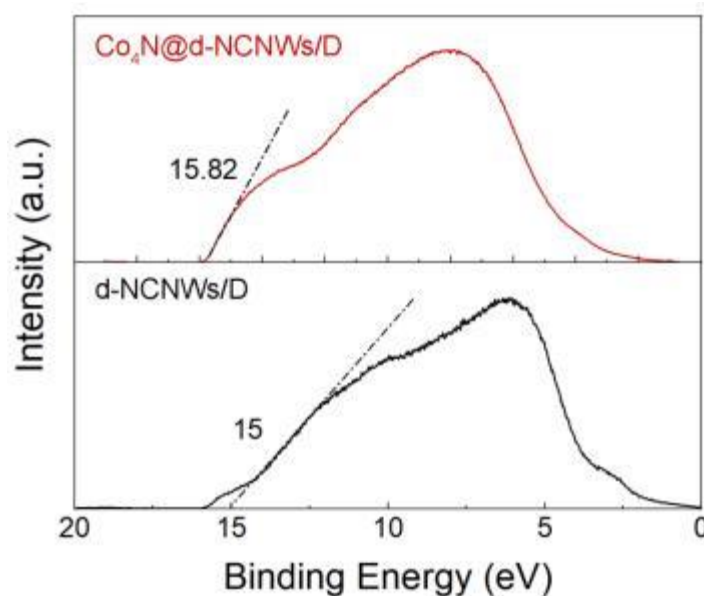


**Figure 5.14.** Ultraviolet photoelectron spectroscopic analysis of the d-NCNWs/D and the Co<sub>4</sub>N@d-NCNWs/D composites.

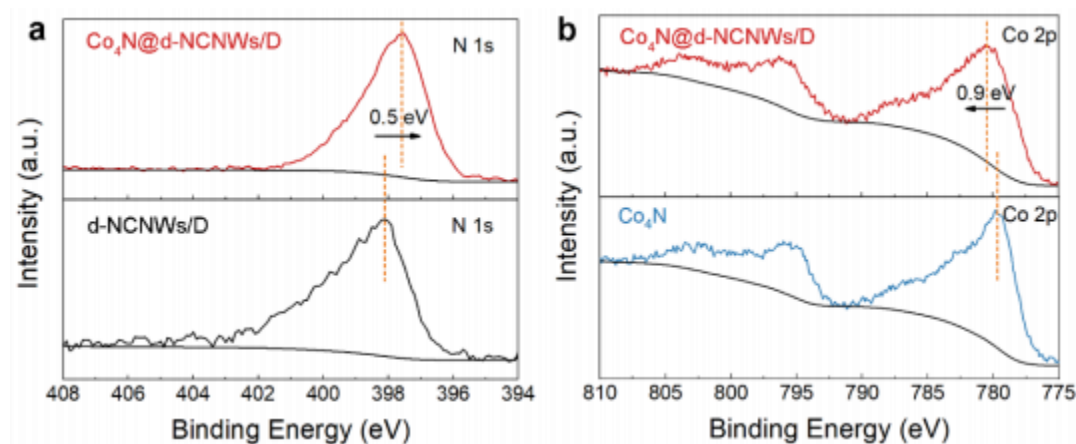


**Figure 5.15.** (a) N 1s XPS spectra of the d-NCNWs/D and the Co<sub>4</sub>N@d-NCNWs/D. (b) Co 2p XPS spectra of the Co<sub>4</sub>N film and the Co<sub>4</sub>N@d-NCNWs/D composites.

#### 5.4 Performance of assembled zinc-air batteries

Based on the superior bi-functional performance of the Co<sub>4</sub>N@d-NCNWs/D composite, a rechargeable aqueous Zn-air battery was assembled with the Co<sub>4</sub>N@d-NCNWs/D composite as the air cathode (**Figure 5.16** and **Figure 5.17a**). As shown in **Figure 5.17b**, the open-circuit potential (OCP) of the Co<sub>4</sub>N@d-NCNWs/D composite constructed Zn-air battery holds 1.385 V, higher than that of Pt/C-RuO<sub>2</sub> based one (1.362 V). The discharge current and maximum power density of Co<sub>4</sub>N@d-NCNWs/D composite based Zn-air battery reach 132 mA cm<sup>-2</sup> and 39.8 mW cm<sup>-2</sup>, respectively. They are higher than those of Pt/C-RuO<sub>2</sub>-based one (80 mA cm<sup>-2</sup> and 24.2 mW cm<sup>-2</sup>), indicating its superior ORR activity (**Figure 5.17c**). Meanwhile, the rate performance of the Co<sub>4</sub>N@d-NCNWs/D composite based Zn-air battery was investigated at a series of current densities. As illustrated in **Figure 5.17d**, the discharge potential remains stable from 2 to 50 mA cm<sup>-2</sup>. Note that the Co<sub>4</sub>N@d-NCNWs/D composite based Zn-air battery retains a high voltage retention of 99.1% at a current density of 2 mA cm<sup>-2</sup>, demonstrating its remarkable reversibility [145].

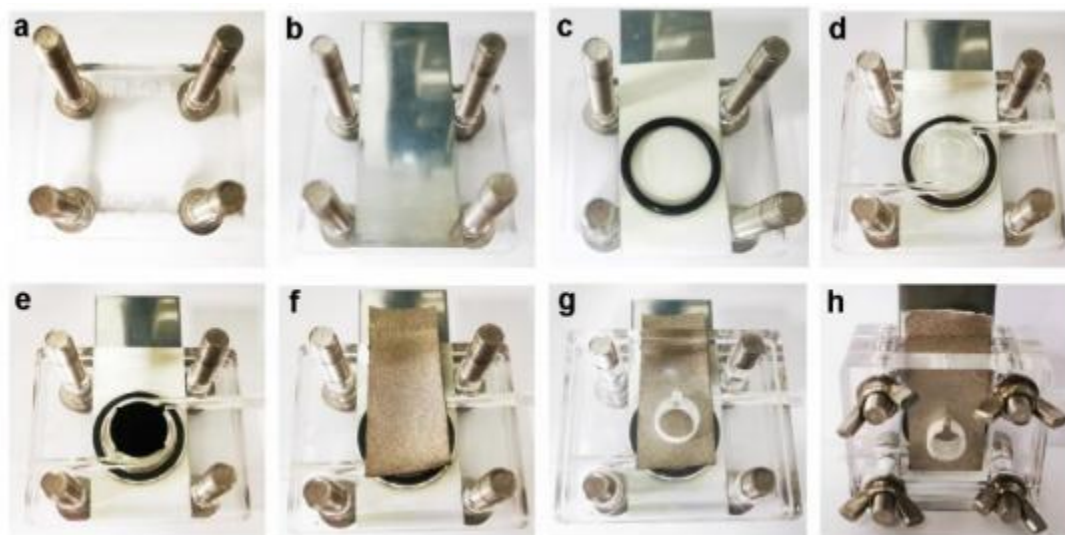


**Figure 5.16.** The assembly procedure of aqueous ZABs with the Co<sub>4</sub>N@d-NCNWs/D composite: (a) Anode plates, (b) Zinc plate with 10.2 g, (c) Anti-dendritic film, (d) Intermediate compartment, (e) As-synthesized Co<sub>4</sub>N@d-NCNWs/D composite, (f) The nickel foam as current collector, (g) Cathode plates, (h) Aqueous ZABs.

It also reveals that the Co<sub>4</sub>N@d-NCNWs/D composite based Zn-air battery exhibits better performance at high currents compared with the Pt/C-RuO<sub>2</sub> based one. Furthermore, the recharge ability of the Co<sub>4</sub>N@d-NCNWs/D composite based Zn-air battery was measured by galvanostatic charging and discharging at a current density of 5 mA cm<sup>-2</sup> (**Figure 5.17e**), revealing an outstanding cycling stability. The Co<sub>4</sub>N@d-NCNWs/D composite based Zn-air battery maintains a smaller voltage gap of 1.02 V and higher energy efficiency of 55% for as long as 130 h, while the Pt/C-RuO<sub>2</sub> based one (voltage gap of 1.13 V and energy efficiency of 52%) suffers from an extremely degradation only after 60 h. Such remarkable performance and stability confirm the structural advantages of the proposed Co<sub>4</sub>N@d-NCNWs/D composite for zinc-air batteries.

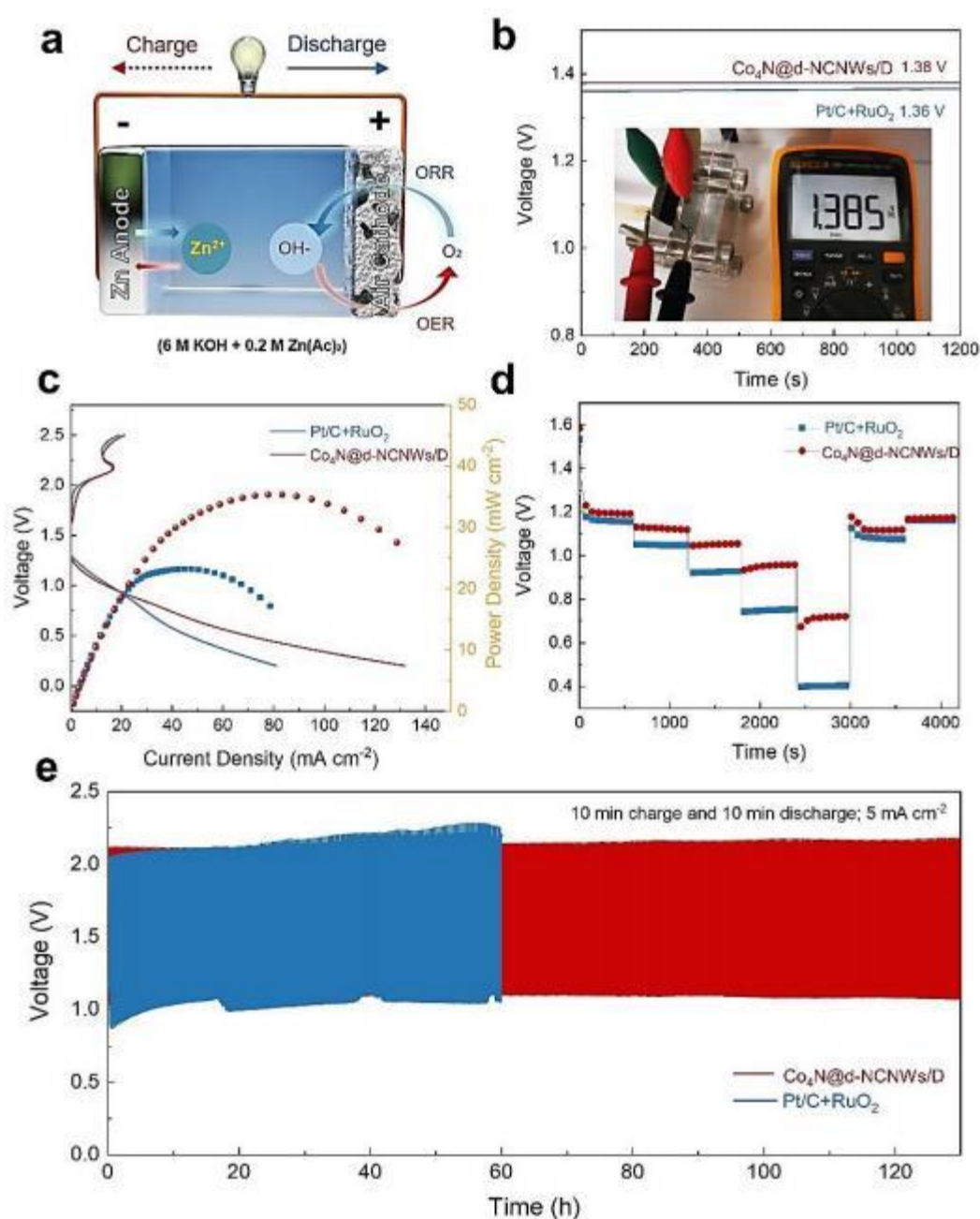


**Figure 5.17.** (a) Schematic configuration of an aqueous rechargeable Zn-air battery, (b) Open-circuit voltage, (c) discharge/charge polarization curves and the corresponding power density, (d) galvanostatic discharge curves at various current densities, (e) galvanostatic discharge curves at a current density of 5 mA cm<sup>-2</sup> of an assembled Zn-air battery with the  $\text{Co}_4\text{N@d-NCNWs/D}$  composite as the air cathode in comparison with the  $\text{Pt/C-RuO}_2$  catalyst.



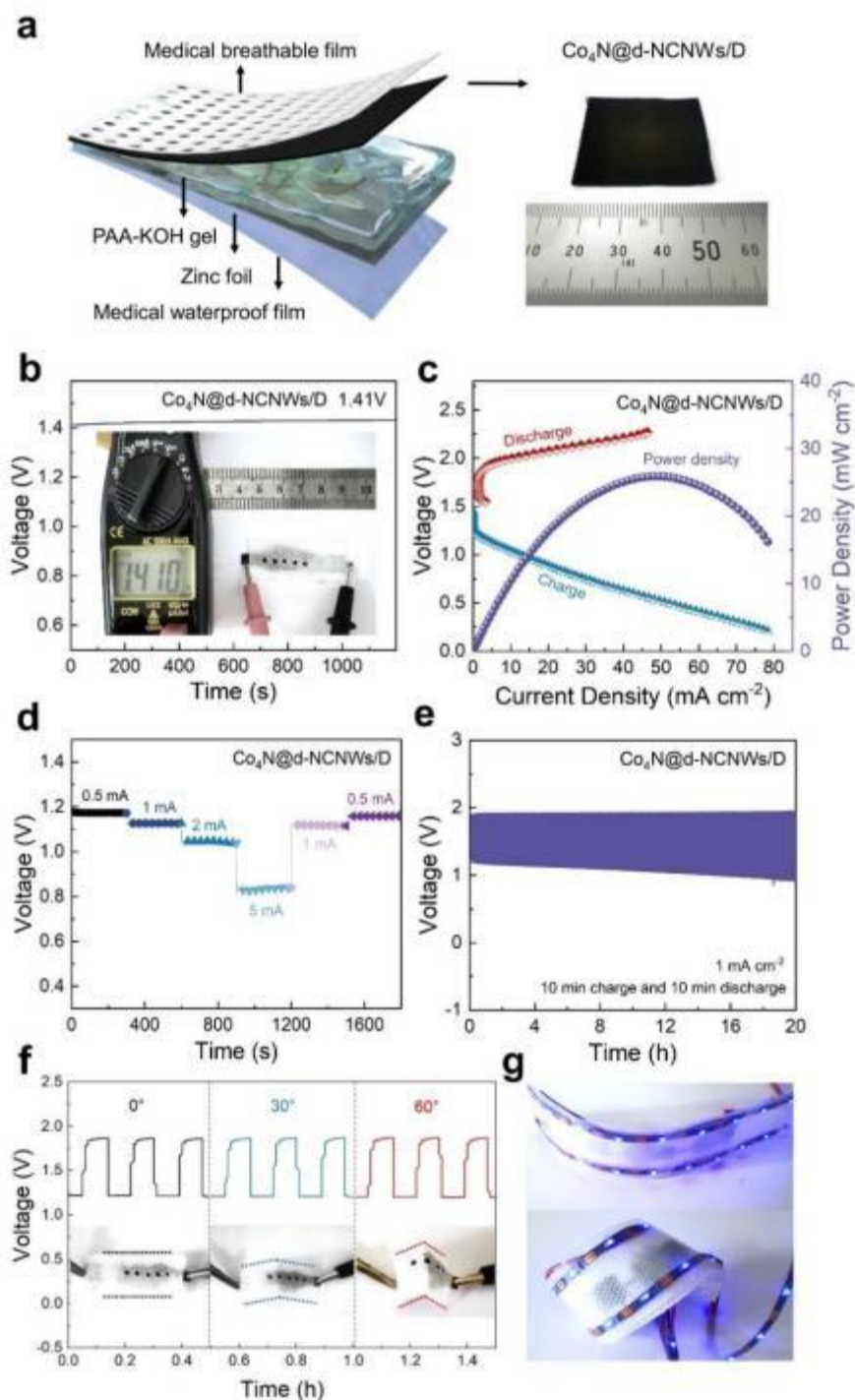


**Figure 5.18.** (a) Schematic configuration of flexible rechargeable Zn-air battery, (b) Open-circuit voltage, (c) Discharge/charge polarization curves (red/blue lines) and the corresponding power density (purple line), (d) Galvanostatic discharge curves at various current densities, (e) Galvanostatic discharge curves at 1 mA cm<sup>-2</sup>, (f) Discharge-charge curves of flexible ZABs under different bending angles, (g, h, i) Photograph images of the LED wristbands.

Finally, based on the superior bi-functional performance, the flexible Zn-air battery with the Co<sub>4</sub>N@d-NCNWs/D composite as the air cathode was assembled to explore the potential utilization in wearable electronics (**Figure 5.18a**). As shown in **Figure 5.18b**, the assemble flexible Zn-air battery exhibits a high open circuit potential (OCP) of 1.41 V. The discharge current and maximum power density of the Co<sub>4</sub>N@d-NCNWs/D composite based Zn-air battery reach 79 mA cm<sup>-2</sup> and 26.5 mW cm<sup>-2</sup>, respectively (**Figure 5.18c**). The discharge curves at various current densities (**Figure 5.18d**) show that such a flexible battery keeps the high voltage retentions of 99.5% at a current density of 1 mAcm<sup>-2</sup>. It exhibits a small voltage gap of 0.6 V at the initial stage and increased to 0.75 V after 20 h, due to the reduced oxygen concentration in the cell (**Figure 5.18e**). In addition, the assembled Zn-air battery maintains a stable voltage plateau under different bending states (**Figure 5.18f**), indicating its superior robustness and flexibility. As displayed in **Figure 5.19**, three flexible Zn-air cells connected in series display an OCP of 4.13 V, slightly lower than the expected value (4.23 V), probably caused by an enlarged internal resistance.

To simulate their practical usage of such a zinc-air battery for flexible devices, three flexible ZABs were connected and integrated as LED wristbands (**Figure 5.18g, h, i**). They work smoothly in both flat and bent states (**Movie 1**). They offer great human safety, thanks to the low toxicity of binder-free electrodes and package materials. All these results illustrate the promising potential of the Co<sub>4</sub>N@d-NCNWs/D composite assembled ZABs in the field of next-generation wearable devices.

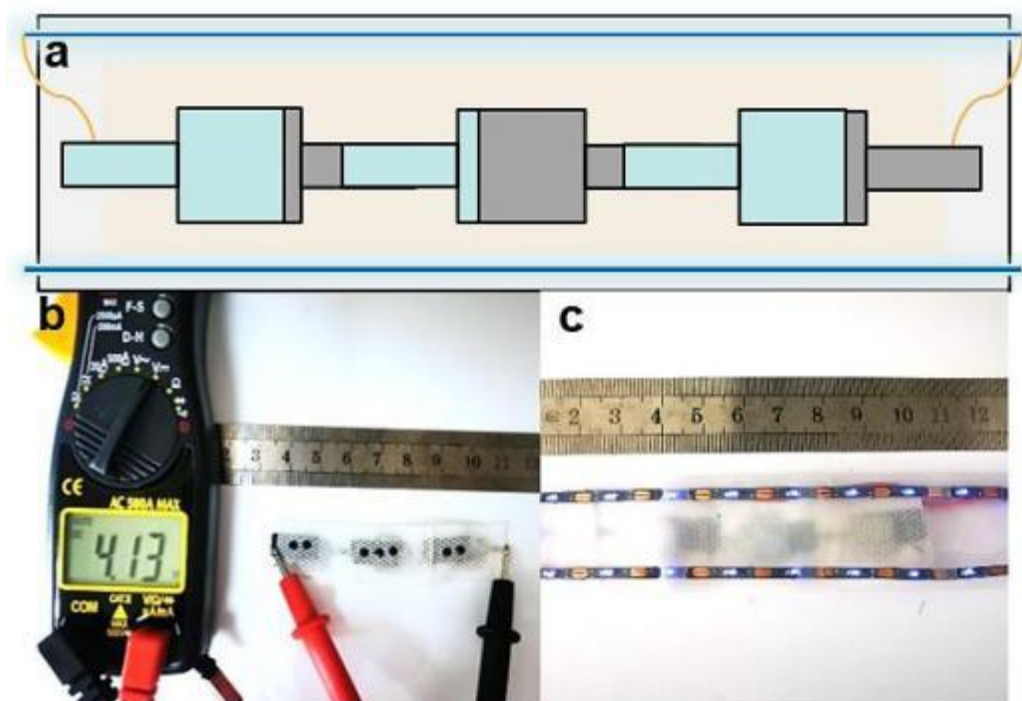


**Figure 5.19.** (a) Illustration of three flexible ZABs cells in series, (b) OCP measurement, (c) Integrated LED wristband assembled with three flexible ZABs in series.

## 5.5 Conclusions

In summary, the DFT calculations have been utilized to guide the design and synthesis of bi-functional electrocatalysts. As a case study, binder-free Co<sub>4</sub>N@d-NCNWs/D composites have been successfully synthesized, where well-dispersed Co<sub>4</sub>N nanoparticles are anchored on the d-NCNWs/D composite *via* post electro-oxidation treatment. Benefiting from the three-dimensional networked structure, an enlarged surface area and enhanced interfacial effect, the Co<sub>4</sub>N@d-NCNWs/D composite exhibits superior catalytic performance toward both the OER and ORR. The intensive electron transfer from Co<sub>4</sub>N nanoparticles to the d-NCNWs/D composite downshifts the *d*-band center of Co and increases the density of states near the Fermi level of C atoms, synergistically reducing the energy barrier of the rate-determining step O\* to OOH\* on the highly active interfacial Co-pyridinic N-C bond and the total reaction overpotentials. As a bind-free and flexible electrode, the Co<sub>4</sub>N@d-NCNWs/D



composites have been employed to assemble flexible Zn-air batteries, demonstrating an outstanding performance with a high OCP and impressive cycling durability under different bending states. This work provides a promising approach for the rational design of highly active ZABs cathodes as well as their applications to assemble zinc air batteries for next-generation wearable and smart electronic devices.

## 6 Cu-np@BDD-m composites for electrocatalytic NITRR

The Cu-based catalysts have been known to be highly active for the NITRR in that Cu is a later transition metal and has a large number of occupied *d*-orbital electrons that can donate electrons. Recently, various Cu-based catalysts (e.g., Cu<sub>50</sub>Ni<sub>50</sub> [151], Cu/Cu<sub>2</sub>O nanowires [152] and Cu-PCTDA [153]) have been synthesized and applied for the electrocatalytic reduction of nitrate into ammonia. In some cases, high selectivity and yield rates of the NITRR were achieved. However, these Cu-based catalysts often suffered from their surface reconstruction during the NITRR, poisoning of their active sites and secondary contamination of water bodies [15, 154], limiting their long-term recycling in the practical devices. Moreover, the performance of the NITRR on these traditional Cu-based catalysts was inhibited by the linear scaling relationship. Therefore, there is an urgent need to propose new strategies to enhance the activity and stability of Cu-based catalysts for the NITRR [155, 156].

Boron-doped diamond (BDD) has long been employed for the NITRR, due to its high electrical conductivity, high resistance to poisoning effect, and wide electrochemical potential window [157-160]. Moreover, the negative hydrogen evolution overpotential ensures its thermodynamic selectivity for the NITRR. Using a BDD as a support, the combination of the efficiency of a Cu-based catalyst with its stability is foreseen. For example, the nitrate removal on a copper-modified BDD electrode was found to be higher than that on a Cu electrode at negative potentials. The ammonia selectivity and stability on a copper-modified BDD was further boosted after its annealing treatment under N<sub>2</sub> atmosphere [161]. However, the chemical inertness of the BDD surface resulted in a poor bonding strength of Cu metal particles on the BDD surface, inhibiting the performance improvement of this copper-modified BDD electrode. In Chapter 5 it has been investigated that the construction of strong metal-supporting interactions allows the homogeneous anchoring of metal nanoparticles and further induces electronic effect at the heterointerface. Such a strategy is expected to further enhance the activity and selectivity of the NITRR.

In this chapter, a new strategy is shown, where Cu nanoparticles are embedded in the BDD-m supports, namely the synthesis of the Cu-np@BDD-m composites. Their morphology, physical and chemical properties are then characterized, followed by the analysis of their NITRR performance. Furthermore, the DFT calculations have been utilized to investigate reaction mechanisms of the NITRR on these Cu-np@BDD-m composites. An implicit solvent model was employed to study the local ion accumulation in the nanoconfined area. This work provides a novel efficient and stable composite catalyst that can be assembled in a sustainable flow cell for the NITRR. It further provides insight into the thermodynamic and kinetic processes involved in the NITRR.

### 6.1 Characterization of Cu-np@BDD-m composites

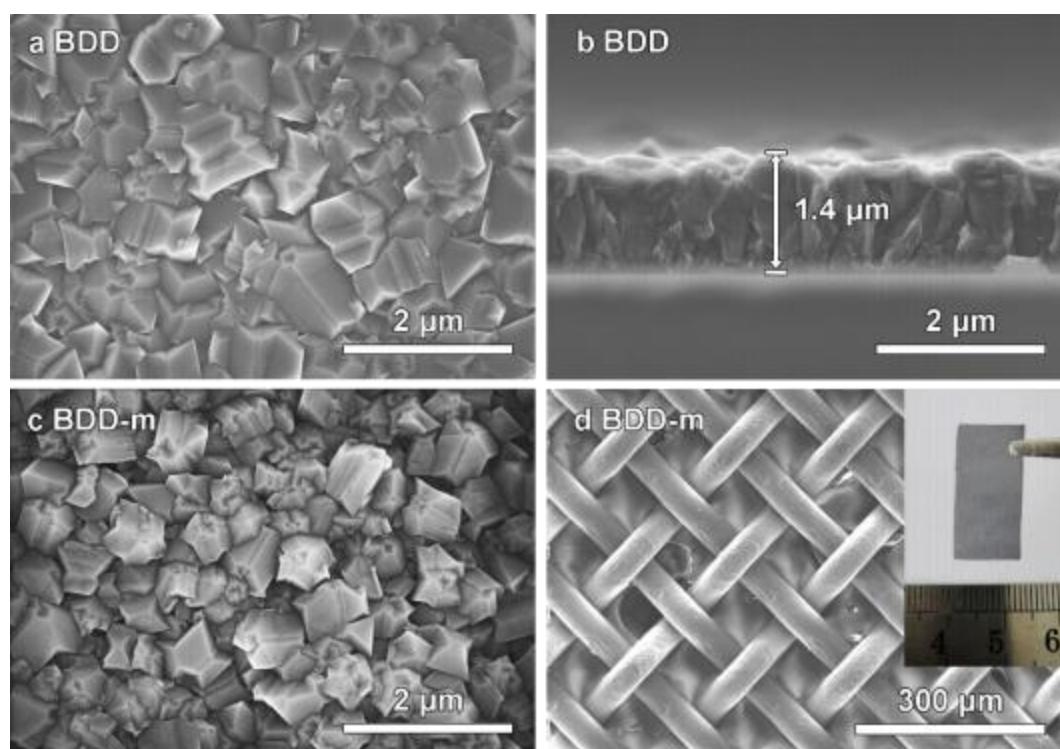


**Figure 6.1.** SEM images of (a) top- and (b) side-view of BDD grown on a silicon wafer, (c) BDD-m grown on copper mesh, (d) BDD-m grown on copper mesh at a low magnification, BDD-m electrode with the size of 1×2 cm (inset).

The synthesis procedure of Cu-np@BDD-m composites is depicted in chapter 3.2.3. In the first step, the BDD-m is deposited on a copper mesh *via* a HFCVD technique. Compared to the BDD grown on a silicon wafer (**Figure 6.1a**), the BDD-m displays a similar micro-crystalline morphology, but with smaller grain size (**Figure 6.1c**). **Figure 6.1d** and its inset show that the BDD-m uniformly covered the copper wires with a diameter of  $\sim 70\ \mu\text{m}$ . Note that the BDD-m film still holds good bendability after deposition.

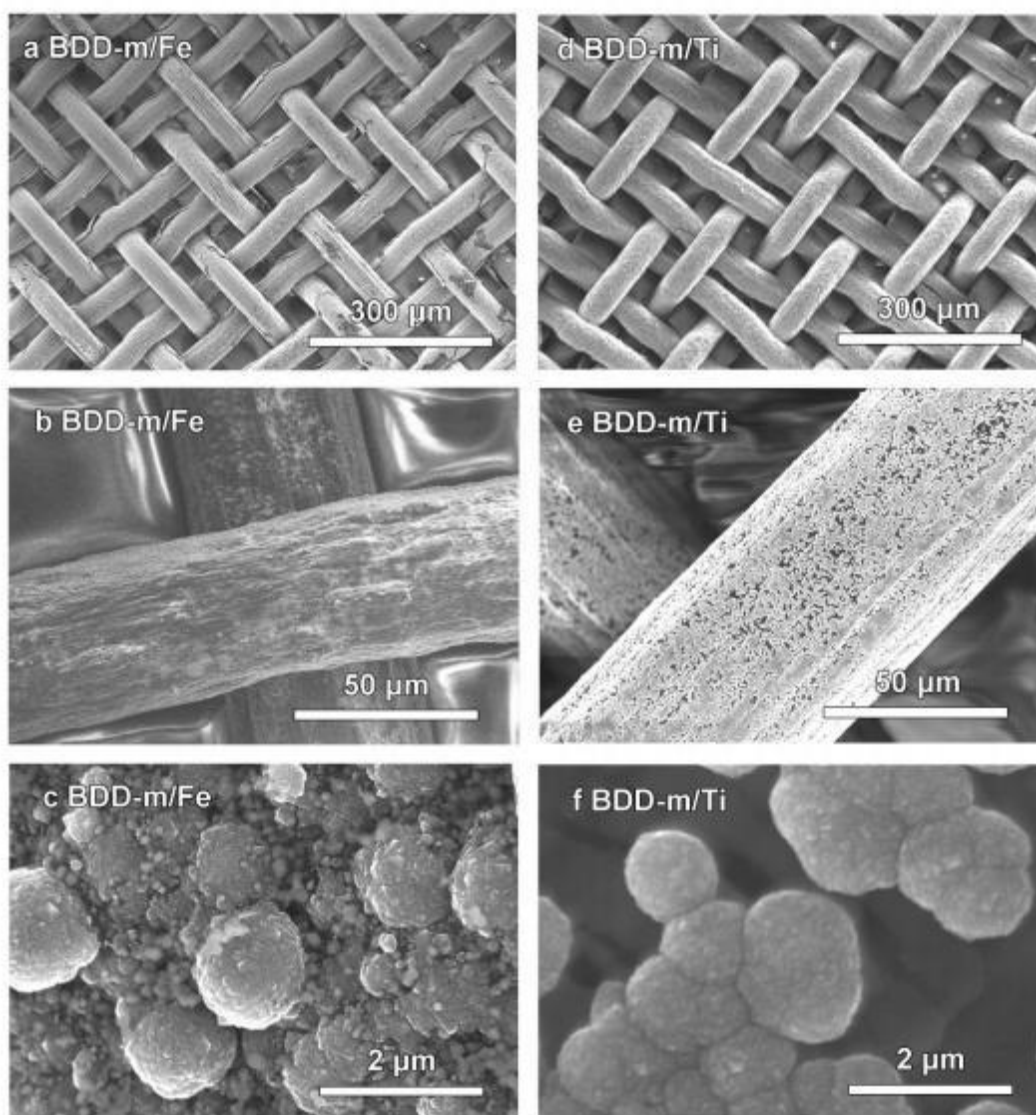


**Figure 6.2.** SEM images of (a,b, c) BDD-m on iron mesh, (d, e,f) BDD-m on titanium mesh.

As control experiments, the BDD-m grown on iron and titanium substrates were prepared using identified parameters. The BDD-m/Fe film shows an irregular thickness. Many obvious cracks are found on its surface (**Figure 6.2a, b**). Notably, a unique profile that huge nanodiamond clusters are surrounded by many graphite spheres appears, indicating that the growth of the diamond phase on strong catalytic substrates (e.g., Fe, Co, Ni) is inhibited. The BDD-m/Ti films, however, exhibit a discontinuous morphology with isolated nanodiamond clusters (**Figure 6.2d,e, f**). Moreover, the film becomes brittle after the BDD deposition, perhaps due to the carbonization of the titanium substrate at high temperatures [162].

Magnetron sputtering was used to deposit a thin Cu layer on the BDD-m (**Figure 6.3a**). The thickness of the Cu layer was estimated to be ~1 nm. After that, the as-prepared Cu@BDD-m composites were annealed in a tube furnace under various conditions. In related SEM images, there are only several Cu nanoparticles with a size of ~100 nm for the Cu-np@BDD-m 600 film, which was annealed at 600 °C under atmospheric pressure (**Figure 6.3b**). The Cu-np@BDD-m 600-vacuum film annealed at a low pressure (~1 Pa) contains more dispersed Cu nanoparticles and their diameters are only of ~20 nm (**Figure 6.3c**). More intriguingly, as the annealing temperature reaches 700 °C, the copper nanoparticles etch through the BDD crystalline grains and create hole channels (**Figure 6.3d**). This is most likely because copper nanoparticles catalyze the conversion of the diamond phase into the graphite phase at a low pressure, resulting in the formation of gas products during the annealing process and thus generating pores structures [163].

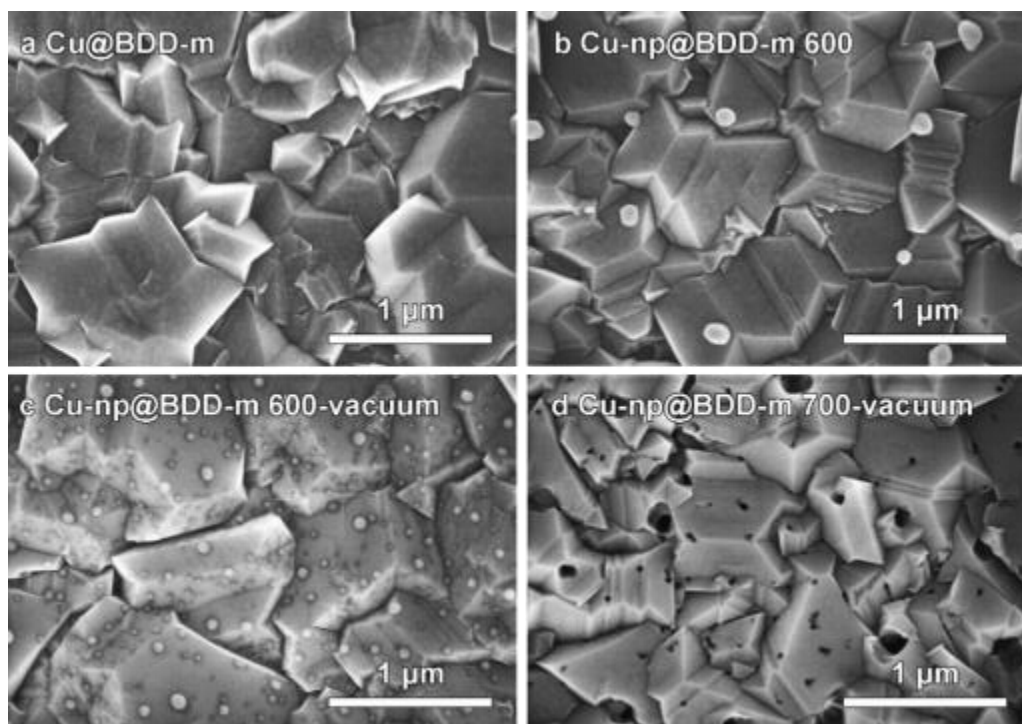


**Figure 6.3.** SEM images of (a) BDD-m on copper mesh with a thin Cu layer, (b) Cu@BDD-m composites after annealing in the atmospheric tube furnace at 600 °C and Cu@BDD-m composites after annealing in the vacuum tube furnace at (c) 600 °C, (d) 700 °C.

Raman spectroscopy was employed to further characterize the phase structures of Cu-np@BDD-m composites (**Figure 6.4**). As a comparison, both the BDD-m and Cu@BDD-m composites were investigated. In their Raman spectra, all three show a broadband at around  $481\text{ cm}^{-1}$  and an obvious asymmetric band at  $1226\text{ cm}^{-1}$ . The latter one is merged with a narrow diamond line at  $1313\text{ cm}^{-1}$ , a typical Fano effect [164]. The presence of these three bands demonstrates the characteristics of a heavily boron-doped diamond [165]. Note that there is a tiny raised band in the Raman spectrum of the Cu-np@BDD-m at  $1606\text{ cm}^{-1}$ , corresponding to the  $\text{sp}^2$  carbon. This confirms our previous assumption that during the etching process a portion of the diamond phase is transformed into graphite.

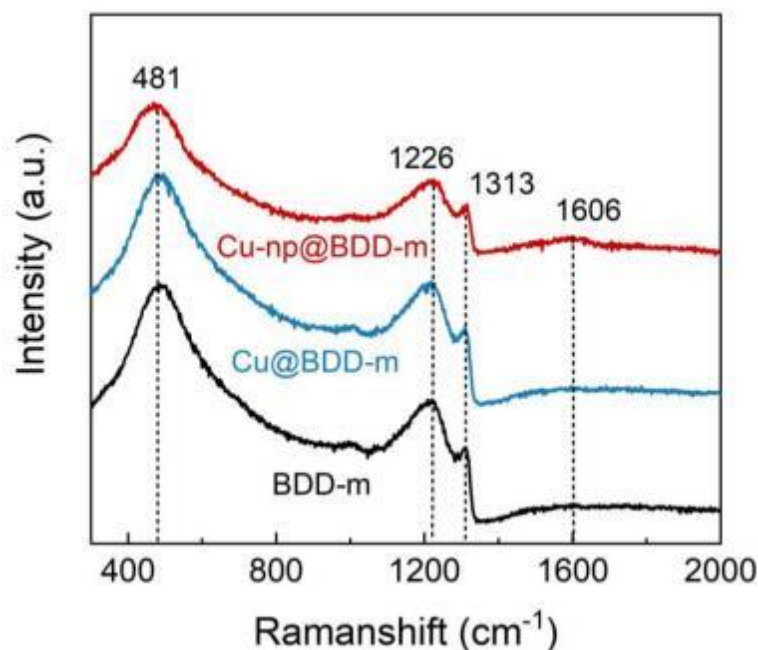


**Figure 6.4.** Raman spectra of BDD-m, Cu@BDD-m and Cu-np@BDD-m composites.

Based on the above experimental results, the presumed etching process is demonstrated in **Figure 6.5**. As the annealing temperature increases, the copper atoms are firstly aggregated and catalyze the conversion of the  $sp^3$ -C to  $sp^2$ -C on the surface layer of BDD-m film. Subsequently, the  $sp^2$ -C phase reacts with the hydrogen atom from Ar/H<sub>2</sub> atmosphere to form hydrocarbons. Their release from the surface leads to continuous etching of the  $sp^3$ -C phase and the creation of various porous. During this process, the formation of the graphite layer is not only necessary for the etching, but also enhances the SMSI between the copper compounds and the BDD-m supports. Well-dispersed copper nanoparticles are achieved by suppressing the Ostwald ripening effect [166]. More interestingly, it is shown in chapter 5.1 that SMSI is expected to induce the charge transfer and adjust the electronic structure of the anchored metal nanoparticles. Therefore, it suggests that this etching process is promising to further affect the activity and selectivity of the NITRR on diamond surface.

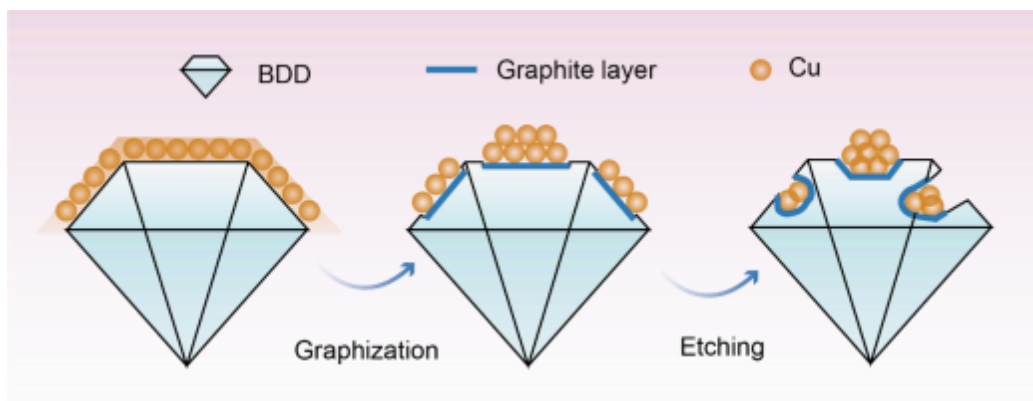


**Figure 6.5.** Illustration of speculative etching process.

## 6.2 Electrocatalytic NITRR performance

To investigate the effect of such a composite on the electrocatalytic activity and kinetics of NITRR, various electrochemical measurements were conducted in 0.5 M  $\text{Na}_2\text{SO}_4$  electrolyte with a three-electrode system of a H-type cell. The LSV curves of the BDD-m, Cu@BDD-m and Cu-np@BDD-m composites were recorded before and after adding of 10 mM  $\text{NaNO}_3$  (**Figure 6.6a**). The difference of the current density indicates the occurrence of reduction reaction of  $\text{NO}_3^-$ . Notably, the Cu-np@BDD-m shows more positive on-set potential (0.1 V vs. RHE) and higher peak current density ( $4.7 \text{ mAcm}^{-2}$ ) than those of Cu@BDD-m (-0.25 V vs. RHE and  $4.1 \text{ mAcm}^{-2}$ ) (**Figure 6.6b**). This potential corresponds to the energy required for the first electron step from the adsorption of  $\text{NO}_3^-$  to  $\text{NO}_3^*$ , which is considered to be a diffusion-controlled process [167]. The obviously positive shift of the on-set potential indicates that the copper nanoparticles in the nanopores or inside the channels contribute to a fast kinetics of  $\text{NO}_3^-$  adsorption. In addition, the absence of on-set potential for the BDD-m film suggests that the adsorption sites of  $\text{NO}_3^-$  is mainly originated from the copper compounds.



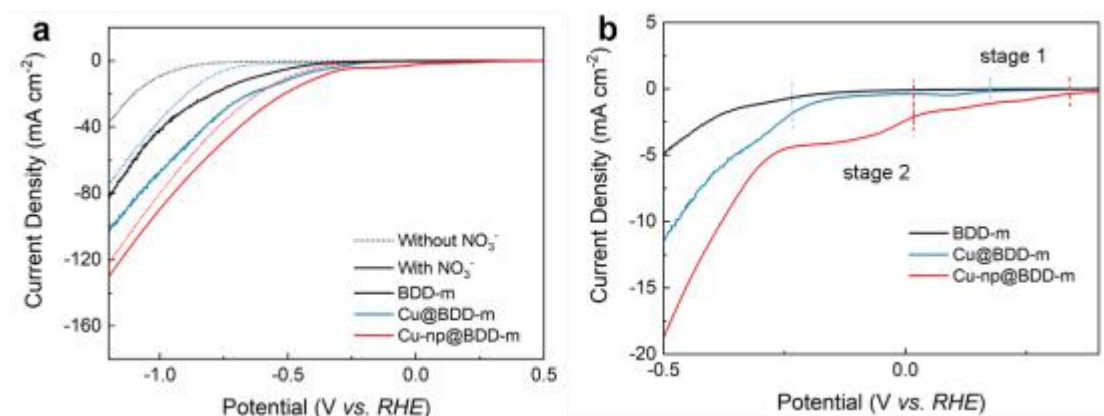


**Figure 6.6.** (a) LSV curves of NITRR performance of BDD-m, Cu@BDD-m and Cu-np@BDD-m composites without and with NO<sub>3</sub><sup>-</sup> at the scan rate of 2 mV/s; (b) On-set potentials of two stages of BDD-m, Cu@BDD-m and Cu-np@BDD-m composites.

The activity and selectivity of the NITRR were further analyzed by products detection after the *i-t* measurements at different potentials for 2 h. For the BDD-m, the conversion rate of NO<sub>3</sub><sup>-</sup> and NH<sub>4</sub><sup>+</sup> is gradually increased while that of NO<sub>2</sub><sup>-</sup> is decreased when the potential is changed from -0.4 to -1 V (vs. RHE) (**Figure 6.7a**). The faradaic efficiency (FE) reaches a maximal value of 37.6% at -1.0 V (vs. RHE) with a NH<sub>3</sub> yield rate of 2.74 mg h<sup>-1</sup> cm<sup>-2</sup> (**Figure 6.7b**). In addition, the reaction rate of nitrate removal slows down with the prolonging of time. The NO<sub>2</sub><sup>-</sup> begins to transform to NH<sub>3</sub> after 30 min, indicating that the NITRR is an eight-electrons step reaction (**Figure 6.7c**) [168]. As a comparison, the Cu@BDD-m composite shows a similar tendency except for the maximal FE of 46.8 % at -0.8 V (vs. RHE) with a NH<sub>3</sub> yield rate of 2.41 mg h<sup>-1</sup> cm<sup>-2</sup> (**Figure 6.7d, e, c**). It reveals that the Cu@BDD-m composite exhibits higher NITRR activity and current utilization efficiency than the BDD-m.

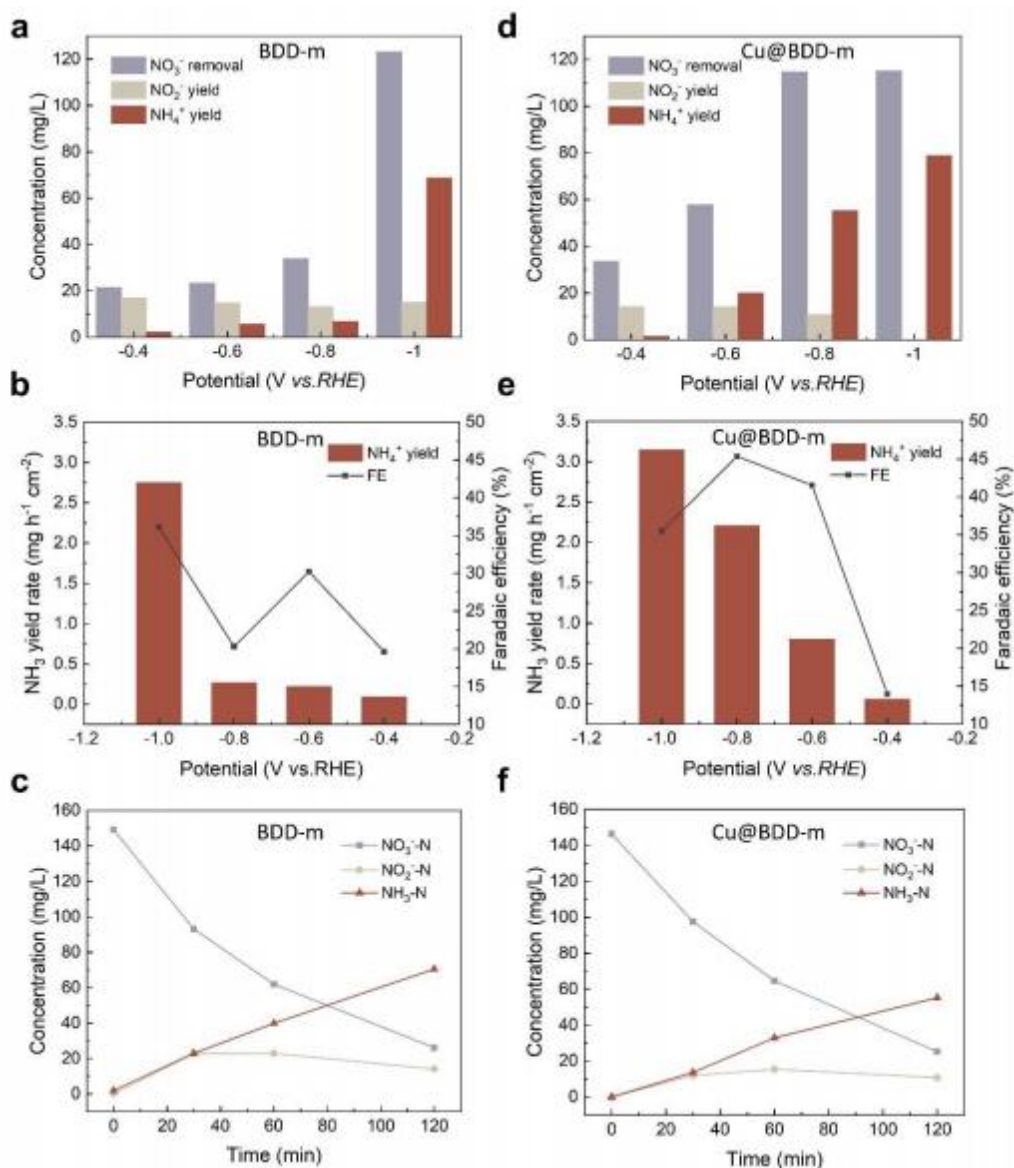


**Figure 6.7.** (a, d)  $\text{NO}_3^-$  removal,  $\text{NO}_2^-$  yield and  $\text{NH}_4^+$  yield rate of (a) BDD-m and (b) Cu@BDD-m composites at different voltages; (b, e)  $\text{NH}_3$  yield rate and FE of (b) BDD-m and (e) Cu@BDD-m composites at different voltages; (d, f) The concentration of  $\text{NO}_3^-$ ,  $\text{NO}_2^-$  and  $\text{NH}_4^+$  of (c) BDD-m and (f) Cu@BDD-m composites with the prolonging of reaction time.

Subsequently, we compared the removal rate of  $\text{NO}_3^-$  and the selectivity of  $\text{NH}_4^+$  for plate BDD, BDD-m, Cu@BDD-m and Cu-np@BDD-m composites (**Figure 6.8a**). The BDD-m shows almost 4 times higher nitrate removal rate (80.2%) than the plate

BDD (21.2 %), which is probably due to the enlarged surface areas and enhanced conductivity of copper mesh. After the combination with Cu nanoparticles, the removal portion of  $\text{NO}_3^-$  is enhanced up to 82.7 % for the Cu@BDD-m composite and 90.2 % for the Cu-np@BDD-m composite, while the selectivity of  $\text{NH}_3$  is increased from 56 % for the BDD-m composite to 61.4 % for the Cu@BDD-m composite, and further increased to 76.8 % for the Cu-np@BDD-m composite. The Cu-np@BDD-m composite exhibits the highest FE of 61.2 % with a  $\text{NH}_3$  yield rate of  $3.5 \text{ mg h}^{-1} \text{ cm}^{-2}$  (Figure 6.8b).

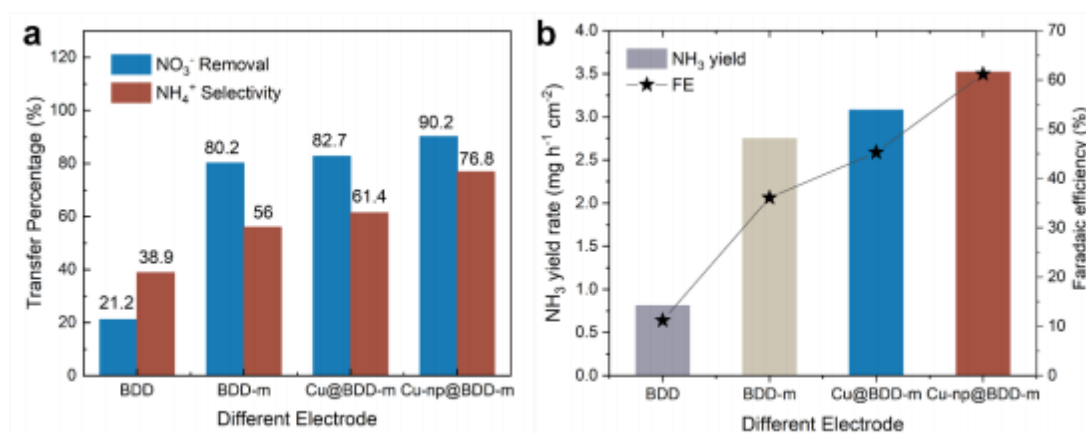


**Figure 6.8.** (a)  $\text{NO}_3^-$  removal and  $\text{NH}_4^+$  selectivity rate, (b)  $\text{NH}_3$  yield and FE of BDD, BDD-m, Cu@BDD-m and Cu-np@BDD-m composites.

### 6.3 DFT calculations of composite interface and NITRR mechanisms

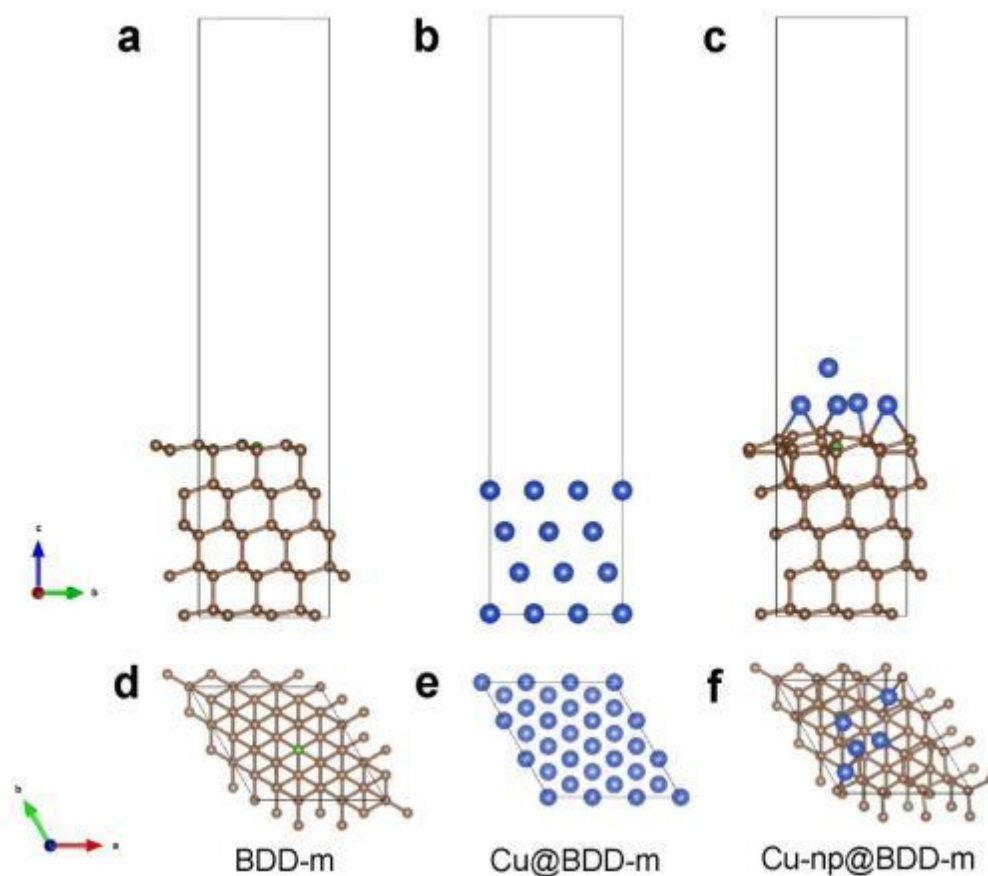


**Figure 6.9.** The constructed models of (a, d) the BDD-m, (b, e) Cu@BDD-m, and (c, f) Cu-np@BDD-m composites in *a* and *c* directions.

Inspired by the boosted activity and selectivity of NITRR on the Cu-np@BDD-m composite, we attempted to seek the relationship between the adsorption of intermediates through the reaction pathways and NITRR performance on different electrodes. Three simplified models were then constructed, corresponding to the BDD-m, Cu@BDD-m and Cu-np@BDD-m composites, respectively (**Figure 6.9**). Three supercells have the same size of  $a = 7.67 \text{ \AA}$ ,  $b = 6.64 \text{ \AA}$ . A vacuum layer of  $30 \text{ \AA}$  in the *c*-direction was setup for the further surface adsorption of intermediates. Note that for the Cu-np@BDD-m composites, only five copper atoms were constructed to highlight the interactions between the BDD-m substrate and the copper nanoparticles. This simplification is necessary to reduce the consumption of computational resources.

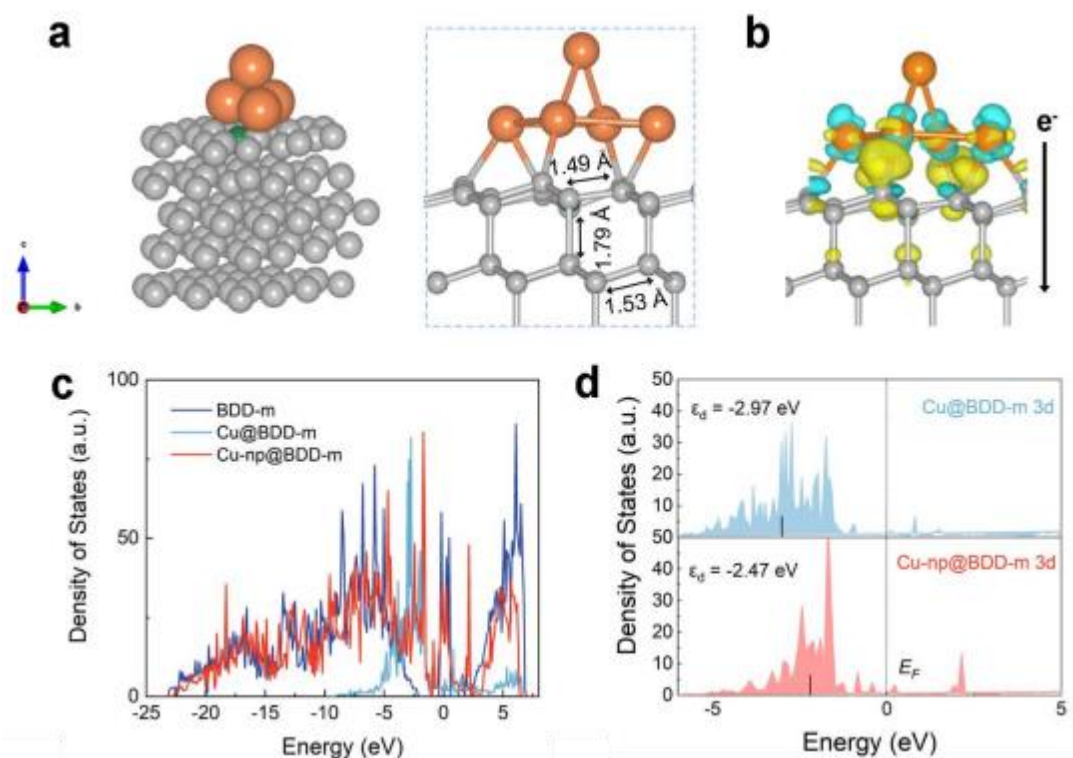


**Figure 6.10.** (a) The optimized structure of Cu-np@BDD-m; (b) Charge transfer at the interface between the BDD-m substrate and Cu nanoparticles; (c) Density of states (DOS) of the BDD-m, Cu@BDD-m and Cu-np@BDD-m composites; (d) D-band center of Cu atoms of Cu@BDD-m and Cu-np@BDD-m composites.

After the structure optimization of the Cu-np@BDD-m composite, the carbon atoms in the first two layers of the BDD surface were found to be reorganized, due to the adding of Cu atoms. The length of C-C bonds in the first layer is reduced from 1.53 to 1.47 Å, while that of the second layer is increased from 1.53 to 1.79 Å (**Figure 6.10**). The configuration is converted from the orthotetrahedron of  $sp^3C$  to the planar six-membered ring of  $sp^2C$ , confirming the assumption that copper nanoparticles are thermodynamically favorable for promoting graphitization of the diamond phase. Further Bader charge analysis and calculation of electron density of state show that the charge transfer is induced from the copper atoms to the BDD-m substrate (**Figure 6.10b**). The DOS near the fermi level reduced and the d-band center of Cu 3d orbital up shifts from -2.97 to -2.47 eV (**Figure 6.10c, d**). This tendency is reversed comparing

with the calculations that were conducted in Chapter 5.1, probably because the different number of electrons filled in d orbitals of Cu and Co.

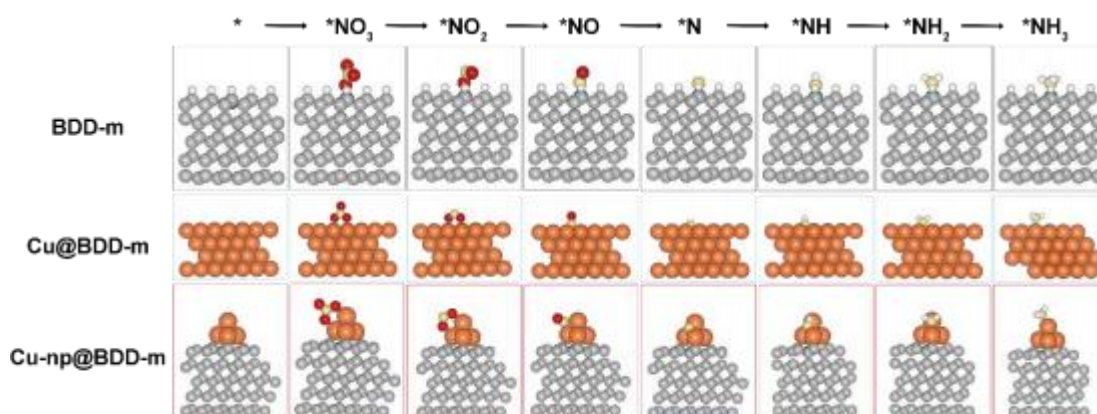


**Figure 6.11.** Reaction pathways on BDD-m, Cu@BDD-m and Cu-np@BDD-m composites.

The speculated reaction pathway of NITRR on BDD-m, Cu@BDD-m and Cu-np@BDD-m composites are listed as:  $\text{NO}_3^- \rightarrow * \text{NO}_3 \rightarrow * \text{NO}_2 \rightarrow * \text{NO} \rightarrow * \text{N} \rightarrow * \text{NH} \rightarrow * \text{NH}_2 \rightarrow * \text{NH}_3 \rightarrow \text{NH}_3(\text{g})$ , which is reported with the minimize energy barrier (**Figure 6.11**) [168, 169]. Note that the adsorption site on BDD-m is boron atom, while that on Cu@BDD-m and Cu-np@BDD-m is parallel Cu sites. All adsorption sites are calibrated to the minimum value, ensuring the accuracy of subsequent energy calculations of each step.

To analyze the effect of the tunable electronic structure of Cu-np@BDD-m composite on the performance of NITRR, the adsorption energy of intermediates along the NITRR and HER reaction pathways in different pH value was calculated. As shown in **Figure 6.12a**, the adsorption energies of  $* \text{NO}_3$ ,  $* \text{NO}_2$  and  $\text{N}^*$  intermediates are increased significantly on the Cu-np@BDD-m composite, allowing the total reaction to be thermodynamically favorable.



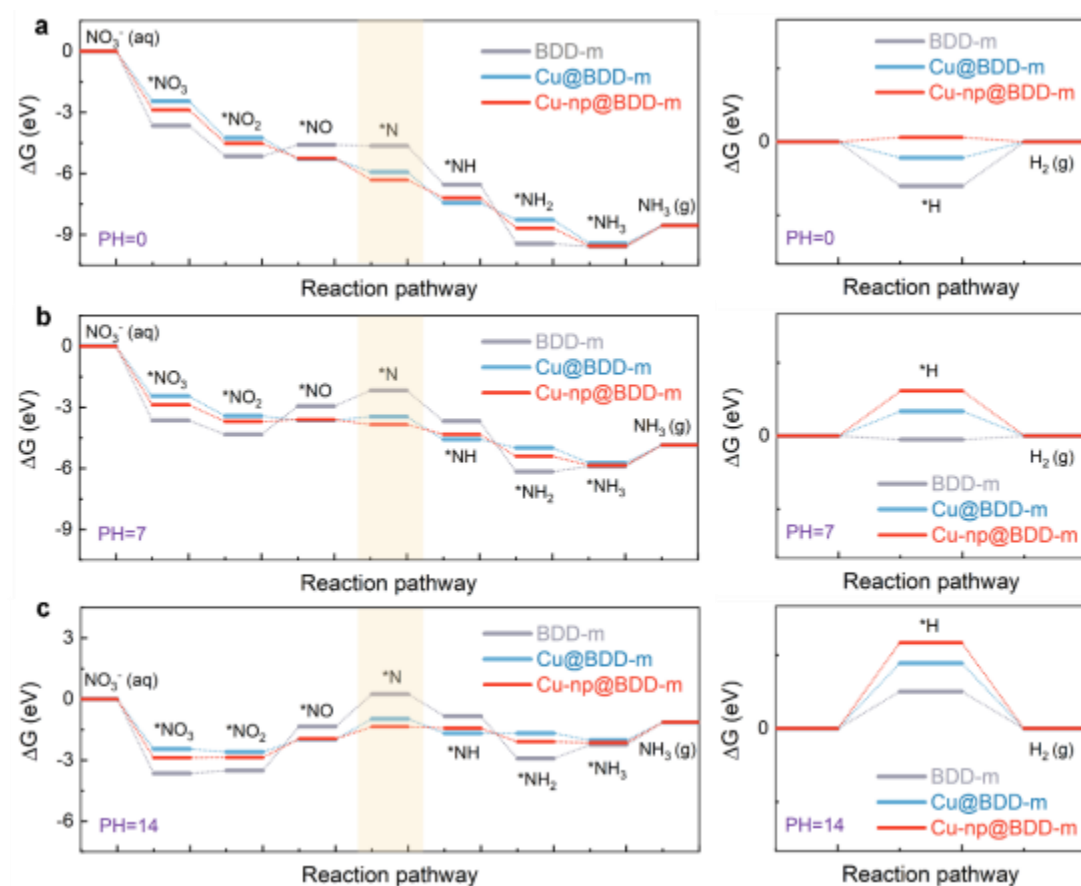


**Figure 6.12.** (a) Gibbs energy diagram along the NITRR reaction pathways of BDD-m, Cu@BDD-m and Cu-np@BDD-m composites; (b) Configurations with intermediate adsorption for each step on the Cu-np@BDD-m composite.

However, the energy barrier of HER (0.12 eV) at pH=0 is much lower than that of NITRR (1.43 eV) (**Figure 6.12b**), extremely reducing the current efficiency of NITRR. In the neutral environment (pH=7), the energy barrier of HER is up to 0.97 eV, surpassing that of NITRR (0.90 eV) on Cu-np@BDD-m composites, leads to the improved NITRR performance by inhibiting the HER (**Figure 6.12c, d**). In the contrary, the energy barrier of HER on Cu@BDD-m composites is 0.50 eV but the reaction energy of NITRR is 1.09 eV. Although the energy barrier of HER in an alkaline environment (pH=14) on all samples is larger than that of NITRR, the selectivity of ammonia is limited by low concentration of  $^*\text{H}$  (**Figure 6.12e, f**). Hence, it can be speculated that the interaction between the BDD-m and Cu nanoparticles reduce the

energy barrier of NITRR and increase that of HER, enhancing the reaction selectivity. In addition, it has been found that the angles and adsorption sites of the intermediate molecules switch during the NITRR reactions. Therefore, it is necessary to correct these Gibbs energies in the real solution environment in the next studies.

#### 6.4 Ion accumulation in the nanoconfined area

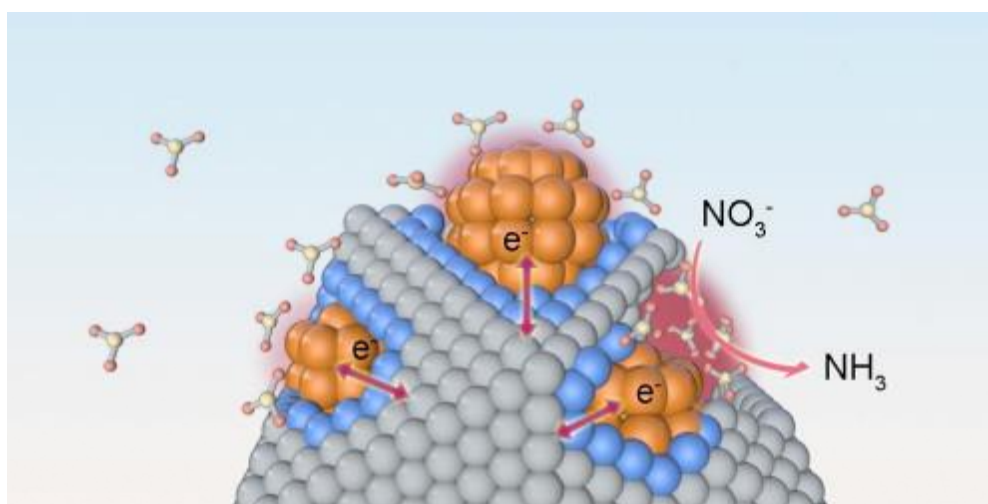


**Figure 6.13.** Illustration of NITRR reaction mechanisms in the nanoconfined area.

As discussed in chapter 6.3, the interaction between the BDD-m substrate and copper nanoparticles can modulate the electronic structure of each component, eventually adjusting the reaction pathways of NITRR and HER. More interestingly, our electrochemical LSV tests demonstrate that the first step of NITRR, namely the adsorption of  $\text{NO}_3^-$ , is controlled by diffusion kinetics and extremely enhanced on the Cu-np@BDD-m composite. We attempted to attribute this to the local accumulation of ions in a nano-confined area (**Figure 6.13**) [170], a new approach to break the linear scaling relationship of catalyst design concept. Therefore, an implicit model is employed to investigate the adsorption kinetics of  $\text{NO}_3^-$  ions on the Cu-np@BDD-m composite (**Figure 6.14**). The electrolyte layer consists of 0.5 M  $\text{Na}_2\text{SO}_4$ , 10 mM  $\text{NaNO}_3$  and water. Note that the negative ions, especially  $\text{NO}_3^-$ , are accumulated in the nearest solution layer on the Cu-np@BDD-m composites, while  $\text{Na}^+$  ions are repelled



at the far distance (**Figure 6.14a**). A local enrichment region of nitrate is formed around the copper atoms at the interface (**Figure 6.14b**). The increased number of adsorbed  $\text{NO}_3^-$  ions of Cu-np@BDD-m composites near the Cu atoms suggest the local accumulation effect in the nanoconfined area (**Figure 6.14c**). This effect is expected to significantly increase the concentration of reactant and accelerate the conversion rate, thereby serving as a guideline for the structural design of other catalytic reactions controlled by diffusion adsorption (e.g., NRR and  $\text{CO}_2\text{RR}$ ).

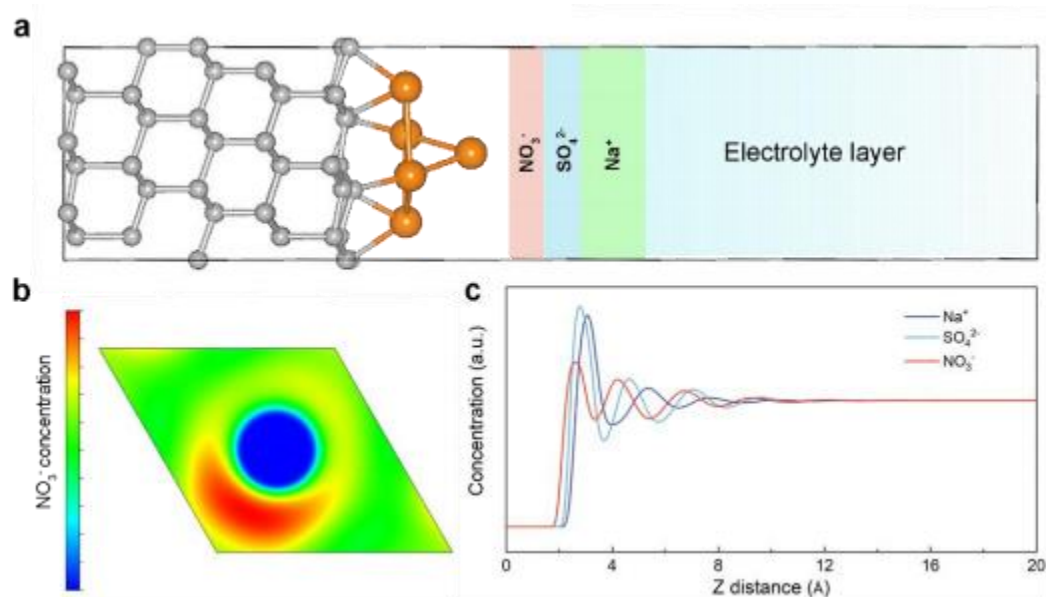


**Figure 6.14.** 3D-rism calculation of  $\text{NO}_3^-$  ion adsorption on Cu-np@BDD-m composite: (a) The simulated electrolyte layer above on Cu-np@BDD-m composite, (b) The local accumulation of  $\text{NO}_3^-$  ions, (c) The distribution of  $\text{NO}_3^-$  concentration along the distance of Cu-np@BDD-m composite.

## 6.5 Conclusions

In summary, the Cu-np@BDD-m composite was synthesized by the combination of HFCVD with magnetron sputtering, where Cu nanoparticles etched the BDD-m substrate *via* post annealing treatment in a low-pressure tube furnace. Such a composite exhibits superior NITRR performance (e.g., high nitrate transformation ratio of 90.2% and ammonia selectivity of 76.8%). The DFT calculations elaborate that the SMSI

between BDD-m substrate and Cu nanoparticles induces the charge transfer from Cu-np to BDD-m, upshifts the d-band center of Cu 3d orbitals from -2.97 to -2.47 eV and enhanced adsorption energy of the N-contained intermediates along the reaction pathways, thus reducing the reaction energy of NITRR from 1.09 to 0.91 eV and increasing the energy barrier of HER from 0.50 to 0.97 eV. Furthermore, the unique pore structure formed by the etching effect shows ions local accumulation effect in the nanoconfined areas, boosting the kinetics of nitrate adsorption. Consequently, this work offers insight into the thermodynamic and kinetic mechanisms of NITRR and provides the guidance to design efficient and stable catalytic electrode for sustainable electrosynthesis.

## 7 Summary and outlook

### 7.1 Summary

In this thesis, the DFT calculations have been combined with different experimental tool with an aim to design three diamond-based composites. They have been synthesized by various techniques such as MPCVD and HFCVD, etc.) and further employed for electrocatalysis of small molecules - oxygen and nitrate.

In the first part of this thesis, the N-CNWs/D composites have been deposited by means of the MPCVD technique. The morphology structures and compositions were modulated by varying the deposition parameters of methanol concentration and nitrogen flux. After annealing post-treatment, the composites exhibited enhanced ORR performance (e.g., the  $E_{\text{onset}}$  increased from 0.73 to 0.835 V vs. RHE) and excellent stability (e.g., 90% current retention after a 20 h electrolysis time). The boosted performance was found to mainly result from the optimized surface property, exposed active pyridinic-N edge sites and the bonding nanodiamond layer of such composites.

In the second part of this thesis, highly dispersed  $\text{Co}_4\text{N}$  nanoparticles were further anchored on the d-NCNWs/D composite in order to enhance the metal-supporting interactions. The DFT calculations predict that this SMSI induces the charge transfer at the heterointerface from Co to C, downshifting the d-band center of Co 3d orbitals from -2.15 to -2.21 eV. The adsorption energy of intermediates through the ORR/OER reaction pathways is thus balanced, leading to the overpotential reduced from 0.67 to 0.23 eV. An electrooxidation pretreatment was exploited to build the  $\text{Co}_4\text{N}@d\text{-NCNWs/D}$  composite with superior ORR/OER bi-functional performance (e.g., a small potential gap of 0.75 V). Moreover, the composite was assembled as an air cathode into the flexible zinc-air batteries, of which open circuit was as high as 1.41 V and bendable stability was excellent.

In the third part of this thesis, a composite of BDD-m and Cu nanoparticles was used for the NITRR. The BDD-m supporting was directly prepared on a copper mesh

*via* the HFCVD, followed by depositing a thin copper film by magnetron sputtering. Copper nanoparticles were found to be embedded in the BDD-m by annealing under a low pressure. This composite featured superior NITRR performance (e.g., nitrate removal of 90.2% and ammonia selectivity of 76.8%) and a positive onset potential at 0.1 V (*vs.* RHE), indicating the fast kinetic of the first step. The DFT calculations confirmed that the enhanced interactions after etching improved the selectivity in thermodynamic process, namely reduced the reaction energy of NITRR from 1.09 to 0.90 eV. It also raised the energy barrier of HER from 0.50 up to 0.92 eV, generating a “trapping” nanoconfined area where the local accumulation of nitrate ions in the kinetic process was enhanced. This effect breaks the linear scaling principles and achieves efficient energy conversion.

The importance of the work in this thesis lies on two aspects. Firstly, the balance of the activity and stability of a catalyst can be achieved by designing its morphology structure, composition and heterointerface interactions. Secondly, the combination of the DFT calculation with experimental results are useful and efficient and to discuss the effect of SMSI on the electrocatalytic performance of a catalyst, especially for the inert diamond-based supports. It is important for the future screening of highly efficient diamond-based heterogeneous catalysts.

## 7.2 Outlook

Based on the achievements shown in this thesis, future activities can be further conducted in the following research areas:

(1) According to the results of ammonia synthesis demonstrated in chapter 6, the addition of a second reactant will be promising for the synthesis of more high value products (e.g., urea). Design of a flow reactor including product collection might extend the practical applications of diamond-based composites in the electrocatalysis of small molecules.

(2) Dynamic characterization of the microenvironment in the heterointerface

region shall be investigated by use of *in-situ* spectroscopy (e.g., *in-situ* Raman, *in-situ* DFT-IR, etc.). Deeply insight into the dynamics of the catalytic reactions of small molecules is desired.

(3) The combination of the DFT calculations further with machine learning is expected to screen highly efficient diamond composites for specific catalytic reactions, based on strong metal-support interactions inside the designed catalysts.

(4) The substrate materials need to be designed with controlled shape and porosity. Diamond composites can be prepared to construct self-supporting gas diffusion electrodes.

(5) All these concepts, strategies, and materials are expected to be workable for electrocatalysis of other small molecules such as  $\text{N}_2$  and  $\text{CO}_2$ .

## 8 References

- [1] J. J. Weijia Zhou, Jia Lu, Linjing Yang, Dongman Hou, Guoqiang Li, Shaowei Chen, Recent developments of carbon-based electrocatalysts for hydrogen evolution reaction, *Nano Energy*, 28, (2016), 29-43.
- [2] Q. S. Gao, W. B. Zhang, Z. P. Shi, L. C. Yang and Y. Tang, Structural Design and Electronic Modulation of Transition-Metal-Carbide Electrocatalysts toward Efficient Hydrogen Evolution, *Advanced Materials*, 31, (2019), 1802880.
- [3] H. Jin, B. Ruqia, Y. Park, H. J. Kim, H. S. Oh, S. I. Choi and K. Lee, Nanocatalyst Design for Long-Term Operation of Proton/Anion Exchange Membrane Water Electrolysis, *Advanced Energy Materials*, (2020), 2003188.
- [4] J. G. Chen, R. M. Crooks, L. C. Seefeldt, K. L. Bren, R. M. Bullock, M. Y. Darensbourg, P. L. Holland, B. Hoffman, M. J. Janik, A. K. Jones, M. G. Kanatzidis, P. King, K. M. Lancaster, S. V. Lymar, P. Pfromm, W. F. Schneider and R. R. Schrock, Beyond fossil fuel-driven nitrogen transformations, *Science*, 360, (2018), eaar6611.
- [5] P. H. van Langevelde, I. Katsounaros and M. T. M. Koper, Electrocatalytic nitrate reduction for sustainable ammonia production, *Joule*, 5, (2021), 290-294.
- [6] C. Yang, Y. Zhu, J. Liu, Y. Qin, H. Wang, H. Liu, Y. Chen, Z. Zhang and W. Hu, Defect engineering for electrochemical nitrogen reduction reaction to ammonia, *Nano Energy*, 77, (2020), 105126.
- [7] Z.-F. Huang, J. Wang, Y. Peng, C.-Y. Jung, A. Fisher and X. Wang, Design of Efficient Bifunctional Oxygen Reduction/Evolution Electrocatalyst: Recent Advances and Perspectives, *Advanced Energy Materials*, 7, (2017),
- [8] L. Yang, J. Shui, L. Du, Y. Shao, J. Liu, L. Dai and Z. Hu, Carbon-based metal-free ORR electrocatalysts for fuel cells: past, present, and future, *Advanced Materials*, 31, (2019), e1804799.
- [9] X. X. Wang, M. T. Swihart and G. Wu, Achievements, challenges and perspectives on cathode catalysts in proton exchange membrane fuel cells for transportation, *Nature Catalysis*, 2, (2019), 578-589.
- [10] D. B. Liu, K. Ni, J. L. Ye, J. Xie, Y. W. Zhu and L. Song, Tailoring the structure of carbon nanomaterials toward high-end energy applications, *Advanced Materials*, 30, (2018), 1802104.
- [11] Y. Zhang, L. Tao, C. Xie, D. Wang, Y. Zou, R. Chen, Y. Wang, C. Jia and S. Wang, Defect engineering on electrode materials for rechargeable batteries, *Advanced Materials*, 32, (2020), e1905923.
- [12] W. Zhou, L. Xie, J. Gao, R. Nazari, H. Zhao, X. Meng, F. Sun, G. Zhao and J. Ma, Selective H<sub>2</sub>O<sub>2</sub> electrosynthesis by O-doped and transition-metal-O-doped carbon cathodes via O<sub>2</sub> electroreduction: A critical review, *Chemical Engineering Journal*, 410, (2021), 128368.
- [13] H. Yang, X. Han, A. I. Douka, L. Huang, L. Gong, C. Xia, H. S. Park and B. Y. Xia, Advanced oxygen electrocatalysis in energy conversion and storage, *Advanced Functional Materials*, (2020), 2007602.

- [14] Y. Ren, C. Yu, X. Tan, H. Huang, Q. Wei and J. Qiu, Strategies to suppress hydrogen evolution for highly selective electrocatalytic nitrogen reduction: challenges and perspectives, *Energy & Environmental Science*, 14, (2021), 1176-1193.
- [15] H. Xu, Y. Ma, J. Chen, W. X. Zhang and J. Yang, Electrocatalytic reduction of nitrate - a step towards a sustainable nitrogen cycle, *Chem Soc Rev*, 51, (2022), 2710-2758.
- [16] Y. Zeng, C. Priest, G. Wang and G. Wu, Restoring the nitrogen cycle by electrochemical reduction of nitrate: progress and prospects, *Small Methods*, 4, (2020), 2000672.
- [17] K. Muzyka, J. R. Sun, T. H. Fereja, Y. X. Lan, W. Zhang and G. B. Xu, Boron-doped diamond: current progress and challenges in view of electroanalytical applications, *Analytical Methods*, 11, (2019), 397-414.
- [18] Y. He, H. Lin, Z. Guo, W. Zhang, H. Li and W. Huang, Recent developments and advances in boron-doped diamond electrodes for electrochemical oxidation of organic pollutants, *Separation and Purification Technology*, 212, (2019), 802-821.
- [19] R. Trouillon and D. O'Hare, Comparison of glassy carbon and boron doped diamond electrodes: Resistance to biofouling, *Electrochimica Acta*, 55, (2010), 6586-6595.
- [20] A. Manzo-Robledo, C. Lévy-Clément and N. Alonso-Vante, The interplay between hydrogen evolution reaction and nitrate reduction on boron-doped diamond in aqueous solution: the effect of alkali cations, *Electrochimica Acta*, 117, (2014), 420-425.
- [21] S. C. B. Oliveira and A. M. Oliveira-Brett, Voltammetric and electrochemical impedance spectroscopy characterization of a cathodic and anodic pre-treated boron doped diamond electrode, *Electrochimica Acta*, 55, (2010), 4599-4605.
- [22] I. Y. Hideo Notsu, Tetsu Tatsuma, Donald A Tryk, Akira Fujishima, Surface carbonyl groups on oxidized diamond electrodes, *Journal of Electroanalytical Chemistry*, 492, (2000), 31-37.
- [23] D. A. T. Tata N. Rao, K. Hashimoto, and A. Fujishima, Band-Edge Movements of Semiconducting Diamond in Aqueous Electrolyte Induced by Anodic Surface Treatment, *Journal of The Electrochemical Society*, 146, (1999), 680-684.
- [24] P. Canizares, J. Lobato, R. Paz, M. Rodrigo and C. Saez, Electrochemical oxidation of phenolic wastes with boron-doped diamond anodes, *Water Research*, 39, (2005), 2687-2703.
- [25] P. A. M. M. Panizza, G. Cerisola, Ch Comninellis, Electrochemical treatment of wastewaters containing organic pollutants on boron-doped diamond electrodes: Prediction of specific energy consumption and required electrode area, *Electrochemistry Communications*, 3, (2001), 336-339.
- [26] S. Garcia-Segura, E. V. dos Santos and C. A. Martinez-Huitle, Role of sp(3)/sp(2) ratio on the electrocatalytic properties of boron-doped diamond electrodes: A mini review, *Electrochemistry Communications*, 59, (2015), 52-55.

- [27] H. Kato, J. Hees, R. Hoffmann, M. Wolfer, N. Yang, S. Yamasaki and C. E. Nebel, Diamond foam electrodes for electrochemical applications, *Electrochemistry Communications*, 33, (2013), 88-91.
- [28] N. Suo, H. Huang, A. M. Wu, G. Z. Cao, X. D. Hou and G. F. Zhang, Porous boron doped diamonds as metal-free catalysts for the oxygen reduction reaction in alkaline solution, *Applied Surface Science*, 439, (2018), 329-335.
- [29] B. Liu, Y. Zheng, H. Q. Peng, B. Ji, Y. Yang, Y. Tang, C. S. Lee and W. Zhang, Nanostructured and boron-doped diamond as an electrocatalyst for nitrogen fixation, *ACS Energy Letters*, 5, (2020), 2590-2596.
- [30] S. Wang, X. Ji, Y. Ao and J. Yu, Vertically aligned N-doped diamond/graphite hybrid nanosheets epitaxially grown on B-doped diamond films as electrocatalysts for oxygen reduction reaction in an alkaline medium, *ACS Appl Mater Interfaces*, 10, (2018), 29866-29875.
- [31] M. Jiang, Z. Zhang, C. Chen, W. Ma, S. Han, X. Li, S. Lu and X. Hu, High efficient oxygen reduced reaction electrodes by constructing vertical graphene sheets on separated papillary granules formed nanocrystalline diamond films, *Carbon*, 168, (2020), 536-545.
- [32] T. V. Hung, R. Karunagaran, T. T. Tung, N. N. Dang, S. X. Nguyen and D. Losic, Nitrogen-doped carbon-coated nanodiamonds for electrocatalytic applications, *Journal of Physics D: Applied Physics*, 54, (2020),
- [33] J. Koh, S. H. Park, M. W. Chung, S. Y. Lee and S. I. Woo, Diamond@carbon-onion hybrid nanostructure as a highly promising electrocatalyst for the oxygen reduction reaction, *RSC Advances*, 6, (2016), 27528-27534.
- [34] V. Celorrio, D. Plana, J. Flórez-Montaño, M. G. Montes de Oca, A. Moore, M. J. Lázaro, E. Pastor and D. J. Fermín, Methanol oxidation at diamond-supported Pt nanoparticles: effect of the diamond surface termination, *The Journal of Physical Chemistry C*, 117, (2013), 21735-21742.
- [35] Z. Jia, M. Peng, X. Cai, Y. Chen, X. Chen, F. Huang, L. Zhao, J. Diao, N. Wang, D. Xiao, X. Wen, Z. Jiang, H. Liu and D. Ma, Fully exposed platinum clusters on a nanodiamond/graphene hybrid for efficient low-temperature CO oxidation, *ACS Catalysis*, 12, (2022), 9602-9610.
- [36] R. Lu, J. B. Zang, Y. H. Wang and Y. L. Zhao, Microwave synthesis and properties of nanodiamond supported PtRu electrocatalyst for methanol oxidation, *Electrochimica Acta*, 60, (2012), 329-333.
- [37] Y. Wang, J. Zang, L. Dong, H. Pan, Y. Yuan and Y. Wang, Graphitized nanodiamond supporting PtNi alloy as stable anodic and cathodic electrocatalysts for direct methanol fuel cell, *Electrochimica Acta*, 113, (2013), 583-590.
- [38] F. Huang, Y. Deng, Y. Chen, X. Cai, M. Peng, Z. Jia, J. Xie, D. Xiao, X. Wen, N. Wang, Z. Jiang, H. Liu and D. Ma, Anchoring Cu(1) species over nanodiamond-graphene for semi-hydrogenation of acetylene, *Nature Communications*, 10, (2019), 4431.
- [39] K. T. Nicolae Spataru, Chiaki Terashima, Tata N. Rao and Akira Fujishima,



Electrochemical reduction of carbon dioxide at ruthenium dioxide deposited on boron-doped diamond, *Journal of Applied Electrochemistry*, 33, (2003), 1205-1210.

[40] T. I. a. X. E. Verykios, Charge transfer in metal catalysts supported on doped  $\text{TiO}_2$ : A theoretical approach based on metal-semiconductor contact theory, *Journal of Catalysis*, 161, (1996), 560-569.

[41] T. P. S. Rafik Addow, Nolan O'Connor, Michael J. Janik, Adri C.T. vanDuin, and Matthias Batzill, Influence of hydroxyls on Pd atom mobility and clustering on rutile  $\text{TiO}_2(011)\text{-}2 \times 1$ , *ACS Nano*, 8, (2014), 6321-6333.

[42] L. Wang, L. Wang, X. Meng and F. S. Xiao, New strategies for the preparation of sinter-resistant metal-nanoparticle-based catalysts, *Advanced Materials*, 31, (2019), e1901905.

[43] Y. Lou, J. Xu, Y. Zhang, C. Pan, Y. Dong and Y. Zhu, Metal-support interaction for heterogeneous catalysis: from nanoparticles to single atoms, *Materials Today Nano*, 12, (2020), 100093.

[44] H. Ooka, J. Huang and K. S. Exner, The sabatier principle in electrocatalysis: basics, limitations, and extensions, *Frontiers in Energy Research*, 9, (2021), 654460.

[45] Y. Tan, W. Zhu, Z. Zhang, W. Wu, R. Chen, S. Mu, H. Lv and N. Cheng, Electronic tuning of confined sub-nanometer cobalt oxide clusters boosting oxygen catalysis and rechargeable Zn–air batteries, *Nano Energy*, 83, (2021), 105813.

[46] J. R. J. K. Nørskov, A. Logadottir, L. Lindqvist, J. R. Kitchin, T. Bligaard, and H. Jónsson, Origin of the overpotential for oxygen reduction at a fuel-cell cathode, *J. Phys. Chem. B*, 108, (2004), 17886-17892.

[47] F. Abild-Pedersen, J. Greeley, F. Studt, J. Rossmeisl, T. R. Munter, P. G. Moses, E. Skúlason, T. Bligaard and J. K. Nørskov, Scaling properties of adsorption energies for hydrogen-containing molecules on transition-metal surfaces, *Phys Rev Lett*, 99, (2007), 016105.

[48] I. C. Man, H. Y. Su, F. Calle-Vallejo, H. A. Hansen, J. I. Martínez, N. G. Inoglu, J. Kitchin, T. F. Jaramillo, J. K. Nørskov and J. Rossmeisl, Universality in Oxygen Evolution Electrocatalysis on Oxide Surfaces, *ChemCatChem*, 3, (2011), 1159-1165.

[49] M. T. M. Koper, Thermodynamic theory of multi-electron transfer reactions: Implications for electrocatalysis, *Journal of Electroanalytical Chemistry*, 660, (2011), 254-260.

[50] J. Pérez-Ramírez and N. López, Strategies to break linear scaling relationships, *Nature Catalysis*, 2, (2019), 971-976.

[51] P. H. Jun Cheng, Peter Ellis, Sam French, Gordon Kelly and C. Martin Lok, Bronsted-Evans-Polanyi relation of multistep reactions and volcano curve in heterogeneous catalysis, *Journal of Physical Chemistry C*, 112, (2008), 1308-1311.

[52] T. Bligaard, J. K. Nørskov, S. Dahl, J. Matthiesen, C. H. Christensen and J. Sehested, The Brønsted–Evans–Polanyi relation and the volcano curve in heterogeneous catalysis, *Journal of Catalysis*, 224, (2004), 206-217.

- [53] P. H. Jun Cheng, Peter Ellis, Sam French, Gordon Kelly and C. Martin Lok, Brønsted-Evans-Polanyi relation of multistep reactions and volcano curve in heterogeneous catalysis, *J. Phys. Chem. C*, 112, (2008), 1308-1311.
- [54] J. K. N. B. Hammer, Why gold is the noblest of all the metals, *Nature*, 376, (1995), 238-240.
- [55] J. K. Nørskov, F. Abild-Pedersen, F. Studt and T. Bligaard, Density functional theory in surface chemistry and catalysis, *Proc Natl Acad Sci U S A*, 108, (2011), 937-943.
- [56] J. K. N. B. Hammer, Theoretical surface science and catalysis-calculations and concepts, *Advances in Catalysis*, 45, (2000), 71-129.
- [57] H. Xin, A. Vojvodic, J. Voss, J. K. Nørskov and F. Abild-Pedersen, Effects of d-band shape on the surface reactivity of transition-metal alloys, *Physical Review B*, 89, (2014), 115114.
- [58] I. Takigawa, K.-i. Shimizu, K. Tsuda and S. Takakusagi, Machine-learning prediction of the d-band center for metals and bimetals, *RSC Advances*, 6, (2016), 52587-52595.
- [59] S. K. Singh, K. Takeyasu and J. Nakamura, Active sites and mechanism of oxygen reduction reaction electrocatalysis on nitrogen-doped carbon materials, *Advanced Materials*, 31, (2019), e1804297.
- [60] L. P. Muhammad Tahir, Faryal Idrees, Xiangwen Zhang, Li Wang, Ji-Jun Zou, Zhong Lin Wang, Electrocatalytic oxygen evolution reaction for energy conversion and storage, *Nano Energy*, 37, (2017), 136-157.
- [61] H. N. N. Tobias Reier, Detre Teschner, Robert Schlogl and Peter Strasser, Electrocatalytic oxygen evolution reaction in acidic environments-reaction mechanisms and catalysts, *Advanced Energy Materials*, 7, (2017), 1601275.
- [62] L. Wei, E. H. Ang, Y. Yang, Y. Qin, Y. Zhang, M. Ye, Q. Liu and C. C. Li, Recent advances of transition metal based bifunctional electrocatalysts for rechargeable zinc-air batteries, *Journal of Power Sources*, 477, (2020), 228696.
- [63] S. Grimme, Semiempirical hybrid density functional with perturbative second-order correlation, *J Chem Phys*, 124, (2006), 034108.
- [64] S. Grimme, Accurate description of van der Waals complexes by density functional theory including empirical corrections, *J Comput Chem*, 25, (2004), 1463-1473.
- [65] P. Jurečka, J. Černý, P. Hobza and D. R. Salahub, Density functional theory augmented with an empirical dispersion term. Interaction energies and geometries of 80 noncovalent complexes compared with ab initio quantum mechanics calculations, *J Comput Chem*, 28, (2007), 555-569.
- [66] A. Tkatchenko and M. Scheffler, Accurate molecular van der waals interactions from ground-state electron density and free-atom reference data, *Physical Review Letters*, 102, (2009), 073005.
- [67] O. A. von Lilienfeld, I. Tavernelli, U. Rothlisberger and D. Sebastiani, Optimization of effective atom centered potentials for london dispersion forces in

density functional theory, *Phys Rev Lett*, 93, (2004), 153004.

[68] U. Zimmerli, M. Parrinello and P. Koumoutsakos, Dispersion corrections to density functionals for water aromatic interactions, *J Chem Phys*, 120, (2004), 2693-2699.

[69] H. S. Yu, S. L. Li and D. G. Truhlar, Perspective: Kohn-Sham density functional theory descending a staircase, *J Chem Phys*, 145, (2016), 130901.

[70] I. S. B. Michael G. Medvedev, Jianwei Sun, John P. Perdew, Konstantin A. Lyssenko, Density functional theory is straying from the path toward the exact functional, *Science*, 335, (2017), 49-52.

[71] D. R. Hartree, The wave mechanics of an atom with a non-coulomb central field. Part II. Some results and discussion, *Mathematical Proceedings of the Cambridge Philosophical Society*, 24, (2008), 111-132.

[72] V. Fock, "Selfconsistent field" mit Austausch für Natrium, *Zeitschrift für Physik*, 62, (1930), 795-805.

[73] F. R. S. D. R. Hartree, and W. Hartree, Self-consistent field, with exchange, for beryllium, *The royal society*, 150, (1935), 9-33.

[74] P. Hohenberg and W. Kohn, Inhomogeneous electron gas, *Physical Review*, 136, (1964), B864-B871.

[75] W. Kohn and L. J. Sham, Self-consistent equations including exchange and correlation effects, *Physical Review*, 140, (1965), A1133-A1138.

[76] Y. Park, V. Choong, Y. Gao, B. R. Hsieh and C. W. Tang, Work function of indium tin oxide transparent conductor measured by photoelectron spectroscopy, *Applied Physics Letters*, 68, (1996), 2699-2701.

[77] G. H. Kim, H. B. Kim, B. Walker, H. Choi, C. Yang, J. Park and J. Y. Kim, Effects of ionic liquid molecules in hybrid PbS quantum dot-organic solar cells, *ACS Appl Mater Interfaces*, 5, (2013), 1757-60.

[78] D. M. Fabian and S. Ardo, Hybrid organic–inorganic solar cells based on bismuth iodide and 1,6-hexanediammonium dication, *Journal of Materials Chemistry A*, 4, (2016), 6837-6841.

[79] J. Kowalska and S. DeBeer, The role of X-ray spectroscopy in understanding the geometric and electronic structure of nitrogenase, *Biochimica et Biophysica Acta (BBA) - Molecular Cell Research*, 1853, (2015), 1406-1415.

[80] C. Du, Q. Tan, G. Yin and J. Zhang, Rotating disk electrode method, *Journal*, (2014), 171-198.

[81] D. E. Beltrán and S. Litster, Half-wave potential or mass activity? Characterizing platinum group metal-free fuel cell catalysts by rotating disk electrodes, *ACS Energy Letters*, 4, (2019), 1158-1161.

[82] Z. F. Huang, J. Wang, Y. Peng, C. Y. Jung, A. Fisher and X. Wang, Design of efficient bifunctional oxygen reduction/evolution electrocatalyst: recent advances and perspectives, *Advanced Energy Materials*, 7, (2017), 1700544.

[83] L. Dai, Y. Xue, L. Qu, H. J. Choi and J. B. Baek, Metal-free catalysts for

oxygen reduction reaction, *Chemical Review*, 115, (2015), 4823-92.

[84] C. Tang and Q. Zhang, Nanocarbon for oxygen reduction electrocatalysis: Dopants, edges, and defects, *Advanced Materials*, 29, (2017), 1604103.

[85] F. D. Kuanping Gong, Zhenhai Xia, Michael Durstock, Liming Dai, Nitrogen doped carbon nanotube arrays with high electrocatalytic activity for oxygen reduction, *Science*, 323, (2009), 760-764.

[86] H. W. Liang, X. Zhuang, S. Bruller, X. Feng and K. Mullen, Hierarchically porous carbons with optimized nitrogen doping as highly active electrocatalysts for oxygen reduction, *Nature Communications*, 5, (2014), 4973.

[87] J. Zeng, Y. B. Mu, X. X. Ji, Z. J. Lin, Y. H. Lin, Y. H. Ma, Z. X. Zhang, S. G. Wang, Z. H. Ren and J. Yu, N,O-codoped 3D graphene fibers with densely arranged sharp edges as highly efficient electrocatalyst for oxygen reduction reaction, *Journal of Materials Science*, 54, (2019), 14495-14503.

[88] K. Gao, B. Wang, L. Tao, B. V. Cunnings, Z. Zhang, S. Wang, R. S. Ruoff and L. Qu, Efficient metal-free electrocatalysts from N-doped carbon nanomaterials: Mono-doping and co-doping, *Advanced Materials*, 31, (2019), e1805121.

[89] J. Zhu, W. Li, S. Li, J. Zhang, H. Zhou, C. Zhang, J. Zhang and S. Mu, Defective N/S-codoped 3D cheese-like porous carbon nanomaterial toward efficient oxygen reduction and Zn-air batteries, *Small*, 14, (2018), e1800563.

[90] R. Zhao, Q. Li, Z. Chen, V. Jose, X. Jiang, G. Fu, J.-M. Lee and S. Huang, B, N-doped ultrathin carbon nanosheet superstructure for high-performance oxygen reduction reaction in rechargeable zinc-air battery, *Carbon*, 164, (2020), 398-406.

[91] Z. Lu, G. Chen, S. Siahrostami, Z. Chen, K. Liu, J. Xie, L. Liao, T. Wu, D. Lin, Y. Liu, T. F. Jaramillo, J. K. Nørskov and Y. Cui, High-efficiency oxygen reduction to hydrogen peroxide catalysed by oxidized carbon materials, *Nature Catalysis*, 1, (2018), 156-162.

[92] L. Tao, Q. Wang, S. Dou, Z. Ma, J. Huo, S. Wang and L. Dai, Edge-rich and dopant-free graphene as a highly efficient metal-free electrocatalyst for the oxygen reduction reaction, *Chem Commun (Camb)*, 52, (2016), 2764-7.

[93] W. Takeuchi, Ura, Masato, Hiramatsu, Mineo, Tokuda, Yutaka, Kano, Hiroyuki, Hori, Masaru, Electrical conduction control of carbon nanowalls, *Applied Physics Letters*, 92, (2008), 213103.

[94] X. Xiao, X. Wang, X. Jiang, S. Song, D. Huang, L. Yu, Y. Zhang, S. Chen, M. Wang, Y. Shen and Z. Ren, In situ growth of Ru nanoparticles on (Fe,Ni)(OH)<sub>2</sub> to boost hydrogen evolution activity at high current density in alkaline media, *Small Methods*, 4, (2020), 1900796.

[95] A. Shen, Y. Zou, Q. Wang, R. A. Dryfe, X. Huang, S. Dou, L. Dai and S. Wang, Oxygen reduction reaction in a droplet on graphite: direct evidence that the edge is more active than the basal plane, *Angew Chem Int Ed Engl*, 53, (2014), 10804-10808.

[96] R. S. Donghui Guo, Chisato Akiba, Shunsuke Saji, Takahiro Kondo, Junji Nakamura, Active sites of nitrogen doped carbon materials for oxygen reduction reaction clarified using model catalysts, *Science*, 351, (2016), 361-365.

- [97] Z. Zhai, B. Leng, N. Yang, B. Yang, L. Liu, N. Huang and X. Jiang, Rational construction of 3D-networked carbon nanowalls/diamond supporting CuO architecture for high-performance electrochemical biosensors, *Small*, 15, (2019), e1901527.
- [98] A. M. Zaitsev, N. M. Kazuchits, V. N. Kazuchits, K. S. Moe, M. S. Rusetsky, O. V. Korolik, K. Kitajima, J. E. Butler and W. Wang, Nitrogen-doped CVD diamond: Nitrogen concentration, color and internal stress, *Diamond and Related Materials*, 105, (2020), 107794.
- [99] C. Y. Cheng and K. Teii, Control of the growth regimes of nanodiamond and nanographite in microwave plasmas, *IEEE Transactions on Plasma Science*, 40, (2012), 1783-1788.
- [100] A. C. Ferrari and D. M. Basko, Raman spectroscopy as a versatile tool for studying the properties of graphene, *Nat Nanotechnol*, 8, (2013), 235-46.
- [101] H. A. Casiraghi C., Qian H., Piscanec S., Georgi C., Fasoli A., Novoselov K. S., Basko D. M. and Ferrari A. C., Raman spectroscopy of graphene edges, *Nano letters*, 9, (2009), 1434-1440.
- [102] M. Taniguchi, R. Yoshie, K. Akikubo, A. Tateno, K. Hotozuka, N. Kawaguchi, T. Uchida, M. Tanimura and M. Tachibana, Effect of nitrogen and iron in carbon nanowalls on oxygen reduction reaction, *Electrochimica Acta*, 306, (2019), 132-142.
- [103] J. B. Wu, M. L. Lin, X. Cong, H. N. Liu and P. H. Tan, Raman spectroscopy of graphene-based materials and its applications in related devices, *Chem Soc Rev*, 47, (2018), 1822-1873.
- [104] K. Lehmann, O. Yurchenko, J. Melke, A. Fischer and G. Urban, High electrocatalytic activity of metal-free and non-doped hierarchical carbon nanowalls towards oxygen reduction reaction, *Electrochimica Acta*, 269, (2018), 657-667.
- [105] B. Yang, B. Yu, H. Li, N. Huang, L. Liu and X. Jiang, Enhanced and switchable silicon-vacancy photoluminescence in air-annealed nanocrystalline diamond films, *Carbon*, 156, (2020), 242-252.
- [106] Z. Q. Luo, S. H. Lim, Z. Q. Tian, J. Z. Shang, L. F. Lai, B. MacDonald, C. Fu, Z. X. Shen, T. Yu and J. Y. Lin, Pyridinic N doped graphene: synthesis, electronic structure, and electrocatalytic property, *Journal of Materials Chemistry*, 21, (2011), 8038-8044.
- [107] H. Miao, S. Li, Z. Wang, S. Sun, M. Kuang, Z. Liu and J. Yuan, Enhancing the pyridinic N content of Nitrogen-doped graphene and improving its catalytic activity for oxygen reduction reaction, *International Journal of Hydrogen Energy*, 42, (2017), 28298-28308.
- [108] C. Xiao, X. Chen, Z. Fan, J. Liang, B. Zhang and S. Ding, Surface-nitrogen-rich ordered mesoporous carbon as an efficient metal-free electrocatalyst for oxygen reduction reaction, *Nanotechnology*, 27, (2016), 445402.
- [109] Z. Liu, Z. Zhao, Y. Wang, S. Dou, D. Yan, D. Liu, Z. Xia and S. Wang, In Situ Exfoliated, Edge-Rich, Oxygen-Functionalized Graphene from Carbon Fibers for

Oxygen Electrocatalysis, *Advanced Materials*, 29, (2017),

[110] J. P. McClure, J. D. Thornton, R. Jiang, D. Chu, J. J. Cuomo and P. S. Fedkiw, Oxygen reduction on metal-free nitrogen-doped carbon nanowall electrodes, *Journal of The Electrochemical Society*, 159, (2012), F733-F742.

[111] Z. Zhai, B. Leng, N. Yang, B. Yang, L. Liu, N. Huang and X. Jiang, Rational construction of 3D-networked carbon nanowalls/diamond supporting CuO architecture for high-performance electrochemical biosensors, *Small*, 15, (2019), 1901527.

[112] R. S. Donghui Guo, Chisato Akiba, Shunsuke Saji, Takahiro Kondo, Junji Nakamura, Active sites of nitrogen-doped carbon materials for oxygen reduction reaction clarified using model catalysts, *Science*, 351, (2016), 361-365.

[113] H. Watanabe, H. Kondo, M. Hiramatsu, M. Sekine, S. Kumar, K. Ostrikov and M. Hori, Surface chemical modification of carbon nanowalls for wide-range control of surface wettability, *Plasma Processes and Polymers*, 10, (2013), 582-592.

[114] G. P. Keeley, N. McEvoy, H. Nolan, M. Holzinger, S. Cosnier and G. S. Duesberg, Electroanalytical sensing properties of pristine and functionalized multilayer graphene, *Chemistry of Materials*, 26, (2014), 1807-1812.

[115] R. J. R. a. R. L. McCreery, Quantitative relationship between electron transfer rate and surface microstructure of laser-modified graphite electrodes, *Analyse Chemistry*, 61, (1989), 1637-1641.

[116] M. Li, L. Zhang, Q. Xu, J. Niu and Z. Xia, N-doped graphene as catalysts for oxygen reduction and oxygen evolution reactions: Theoretical considerations, *Journal of Catalysis*, 314, (2014), 66-72.

[117] H. Kim, K. Lee, S. I. Woo and Y. Jung, On the mechanism of enhanced oxygen reduction reaction in nitrogen-doped graphene nanoribbons, *Phys Chem Chem Phys*, 13, (2011), 17505-10.

[118] K. H. Wu, D. W. Wang, X. Zong, B. S. Zhang, Y. F. Liu, I. R. Gentle and D. S. Su, Functions in cooperation for enhanced oxygen reduction reaction: the independent roles of oxygen and nitrogen sites in metal-free nanocarbon and their functional synergy, *Journal of Materials Chemistry A*, 5, (2017), 3239-3248.

[119] P. Yu, L. Wang, F. Sun, Y. Xie, X. Liu, J. Ma, X. Wang, C. Tian, J. Li and H. Fu, Co nanoislands rooted on Co-N-C nanosheets as efficient oxygen electrocatalyst for Zn-air batteries, *Advanced Materials*, 31, (2019), e1901666.

[120] X. Wan, X. Guo, M. Duan, J. Shi, S. Liu, J. Zhang, Y. Liu, X. Zheng and Q. Kong, Ultrafine CoO nanoparticles and Co-N-C lamellae supported on mesoporous carbon for efficient electrocatalysis of oxygen reduction in zinc-air batteries, *Electrochimica Acta*, 394, (2021), 139135.

[121] P. Chen, K. Xu, Y. Tong, X. Li, S. Tao, Z. Fang, W. Chu, X. Wu and C. Wu, Cobalt nitrides as a class of metallic electrocatalysts for the oxygen evolution reaction, *Inorganic Chemistry Frontiers*, 3, (2016), 236-242.

[122] P. Chen, K. Xu, Z. Fang, Y. Tong, J. Wu, X. Lu, X. Peng, H. Ding, C. Wu and Y. Xie, Metallic Co<sub>4</sub>N porous nanowire arrays activated by surface oxidation as electrocatalysts for the oxygen evolution reaction, *Angew Chem Int Ed Engl*, 54, (2015),

14710-14714.

[123] P. Yin, T. Yao, Y. Wu, L. Zheng, Y. Lin, W. Liu, H. Ju, J. Zhu, X. Hong, Z. Deng, G. Zhou, S. Wei and Y. Li, Single cobalt atoms with precise N-coordination as superior oxygen reduction reaction catalysts, *Angew Chem Int Ed Engl*, 55, (2016), 10800-10805.

[124] Z. Zhang, C. S. Lee and W. Zhang, Vertically aligned graphene nanosheet arrays: Synthesis, properties and applications in electrochemical energy conversion and storage, *Advanced Energy Materials*, 7, (2017), 1700678.

[125] T. P. S. Rafik Addow, Nolan O'Connor, Michael J. Janik, AdriC.T. vanDuin, and Matthias Batzill, Influence of hydroxyls on Pd atom mobility and clustering on rutile TiO<sub>2</sub>(011)-2X1, *ACS Nano*, 8, (2014), 6321-6333.

[126] Q. Q. Yan, D. X. Wu, S. Q. Chu, Z. Q. Chen, Y. Lin, M. X. Chen, J. Zhang, X. J. Wu and H. W. Liang, Reversing the charge transfer between platinum and sulfur-doped carbon support for electrocatalytic hydrogen evolution, *Nature Communications*, 10, (2019), 4977.

[127] G. Vilé, D. Albani, M. Nachtegaal, Z. Chen, D. Dontsova, M. Antonietti, N. López and J. Pérez-Ramírez, A stable single-site palladium catalyst for hydrogenations, *Angew Chem Int Ed Engl*, 54, (2015), 11265-11269.

[128] T. I. a. X. E. Verykios, Charge Transfer in Metal Catalysts Supported on Doped TiO<sub>2</sub>: A Theoretical Approach Based on Metal-Semiconductor Contact Theory, 161, (1996), 560-569.

[129] T. Schiros, D. Nordlund, L. Pálová, D. Prezzi, L. Zhao, K. S. Kim, U. Wurstbauer, C. Gutiérrez, D. Delongchamp, C. Jaye, D. Fischer, H. Ogasawara, L. G. Pettersson, D. R. Reichman, P. Kim, M. S. Hybertsen and A. N. Pasupathy, Connecting dopant bond type with electronic structure in N-doped graphene, *Nano Lett*, 12, (2012), 4025-4031.

[130] Z. Chen, Y. Song, J. Cai, X. Zheng, D. Han, Y. Wu, Y. Zang, S. Niu, Y. Liu, J. Zhu, X. Liu and G. Wang, Tailoring the d-Band Centers Enables Co<sub>4</sub>N Nanosheets To Be Highly Active for Hydrogen Evolution Catalysis, *Angew Chem Int Ed Engl*, 57, (2018), 5076-5080.

[131] B. H. a. J. K. Nørskov, Why gold is the noblest of all the metals, *Nature*, 376, (1995), 238-239.

[132] B. Cao, M. Hu, Y. Cheng, P. Jing, B. Liu, B. Zhou, X. Wang, R. Gao, X. Sun, Y. Du and J. Zhang, Tailoring the d-band center of N-doped carbon nanotube arrays with Co<sub>4</sub>N nanoparticles and single-atom Co for a superior hydrogen evolution reaction, *NPG Asia Materials*, 13, (2021), 1-14.

[133] L. Dai, Y. Xue, L. Qu, H. J. Choi and J. B. Baek, Metal-free catalysts for oxygen reduction reaction, *Chemical Review*, 115, (2015), 4823-4892.

[134] W. Yuan, S. Wang, Y. Ma, Y. Qiu, Y. An and L. Cheng, Interfacial Engineering of Cobalt Nitrides and Mesoporous Nitrogen-Doped Carbon: Toward Efficient Overall Water-Splitting Activity with Enhanced Charge-Transfer Efficiency,

ACS Energy Letters, 5, (2020), 692-700.

[135] L. Chen, Y. Zhang, X. Liu, L. Long, S. Wang, X. Xu, M. Liu, W. Yang and J. Jia, Bifunctional oxygen electrodes of homogeneous Co<sub>4</sub>N nanocrystals@N-doped carbon hybrids for rechargeable Zn-air batteries, Carbon, 151, (2019), 10-17.

[136] H. Zhang, D. Tian, Z. Zhao, X. Liu, Y.-N. Hou, Y. Tang, J. Liang, Z. Zhang, X. Wang and J. Qiu, Cobalt nitride nanoparticles embedded in porous carbon nanosheet arrays propelling polysulfides conversion for highly stable lithium–sulfur batteries, Energy Storage Materials, 21, (2019), 210-218.

[137] Y. Yang, R. Zeng, Y. Xiong, F. J. DiSalvo and H. D. Abruna, Cobalt-Based Nitride-Core Oxide-Shell Oxygen Reduction Electrocatalysts, J Am Chem Soc, 141, (2019), 19241-19245.

[138] X. Yu, T. Zhou, J. Ge and C. Wu, Recent Advances on the Modulation of Electrocatalysts Based on Transition Metal Nitrides for the Rechargeable Zn-Air Battery, ACS Materials Letters, 2, (2020), 1423-1434.

[139] Q. Xu, H. Jiang, Y. Li, D. Liang, Y. Hu and C. Li, In-situ enriching active sites on co-doped Fe-Co<sub>4</sub>N@N-C nanosheet array as air cathode for flexible rechargeable Zn-air batteries, Applied Catalysis B: Environmental, 256, (2019), 117893.

[140] Z. Zhang, W. Li, M. F. Yuen, T. W. Ng, Y. Tang, C. S. Lee, X. Chen and W. Zhang, Hierarchical composite structure of few-layers MoS<sub>2</sub> nanosheets supported by vertical graphene on carbon cloth for high-performance hydrogen evolution reaction, Nano Energy, 18, (2015), 196-204.

[141] W. Zhang, C. H. Xu, H. Zheng, R. Li and K. Zhou, Oxygen-rich cobalt–nitrogen–carbon porous nanosheets for bifunctional oxygen electrocatalysis, Advanced Functional Materials, (2022), 2200763.

[142] T. Y. Ma, S. Dai, M. Jaroniec and S. Z. Qiao, Metal-organic framework derived hybrid Co<sub>3</sub>O<sub>4</sub>-carbon porous nanowire arrays as reversible oxygen evolution electrodes, JAm Chem Soc, 136, (2014), 13925-13931.

[143] K. Kordek, L. Jiang, K. Fan, Z. Zhu, L. Xu, M. Al-Mamun, Y. Dou, S. Chen, P. Liu, H. Yin, P. Rutkowski and H. Zhao, Two-step activated carbon cloth with oxygen-rich functional groups as a high-performance additive-free air electrode for flexible Zinc–air batteries, Advanced Energy Materials, 9, (2018), 1802936.

[144] W. Zang, A. Sumboja, Y. Ma, H. Zhang, Y. Wu, S. Wu, H. Wu, Z. Liu, C. Guan, J. Wang and S. J. Pennycook, Single Co Atoms Anchored in Porous N-Doped Carbon for Efficient Zinc–Air Battery Cathodes, ACS Catalysis, 8, (2018), 8961-8969.

[145] F. Meng, H. Zhong, D. Bao, J. Yan and X. Zhang, In situ coupling of strung Co<sub>4</sub>N and intertwined N-C fibers toward free-standing bifunctional cathode for robust, efficient, and flexible Zn-air batteries, JAm Chem Soc, 138, (2016), 10226-10231.

[146] H. Qi, Y. Feng, Z. Chi, Y. Cui, M. Wang, J. Liu, Z. Guo, L. Wang and S. Feng, In situ encapsulation of Co-based nanoparticles into nitrogen-doped carbon nanotubes-modified reduced graphene oxide as an air cathode for high-performance Zn-air batteries, Nanoscale, 11, (2019), 21943-21952.

[147] H. Guo, Q. Feng, J. Zhu, J. Xu, Q. Li, S. Liu, K. Xu, C. Zhang and T. Liu,



Cobalt nanoparticle-embedded nitrogen-doped carbon/carbon nanotube frameworks derived from a metal–organic framework for tri-functional ORR, OER and HER electrocatalysis, *Journal of Materials Chemistry A*, 7, (2019), 3664-3672.

[148] M. N. Han, M. J. Shi, J. Wang, M. L. Zhang, C. Yan, J. T. Jiang, S. H. Guo, Z. Y. Sun and Z. H. Guo, Efficient bifunctional Co/N dual-doped carbon electrocatalysts for oxygen reduction and evolution reaction, *Carbon*, 153, (2019), 575-584.

[149] T. Ø. Oluf Bøckman, George A. Voyiatzis, George N. Papatheodorou, Raman spectroscopy of cemented cobalt on zinc substrates, *Hydrometallurgy*, 55, (2000), 93-105.

[150] M. S. Vidhya, G. Ravi, R. Yuvakkumar, D. Velauthapillai, M. Thambidurai, C. Dang, B. Saravanakumar, A. Syed and T. M.S. Dawoud, Functional reduced graphene oxide/cobalt hydroxide composite for energy storage applications, *Materials Letters*, 276, (2020),

[151] Y. Wang, A. Xu, Z. Wang, L. Huang, J. Li, F. Li, J. Wicks, M. Luo, D. H. Nam, C. S. Tan, Y. Ding, J. Wu, Y. Lum, C. T. Dinh, D. Sinton, G. Zheng and E. H. Sargent, Enhanced nitrate-to-ammonia activity on copper-nickel alloys via tuning of intermediate adsorption, *J Am Chem Soc*, 142, (2020), 5702-5708.

[152] Y. Wang, W. Zhou, R. Jia, Y. Yu and B. Zhang, Unveiling the activity origin of a copper-based electrocatalyst for selective nitrate reduction to ammonia, *Angew Chem Int Ed Engl*, 59, (2020), 5350-5354.

[153] G. F. Chen, Y. Yuan, H. Jiang, S. Y. Ren, L. X. Ding, L. Ma, T. Wu, J. Lu and H. Wang, Electrochemical reduction of nitrate to ammonia via direct eight-electron transfer using a copper–molecular solid catalyst, *Nature Energy*, 5, (2020), 605-613.

[154] Q. Wang, H. Huang, L. Wang and Y. Chen, Electrochemical removal of nitrate by Cu/Ti electrode coupled with copper-modified activated carbon particles at a low current density, *Environ Sci Pollut Res Int*, 26, (2019), 17567-17576.

[155] Z. Zhang, Y. Xu, W. Shi, W. Wang, R. Zhang, X. Bao, B. Zhang, L. Li and F. Cui, Electrochemical-catalytic reduction of nitrate over Pd–Cu/ $\gamma$ -Al<sub>2</sub>O<sub>3</sub> catalyst in cathode chamber: Enhanced removal efficiency and N<sub>2</sub> selectivity, *Chemical Engineering Journal*, 290, (2016), 201-208.

[156] X. Zhang, Y. Wang, C. Liu, Y. Yu, S. Lu and B. Zhang, Recent advances in non-noble metal electrocatalysts for nitrate reduction, *Chemical Engineering Journal*, 403, (2021), 126269.

[157] E. G. C. Reuben, H. Cohen, R. Tenne, R. Kalish, Y. Muraki, K. Hashimoto, A. Fujishima, J.M. Butler, C. Lévy-Clément, Efficient reduction of nitrite and nitrate to ammonia using thin-film B-doped diamond electrodes, *Journal of Electroanalytical Chemistry*, 396, (1995), 233-239.

[158] C. Lévy-Clément, N. A. Ndao, A. Katty, M. Bernard, A. Deneuville, C. Comninellis and A. Fujishima, Boron doped diamond electrodes for nitrate elimination in concentrated wastewater, *Diamond and Related Materials*, 12, (2003), 606-612.

[159] J. T. Matsushima, W. M. Silva, A. F. Azevedo, M. R. Baldan and N. G.

Ferreira, The influence of boron content on electroanalytical detection of nitrate using BDD electrodes, *Applied Surface Science*, 256, (2009), 757-762.

[160] J. Sotelo-Gil, E. Cuevas-Yañez and B. A. Frontana-Uribe, Recent advances on boron doped diamond (BDD) electrode as cathode in organic and inorganic preparative electrotransformations, *Current Opinion in Electrochemistry*, 34, (2022), 101004.

[161] P. Kuang, K. Natsui, Y. Einaga, C. Feng, Y. Cui, W. Zhang and Y. Deng, Annealing enhancement in stability and performance of copper modified boron-doped diamond (Cu-BDD) electrode for electrochemical nitrate reduction, *Diamond and Related Materials*, 114, (2021), 108310.

[162] J. Xu, N. Yang, S. Heuser, S. Yu, A. Schulte, H. Schönherr and X. Jiang, Achieving ultrahigh energy densities of supercapacitors with porous titanium carbide/boron-doped diamond composite electrodes, *Advanced Energy Materials*, 9, (2019), 1803623.

[163] V. S. Aleksei Chepurov, Dmitry Shcheglov, Alexander Latyshev, Evgeny Filatov, Alexander Yelisseyev, A highly porous surface of synthetic monocrystalline diamond effect of etching by Fe nanoparticles in hydrogen atmosphere, *International Journal of Refractory Metal & Hard Materials*, 76, (2018), 12-15.

[164] E. Bustarret, E. Gheeraert and K. Watanabe, Optical and electronic properties of heavily boron-doped homo-epitaxial diamond, *physica status solidi (a)*, 199, (2003), 9-18.

[165] V. Mortet, A. Taylor, Z. Vlčková Živcová, D. Machon, O. Frank, P. Hubík, D. Tremouilles and L. Kavan, Analysis of heavily boron-doped diamond raman spectrum, *Diamond and Related Materials*, 88, (2018), 163-166.

[166] G. Vile, D. Albani, M. Nachtegaal, Z. Chen, D. Dontsova, M. Antonietti, N. Lopez and J. Perez-Ramirez, A stable single-site palladium catalyst for hydrogenations, *Angew Chem Int Ed Engl*, 54, (2015), 11265-11269.

[167] P. K. a. J. A. M. Fedurco, Effect of multivalent cations upon reduction of nitrate ions at the Ag electrode, *Journal of The Electrochemical Society*, 146, (1999), 2569.

[168] T. Hu, C. Wang, M. Wang, C. M. Li and C. Guo, Theoretical insights into superior nitrate reduction to ammonia performance of copper catalysts, *ACS Catalysis*, 11, (2021), 14417-14427.

[169] Y. Guo, R. Zhang, S. Zhang, Y. Zhao, Q. Yang, Z. Huang, B. Dong and C. Zhi, Pd doping-weakened intermediate adsorption to promote electrocatalytic nitrate reduction on TiO<sub>2</sub> nanoarrays for ammonia production and energy supply with zinc-nitrate batteries, *Energy & Environmental Science*, 14, (2021), 3938-3944.

[170] J. Wordsworth, T. M. Benedetti, S. V. Somerville, W. Schuhmann, R. D. Tilley and J. J. Gooding, The influence of nanoconfinement on electrocatalysis, *Angew Chem Int Ed Engl*, 61, (2022), e202200755.

**Lebenslauf**

Name:	Chuyan Zhang
Geburtsdatum:	06.05.1991
Geburtsort:	Liaoning, China
Staatsangehörigkeit:	Chinesische
03/2019-06/2023	Wissenschaftlicher Mitarbeiter und Doktorandin am Lehrstuhl für Oberflächen- und Werkstofftechnologie (LOT) des Instituts für Werkstofftechnik der Universität Siegen, unter der Leitung von Prof. Xin Jiang Gastwissenschaftler in der Gruppe von Dünnschichtmaterialien und Grenzflächen am Institute für Metallforschung (IMR) der Chinesischen Akademie in Shenyang, China
03/2014-06/2018	Materialwissenschaft Studium ( <i>Master of Science</i> ), an der TU-Clausthal
09/2008-06/2013	Materialwissenschaft und Werkstofftechnik Studium ( <i>Bachelor of Science</i> ), an der Tongji Universität Shanghai
09/2002-06/2008	Mittel- und Oberschule an der 20. Oberschule in Shenyang

## Publikationen

1. **Chuyan Zhang**, Nan Huang, Zhaofeng Zhai, BinChen, Lusheng Liu, Bing Yang, Xin Jiang, Nianjun Yang, Bifunctional oxygen electrocatalyst of Co<sub>4</sub>N and nitrogen-doped carbon nanowalls/diamond for high-performance flexible zinc-air batteries, *Advanced Energy Materials*, accepted, 2023.
2. Zhaofeng Zhai, **Chuyan Zhang**, Ruiwen Xie, Bin Chen, Ziwen Zheng, Lusheng Liu, Bing Yang, Dan Shi, Xin Jiang, Nan Huang, Two-dimensional diamond formation drivers in chemical vapor deposition: planar defects and graphite, *Crystal Growth and Design*, 2023, 23, 2321-2330.
3. **Chuyan Zhang**, Nan Huang, Zhaofeng Zhai, Lusheng Liu, Bin Chen, Zhigang Lu, Meiqi Zhou, Haozhe Song, Dan Shi, Bing Yang, Nianjun Yang, Xin Jiang, Nitrogen-doped carbon nanowalls/diamond films as efficient electrocatalysts toward oxygen reduction reaction, *Nanotechnology*, 2022, 33, 015401.
4. Meiqi Zhou, Zhaofeng Zhai, Lusheng Liu, **Chuyan Zhang**, Ziyao Yuan, Zhigang Lu, Bin Chen, Dan Shi, Bing Yang, Qiuping Wei, Nan Huang, XinJiang, Controllable synthesized diamond/CNWs film as a novel nanocarbon electrode with wide potential window and enhanced S/B ratio for electrochemical sensing, *Applied Surface Science*, 2021, 551, 149418.
5. Dan Shi, Lusheng Liu, Zhaofeng Zhai, Bin Chen, Zhigang Lu, **Chuyan Zhang**, Ziyao Yuan, Meiqi Zhou, Bing Yang, Nan Huang, Xin Jiang, Effect of oxygen terminated surface of boron-doped diamond thin-film electrode on seawater salinity sensing, *Journal of Materials Science & Technology*, 2021, 86, 1-10.
6. Zhigang Lu, Nan Huang, Zhaofeng Zhai, Bin Chen, Lusheng Liu, Haozhe Song, Ziyao Yuan, **Chuyan Zhang**, Bing Yang, Xin Jiang, Intergration of 3D interconnected porous microstructure and high electrochemical property for boron-doped diamond by facile strategy, *Journal of Materials Science & Technology*, 2022, 105, 26-35.